# Master thesis and internship[BR]- Master's thesis : Aeroelastic analysis of a slender wing : wind tunnel tests and modelling[BR]- Integration internship

**Auteur :** Pirnay, Maxime
**Promoteur(s) :** Andrianne, Thomas
**Faculté :** Faculté des Sciences appliquées
**Diplôme :** Master en ingénieur civil en aérospatiale, à finalité spécialisée en "aerospace engineering"
**Année académique :** 2024-2025
**URI/URL :** http://hdl.handle.net/2268.2/23386

UNIVERSITY OF LIÈGE - SCHOOL OF ENGINEERING

# Aeroelastic analysis of a slender wing : wind tunnel tests and modelling

---

MASTER THESIS PRESENTED BY
**P**IRNAY **M**AXIME
IN PARTIAL FULFILMENT OF THE REQUIREMENTS FOR THE DEGREE OF MASTER OF SCIENCE IN AEROSPACE ENGINEERING

---

**THESIS SUPERVISORS**

Professor Thomas Andrianne
*University of Liège*

Professor Xavier Amandolèse
*Conservatoire national des arts et métiers*

**JURY MEMBERS**

Prof. Thomas Andrianne, Prof. Xavier Amandolèse, Prof. Loïc Salles

Liège, Academic year 2024-2025

# Abstract

The development of lightweight and flexible wing structures in modern aerospace applications raises critical challenges in the prediction and control of aeroelastic instabilities, particularly flutter. In this context, this thesis addresses the modelling and experimental validation of flutter phenomena in slender, flexible wing structures. The study combines the development of a reduced-order aeroelastic model with wind tunnel testing to investigate the stability of high aspect-ratio configurations.

The numerical model is constructed using a Rayleigh–Ritz decomposition of the structural dynamics, coupled with two aerodynamic representations: a quasi-steady approximation and an unsteady formulation based on Theodorsen's theory. The approach allows for capturing bending–torsion coupling and tip-mass effects using a low-order formulation. A parametric study is conducted to investigate the influence of design variables, including tip mass, tip torsional inertia, chordwise location of the mass and other design choices, on the minimum flutter speed.

Two experimental campaigns were carried out to support and validate the numerical model. A first wing configuration, developed at the Institut Aérotechnique (IAT), was tested to identify modal characteristics and assess aerodynamic coefficients through incidence measurements. These measurements revealed a significant influence of inter-section gaps and three-dimensional effects on the aerodynamic slopes. The second wing, designed at the University of Liège, was tested under increasing flow speeds to observe flutter onset. In both cases, dynamic responses were recorded using accelerometers and/or laser sensor. Modal parameters were extracted using identification techniques including Stochastic Subspace Identification (SSI) and PolyMAX.

The comparison between experimental and numerical results confirms the model's ability to predict frequency evolution, damping trends, and aeroelastic instabilities. In particular, the observed flutter regime for the Liège wing is qualitatively well captured by the unsteady aerodynamic formulation. Furthermore, the influence of parameter uncertainties was investigated through sensitivity analyses.

***Keywords*** : flutter, modal analysis, PolyMAX, Stochastic subspace identification, wind tunnel, slender wing.

# Acknowledgement

This thesis represents the culmination of my academic journey, and it would not have been possible without the support, guidance, and encouragement of many individuals.

First and foremost, I would like to express my deepest gratitude to my supervisor, Thomas Andrianne from the University of Liège, for his constant guidance and insightful advice throughout this project. His expertise and encouragement were instrumental to the successful completion of this work.

I am also sincerely thankful to my co-supervisor, Xavier Amandolèse from the Conservatoire national des arts et métiers, for welcoming me to Paris and providing all the necessary resources to carry out this research. His availability, thoughtful feedback, and the time he devoted to analysing results and debugging code with me were truly invaluable.

My thanks also go to Olivier Vallon and Alexandre Debisschop from the Institut Aérotechnique, whose support during the setup and calibration of the measurement equipment was essential. I would further like to acknowledge Boris Lossouarn, who, although less directly involved, generously provided key equipment and shared his expertise during our interactions. The enriching experience I had in Paris was largely due to their support and kindness.

At the University of Liège, I am grateful to Edouard Verstraelen for his guidance during the wind tunnel tests. His availability and assistance in analysing the results were of great value. I also thank Antoine and Mathieu from the Fablab for their help during the design and manufacturing phases of the wing.

A special thanks to Andrea, Antoine, and Jérôme, with whom I shared an office (and many coffee breaks) throughout the semester. Their company made the experience all the more enjoyable.

Finally, I am deeply grateful to my girlfriend for her unwavering support and encouragement during these years of study.

To all those who have contributed to this journey, directly or indirectly, thank you. Your support has made this achievement possible, and I am sincerely appreciative.

# Contents

# List of Figures

# Chapter 1

# Introduction

## 1.1 Context and motivation

Aeroelasticity is the branch of physics and engineering that studies the mutual interactions between inertial, elastic, and aerodynamic forces acting on a deformable body exposed to a fluid flow. A widely used representation to illustrate the fundamental couplings in aeroelastic phenomena is Collar's triangle, introduced by Collar (1946), and shown in Figure 1.1.

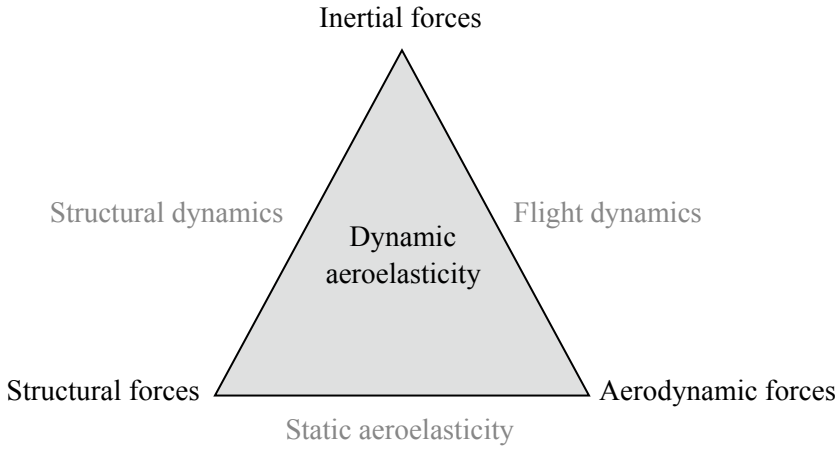


**Figure 1.1:** Collar's triangle.

Throughout the history of aeronautics, aeroelasticity has played a crucial role in aircraft design. Aeroelastic phenomena can induce unwanted structural behaviour, potentially leading to catastrophic failures, and thus constitute one of the main factors limiting the operational flight envelope. In the context of the present work, the focus is placed specifically on flutter-type instabilities.

One of the earliest documented cases of flutter occurred in 1916 with the Handley Page O/400 bomber, which was destroyed in flight due to a coupling of vibrational modes. The case was studied and reported by Lanchester (1916), together with Bairstow & Fage (1916) in the same year. They discovered that the fuselage and horizontal tail had two principal low-frequency modes of vibrations. This incident illustrated how interactions between multiple structural modes could trigger dynamic instabilities well before the mechanisms were fully understood. Despite progress over the decades, modern aircraft still require extensive efforts to prevent aeroelastic effects. These include ground vibration tests (GVTs), flight vibration tests (FVTs), and extensive theoretical and computational analyses during the design and certification phases.

In recent years, advances in aerospace engineering have further intensified research into aeroelasticity. The drive for more efficient aircraft, achieving lower fuel consumption and improved aerodynamic performance, has led to the development of wings with higher aspect ratios and the increased use of lighter

materials. While these trends offer significant benefits in terms of aerodynamic efficiency and structural weight reduction, they also enhance fluid-structure interactions by making wings more flexible (Raghavan & Patil 2006).

This increased flexibility, combined with the growing trend toward slender, high aspect-ratio wings, makes modern structures more susceptible to significant static and dynamic deformations under aerodynamic loading. In particular, slender wings, characterized by their long span and reduced chord, are highly sensitive to fluid–structure interactions. Under certain conditions, these interactions can trigger dynamic instabilities such as flutter, where motion-induced aerodynamic forces transfer energy into the structure's natural modes of vibration. Accurately understanding and predicting this behaviour is essential to ensure the stability and performance of flexible systems across various engineering applications.

In this context, this work focuses on high aspect-ratio lifting surfaces operating in subsonic regimes, which are commonly encountered in applications such as solar-powered UAV wings, High Altitude Long Endurance (HALE) drones, and large wind turbine blades. These structures often undergo static and dynamic deformations, raising concerns about whether traditional aeroelastic models can accurately predict flutter onset and post-critical behaviour.

One illustrative case that highlights the importance of accurate aeroelastic modelling is the Helios Prototype, a solar-powered HALE aircraft developed by NASA. As shown in Figure 1.2, the aircraft experienced a structural failure during a flight test in 2003. The failure was initiated by an unanticipated aeroelastic response when the aircraft encountered atmospheric disturbances. These conditions led to excessive wing deformation, resulting in an unstable coupling between aerodynamic loads and structural flexibility. This dynamic interaction caused growing oscillations, increased loading on the wing structure, and ultimately exceeded the design's elastic limits, leading to the aircraft's failure over the Pacific ocean. This incident underscored the potentially catastrophic consequences of underestimating aeroelastic phenomena in lightweight, high-span configurations. It also marked a turning point in how aeroelastic safety margins are considered in the design of slender structures.

**(a)** Helios prototype just before breaking up.

**(b)** Wreckage of Helios in the Pacific.

**Figure 1.2:** The *AeroVironment Helios Prototype* shortly before and after experiencing aeroelastic failure.

Beyond the scientific challenges, this research is also driven by strategic considerations. HALE drones offer significant advantages for surveillance, reconnaissance, and communication missions. However, Europe does not currently operate its own HALE-class drone and remains dependent on non-European systems for these capabilities. This situation reflects a broader dependence on manufacturers such as the United States and Israel, whose HALE drones, including the RQ-4 Global Hawk and the IAI Heron, are already widely deployed (Figure 1.3). While these systems are technically advanced, relying on suppliers embedded in complex geopolitical dynamics raises concerns about autonomy, access, and long-term strategic flexibility for European states (Colaone 2010).

The ambition to address this gap is not new. Projects such as the Eurodrone were initiated over a decade ago to strengthen Europe's industrial base and reduce reliance on foreign platforms. However, technical,

political, and industrial challenges have slowed progress. Among these, understanding and controlling aeroelastic effects in large flexible structures remains a major technical challenge. As shown in Figure 1.3, current HALE systems like the Global Hawk and the IAI Heron illustrate the structural and aerodynamic complexity that future European models be required to meet.

More recently, defence has become a central element of European industrial policy. The European Defence Fund (EDF) was created to finance collaborative R&D efforts between member states, reflecting a move towards more integrated and strategic defence efforts (Kunertova 2019). By supporting cross-border cooperation, reducing market fragmentation and strengthening the European defence industrial and technological base, the EDF aims to improve the competitiveness and autonomy of the EU defence sector.


**(a)** *Northrop Grumman RQ-4 Global Hawk*.

**(b)** *IAI Heron*.

**Figure 1.3:** HALE-class drones.

While the strategic dimension of aeroelastic design is particularly evident in the aerospace sector, similar concerns are also gaining ground in the field of renewable energies, especially in the area of offshore wind power. Coastal regions benefit from large and consistent wind resources, often located close to major population centers, making offshore wind an attractive option for clean power generation. However, the high costs associated with offshore infrastructure, support structures and maintenance continue to limit the economic viability of these systems.

In this context, vertical axis wind turbines (VAWTs) are gaining increasing attention as a promising alternative to traditional horizontal axis designs. Their structural simplicity, reduced tower height, and ability to capture wind from all directions without active yaw mechanisms make them particularly suited to offshore environments. However, with these advantages come new technical challenges, particularly in terms of aeroelastic stability. On a large scale, the flexibility of VAWT blades and their particular motion in the wind field give rise to complex and potentially unstable fluid-structure interactions.

## 1.2 Objectives of the work

This thesis focuses on the investigation of flutter phenomena in slender, flexible structures, with particular attention to configurations relevant to modern aerospace applications. The objective is to gain a better understanding of the mechanisms leading to flutter onset in systems with high aspect-ratio lifting surfaces, and to assess how simplified modelling tools can be used effectively in that context.

A mathematical model for aeroelastic analysis has been developed to predict flutter onset based on classical linear theory. This model serves as a reference for interpreting the dynamic behaviour of flexible structures subjected to aerodynamic loading. To support and validate the theoretical predictions, two experimental campaigns were conducted using wings with similar geometry and aerodynamic characteristics. These tests were carried out at the Institut Aérotechnique (IAT) in Saint-Cyr-l'École and in the subsonic wind tunnel at the University of Liège. The primary aim of these campaigns is to assess the

accuracy of the model and to observe the onset of aeroelastic instabilities under controlled conditions.

## 1.3 Thesis outline

The thesis is divided into three main chapters. chapter 2 introduces the theoretical foundations of the study, covering essential aerodynamic and aeroelastic concepts. It then details the development of the mathematical model used for flutter prediction. The structure is modelled using the Rayleigh–Ritz method, which leads to the formulation of the structural matrices. Aerodynamic forces are incorporated through both quasi-steady and unsteady formulations, including Theodorsen's theory. A parametric study is then carried out to investigate the influence of wingtip configuration and design choices on the flutter speed.

chapter 3 presents the experimental investigations conducted during two wind tunnel test campaigns. The wing design is first described, followed by the setups used in both campaigns, with particular attention given to excitation methods and measurement techniques. Two identification procedures are then outlined, as they are employed for both wind-off and wind-on modal analyses. Finally, the results of both campaigns are reported.

Finally, chapter 4 provides a comparison between model predictions and experimental observations, allowing for an assessment of the model's validity. Moreover, the effect of parameter uncertainties are discussed.

# Chapter 2

# Aeroelastic modelling

This chapter is dedicated to the development of a mathematical model for predicting the aeroelastic behaviour of the system. It begins with a section outlining the theoretical foundations upon which the analysis is based. The modelling approach and underlying assumptions are then presented, with detailed descriptions of both the structural and aerodynamic formulations. Finally, a parametric study is conducted to gain deeper insight into the flutter mechanism and to evaluate how it can be influenced through key design parameters.

## 2.1 Theoretical background

This section presents the theoretical foundations necessary to support the developments and analyses conducted in this work. In this context, aerodynamic principles and aeroelastic concepts are introduced to provide a clearer understanding of the physical mechanisms involved.

### 2.1.1 Aerodynamic principles

A wing exposed to a fluid flow experiences pressure differentials along its surface, which give rise to distributed aerodynamic forces and moments. These aerodynamic loads can be decomposed into three force components,*i.e.* lift, drag, and side force, and three moment components,*i.e.* pitching, rolling, and yawing moments. In the present work, a simplified two-dimensional representation is used to analyse the forces acting on a wing section per unit span. Assuming negligible three-dimensional effects, the normal force $F_N$ and the chordwise force $F_C$ can be related to the lift $L$ and drag $D$ components in the flow-aligned frame through the angle of attack $\alpha_r$. It writes

$$\begin{aligned} L &= F_N \cos\alpha_r - F_C \sin\alpha_r, \\ D &= F_N \sin\alpha_r + F_C \cos\alpha_r. \end{aligned} \tag{2.1}$$

A representation of the forces acting on the wing section is provided in Figure 2.1. To generalize aerodynamic analysis and allow comparison across different geometries and flow conditions, the forces and moments are typically expressed in terms of non-dimensional aerodynamic coefficients

$$C_L = \frac{L}{p_{\text{dyn}}\, S} \quad , \quad C_D = \frac{D}{p_{\text{dyn}}\, S} \quad , \quad C_{M_{ea}} = \frac{M_{ea}}{p_{\text{dyn}}\, S\, c}, \tag{2.2}$$

where $p_{\text{dyn}} = \rho U^2/2$ is the dynamic pressure, $S$ is the wing reference area, and $c$ is the chord length. Aerodynamic forces are assumed to act at the aerodynamic centre, typically located at the quarter-chord position. The aerodynamic moment, on the other hand, is evaluated with respect to the elastic axis.

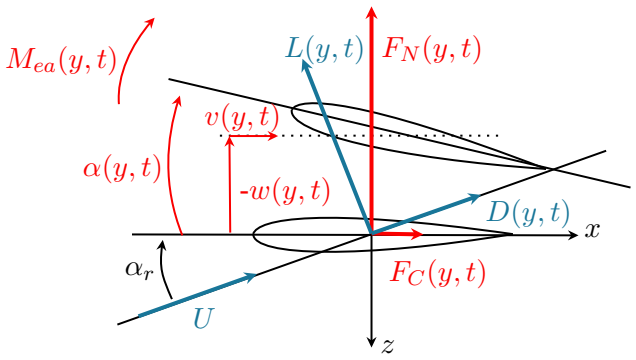


**Figure 2.1:** Schematic of the forces acting on the wing section.

### 2.1.2 Aeroelastic concepts

As previously explained, the focus is placed on flutter-type instabilities, which result from the interaction between aerodynamic forces and the structural dynamics of flexible lifting surfaces. Fluid–structure interactions can also give rise to static instabilities, such as divergence, which is not associated with oscillatory motion. For both cases, the structural response becomes unstable beyond a critical velocity, leading to growing response that may eventually reach a limited amplitude if restraining non-linearities are present. However, the critical velocity for divergence is typically much higher than the flutter speed. As a result, divergence is rarely encountered in practice, especially for well-designed aircraft wings, and is therefore not considered a primary concern in the present work.

#### Flutter phenomenon

Flutter can be defined as an unstable, self-excited structural oscillation at a definite frequency where energy is extracted from the airstream by the motion of the structure. Beyond a certain critical airspeed, the oscillations can grow in amplitude and potentially lead to structural failure. It is arguably the most important of all the aeroelastic phenomena and is the most difficult to predict (Wright & Cooper 2008).

One common approach to studying the onset of flutter is through the analysis of the system's damping ratio as a function of airspeed. As the flow velocity increases, the aerodynamic forces may reduce the effective damping of some vibration modes. Flutter occurs when the damping ratio of a mode drops to zero and becomes negative, indicating that energy is being fed into the system rather than dissipated. Tracking the evolution of modal damping with respect to airspeed therefore provides an estimation of the critical speed at which flutter begins. This is illustrated in Figure 2.2.

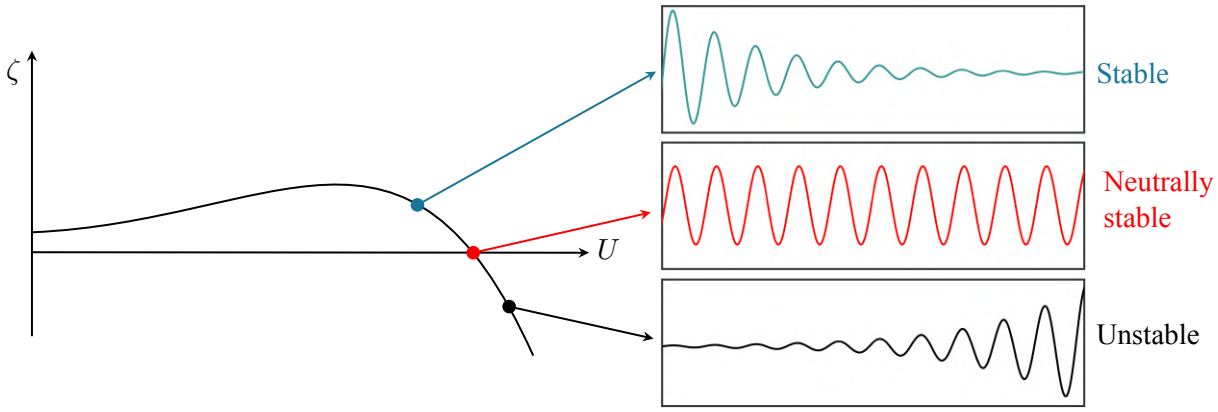


**Figure 2.2:** Evolution of damping ratios illustrating different aeroelastic stability regimes, reproduced from Verstraelen (2018).

In addition to identifying the onset of flutter, it is also important to understand the nature of the instability. Flutter can manifest in different forms depending on how the system behaves as it approaches and crosses the critical airspeed. In the case of soft flutter, the damping decreases progressively with increasing airspeed until it crosses zero, leading to a gradual onset of instability. In contrast, hard flutter is characterized by a sudden drop in damping, where the system transitions abruptly from a stable to an unstable state.

Another possible scenario is the appearance of a hump mode, in which the damping decreases with airspeed, crosses zero to enter an unstable regime, and then increases again at higher speeds, potentially returning the system to a stable state. In this case, flutter occurs only within a limited range of velocities, making its detection and analysis more complex. The different scenarios are shown in Figure 2.3.

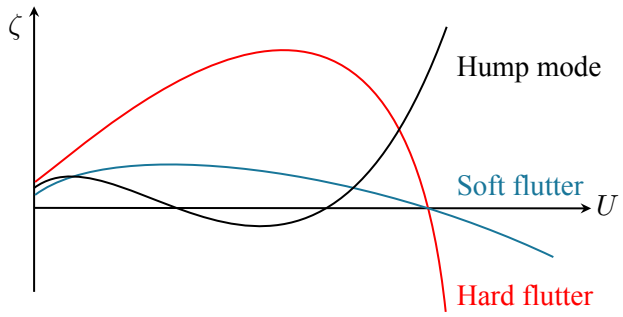


**Figure 2.3:** Evolution of damping ratios for different types of flutter.

The most commonly observed type of flutter in aircraft wings is the bending-torsion flutter. This aeroelastic instability arises from the coupling between bending and torsional modes, whose natural frequencies are often close to each other. In this work, the elastic axis and the inertial axis are intentionally not aligned, which promotes this interaction. Various configurations can be encountered, as illustrated in Figure 2.4.

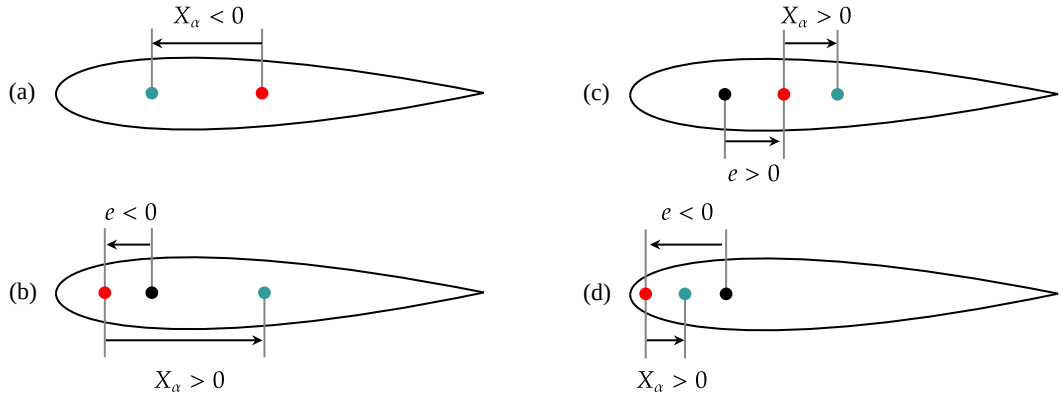


**Figure 2.4:** Configurations leading to coupled-mode flutter. Elastic axis (●) , inertial axis (●) and aerodynamic axis (●) are represented.

These configurations illustrate the conditions under which the wing may experience flutter in the case of a 2-DOFs system. Configuration (a) represents a case where the inertial axis lies upstream of the elastic axis. This is an unconditionally stable setup, meaning that flutter cannot occur. In contrast, configuration (b) corresponds to an unconditionally unstable configuration, which will always exhibit flutter at a certain velocity. Configurations (c) and (d), however, are conditionally stable. Flutter occurs only if specific criteria involving frequency ratio and mass distribution are met. The critical conditions for flutter in

these cases are given by

$$\begin{aligned} \left(\frac{f_w}{f_\alpha}\right)^2 &\leq \frac{X_\alpha + e}{e\left(1 + \dfrac{mX_\alpha e}{I_\alpha}\right)}, && \text{for (c)} \\ \left(\frac{f_w}{f_\alpha}\right)^2 &> \frac{X_\alpha + e}{e\left(1 + \dfrac{mX_\alpha e}{I_\alpha}\right)} \quad \text{and} \quad \left(1 + \frac{mX_\alpha e}{I_\alpha}\right) \leq 0, && \text{for (d)} \end{aligned} \tag{2.3}$$

where $f_w$ and $f_\alpha$ denote the bending and torsion natural frequencies, respectively, $m$ is the mass per unit length, $I_\alpha$ is the mass moment of inertia per unit length, $e$ is the distance from the aerodynamic axis to the elastic axis, and $X_\alpha$ is the distance between the elastic axis and the inertial axis.

## 2.2 Aeroelastic model

This work focuses on slender wings as illustrated in Figure 2.5. The system consists of the wing itself and a movable tip mass mechanism, which allows for adjustment of the structure's dynamic properties, especially its frequency contents.

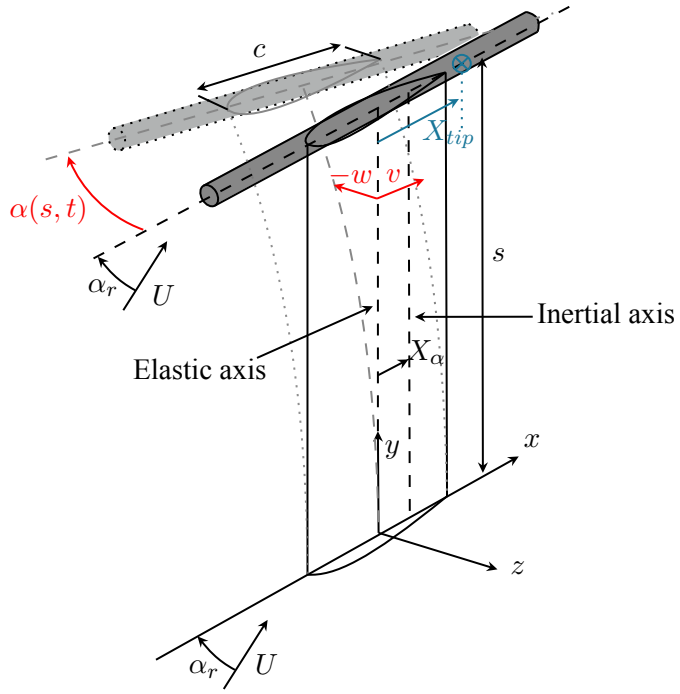


**Figure 2.5:** Schematic of the considered model: The dotted grey representation illustrates the deformed configuration. Red annotations indicate the different degrees of freedom of the system, while blue annotations highlight the adjustable mass located at the tip.

The model relies on some assumptions. Specifically, the absence of chordwise deformation was considered, *i.e.* $v \simeq 0$. Moreover, the effect of rotary inertia in the bending plane due to the tip mass was neglected, as $I_{tz}\ddot{w}' \simeq 0$. Furthermore, the dynamics are governed by linear equations of motion, which are expressed as

$$\begin{aligned} &\left(m + M_t\delta\right)\ddot{w} + c_w\dot{w} + \left(EI_x w''\right)'' + \left(mX_\alpha + M_t\delta X_\alpha\right)\ddot{\alpha} = -F_N, \\ &\left(I_\alpha + I_{ty}\delta\right)\ddot{\alpha} + c_\alpha\dot{\alpha} - \left(GJ\alpha'\right)' + \left(mX_\alpha + M_t\delta X_\alpha\right)\ddot{w} = M_{ea}, \\ &\delta = \delta\left(y - s\right), \end{aligned} \tag{2.4}$$

where $w(y,t)$ represents the displacement of the elastic axis, which is positively defined along the $z$-axis, $\alpha(y,t)$ denotes the rotation about the elastic axis, which is considered positive when evolving clockwise at the upper leading edge, $F_N(y,t)$ corresponds to the distributed normal force, which is aligned with the negative $z$-axis, $M_{ea}(y,t)$ represents the distributed moment about the elastic axis, and $\delta$ is the Dirac function.

### 2.2.1 Rayleigh–Ritz Method

It has been observed that the exact approach is satisfactory for simple systems but is rendered impractical for real systems exhibiting more complex behaviour. In this context, the Rayleigh–Ritz method is employed to represent the system's deformation by a finite series of assumed mode shapes, each multiplied by an unknown coefficient, as

$$w(y,t) = \sum_{i=1}^{N_w} \phi_{w,i}(y) q_{w,i}(t) \quad \text{and} \quad \alpha(y,t) = \sum_{j=1}^{N_\alpha} \phi_{\alpha,j}(y) q_{\alpha,j}(t), \tag{2.5}$$

where $N_w$ and $N_\alpha$ indicate the numbers of selected bending and torsion modes, respectively. When dealing with a continuous system, an infinite number of normal modes theoretically exist. However, in practice, the analysis is limited to a finite number of modes, denoted by $N_w + N_\alpha$. Consequently, the analysis provides estimates of $N_w + N_\alpha$ modes, with higher accuracy generally achieved for the lower-frequency modes (Wright & Cooper 2008). Since the structural dynamics are predominantly governed by the internal structure of the system, the mode shapes of a uniform cantilever beam are adopted as the assumed solutions. Regarding the bending modes, the solution provided by Meirovitch (2010) is employed, and it is expressed as

$$\begin{aligned}
\phi_{w,n}(y) &= A_n \left[ (\sin \beta_{w,n} y - \sinh \beta_{w,n} y) - \gamma_n \left( \cos \beta_{w,n} y - \cosh \beta_{w,n} y \right) \right], \\
\phi'_{w,n}(y) &= A_n \beta_{w,n} \left[ (\cos \beta_{w,n} y - \cosh \beta_{w,n} y) - \gamma_n \left( -\sin \beta_{w,n} y - \sinh \beta_{w,n} y \right) \right], \\
\phi''_{w,n}(y) &= -A_n \beta_{w,n}^2 \left[ (\sin \beta_{w,n} y + \sinh \beta_{w,n} y) - \gamma_n \left( \cos \beta_{w,n} y + \cosh \beta_{w,n} y \right) \right], \\
\gamma_n &= \frac{\sin \beta_{w,n} s + \sinh \beta_{w,n} s}{\cos \beta_{w,n} s + \cosh \beta_{w,n} s}.
\end{aligned} \tag{2.6}$$

In this formulation, $\beta_{w,n}$ is determined according to the selected configuration, and $A_n$ serves as a normalization factor. Specifically, $A_n$ is defined to ensure modal mass normalization, such that the associated mode shape has a unit modal mass. For the configuration without a tip mass, the values of $\beta_{w,n}s$ are determined as the solutions of the characteristic equation

$$\cos(\beta_{w,n} s)\, \cosh(\beta_{w,n} s) + 1 = 0. \tag{2.7}$$

For the configuration with a lumped mass $M_t$ at the tip, the values of $\beta_{w,n}s$ are obtained by solving the characteristic equation

$$1 + \cos(\beta_{w,n} s) \cosh(\beta_{w,n} s) + \frac{M_t}{ms} \beta_{w,n} s \left[ \sinh(\beta_{w,n} s) \cos(\beta_{w,n} s) - \sin(\beta_{w,n} s) \cosh(\beta_{w,n} s) \right] = 0. \tag{2.8}$$

Concerning the torsion modes, the following expressions were proposed by Meirovitch (2010):

$$\begin{aligned}
\phi_{\alpha,n}(y) &= \sin(\beta_{\alpha,n} y), \\
\phi'_{\alpha,n}(y) &= \beta_{\alpha,n} \cos(\beta_{\alpha,n} y), \\
\phi''_{\alpha,n}(y) &= -\beta_{\alpha,n}^2 \sin(\beta_{\alpha,n} y).
\end{aligned} \tag{2.9}$$

Here, $\beta_{\alpha,n}$ is determined according to the chosen configuration. In the absence of a tip mass, the values

of $\beta_{\alpha,n}s$ are determined as the solutions of the characteristic equation

$$\cos(\beta_{\alpha,n}s) = 0. \tag{2.10}$$

Concerning the configuration with a tip mass, the values of $\beta_{\alpha,n}s$ are obtained by solving the characteristic equation

$$\tan(\beta_{\alpha,n}s) = \frac{I_\alpha s}{I_{ty}} \frac{1}{\beta_{\alpha,n}s}. \tag{2.11}$$

### 2.2.2 Structural matrices

The equations of motion described in Equation 2.4 can be expressed in matrix form by introducing the modal expansion proposed by the Rayleigh–Ritz method in Equation 2.5. Then, the first equation is multiplied by $\phi_{w,I}$ for $I = 1, \dots, N_w$ and integrated along the span, while the second equation is multiplied by $\phi_{\alpha,J}$ for $J = 1, \dots, N_\alpha$ and integrated along the span, which yields

$$\begin{aligned}
&\sum_{i=1}^{N_w} \ddot{q}_{w,i} \left[ \int_0^s m\phi_{w,I}\phi_{w,i}\mathrm{d}y + M_t\phi_{w,I}(s)\phi_{w,i}(s) \right] + \sum_{j=1}^{N_\alpha} \ddot{q}_{\alpha,j} \left[ \int_0^s mX_\alpha\phi_{w,I}\phi_{\alpha,j}\mathrm{d}y + M_tX_t\phi_{w,I}(s)\phi_{\alpha,j}(s) \right] \\
&\qquad + \sum_{i=1}^{N_w} \dot{q}_{w,i} \left[ \int_0^s c_{w,i}\phi_{w,I}\phi_{w,i}\mathrm{d}y \right] + \sum_{i=1}^{N_w} q_{w,i} \left[ \int_0^s \phi_{w,I} \left( EI_x\phi''_{w,i} \right)'' \mathrm{d}y \right] = -\int_0^s F_N\phi_{w,I}\mathrm{d}y, \\
&\sum_{j=1}^{N_\alpha} \ddot{q}_{\alpha,j} \left[ \int_0^s I_\alpha\phi_{\alpha,J}\phi_{\alpha,j}\mathrm{d}y + I_{ty}\phi_{\alpha,J}(s)\phi_{\alpha,j}(s) \right] + \sum_{i=1}^{N_w} \ddot{q}_{w,i} \left[ \int_0^s mX_\alpha\phi_{\alpha,J}\phi_{w,i}\mathrm{d}y + M_tX_t\phi_{\alpha,J}(s)\phi_{w,i}(s) \right] \\
&\qquad + \sum_{j=1}^{N_\alpha} \dot{q}_{\alpha,j} \left[ \int_0^s c_{\alpha,j}\phi_{\alpha,J}\phi_{\alpha,j}\mathrm{d}y \right] - \sum_{j=1}^{N_\alpha} q_{\alpha,j} \left[ \int_0^s \phi_{\alpha,J} \left( GJ\phi'_{\alpha,j} \right)' \mathrm{d}y \right] = \int_0^s M\phi_{\alpha,J}\mathrm{d}y.
\end{aligned} \tag{2.12}$$

The boundary conditions for the cantilever beam, under the assumption that $EI_x$ is independent of $y$, are introduced as follows

$$\begin{cases} w(0,t) &= \frac{\partial w}{\partial y}(0,t) = 0, \quad \frac{\partial^2 w}{\partial y^2}(s,t) = \frac{\partial^4 w}{\partial y^4}(s,t) = 0, \\ \alpha(0,t) &= 0, \quad \frac{\partial \alpha}{\partial y}(s,t) = 0. \end{cases} \tag{2.13}$$

Under these assumptions and by employing integration by parts, the stiffness component of the expression is simplified as

$$\begin{aligned}
\int_0^s \phi_{w,I} \left( EI_x\phi''_{w,i} \right)'' \mathrm{d}y &= \int_0^s EI_x\phi''_{w,I}\phi''_{w,i}\mathrm{d}y, \\
-\int_0^s \phi_{\alpha,J} \left( GJ\phi'_{\alpha,j} \right)' \mathrm{d}y &= \int_0^s GJ\phi'_{\alpha,J}\phi'_{\alpha,j}\mathrm{d}y.
\end{aligned} \tag{2.14}$$

Afterwards, the system can be written with matrix formulation as

$$\mathbf{M}_S\ddot{Q} + \mathbf{C}_S\dot{Q} + \mathbf{K}_SQ = F_A \quad \text{with} \quad Q = \left[ q_{w,1}(t) \dots q_{w,N_w}(t)\ q_{\alpha,1}(t) \dots q_{\alpha,N_\alpha}(t) \right]^T, \tag{2.15}$$

where $F_A$ represents the aerodynamic contribution, further detailed in subsection 2.2.3. The structural mass $\mathbf{M}_S$, damping $\mathbf{C}_S$, and stiffness $\mathbf{K}_S$ matrices are obtained by isolating the terms involving $Q$ and its time derivatives.

**Mass matrix**

The mass matrix is constructed as

$$\mathbf{M}_S = \begin{bmatrix} [\mathbf{M}_{ww} + \mathbf{M}_{wwT}]_{N_w \times N_w} & [\mathbf{M}_{w\alpha} + \mathbf{M}_{w\alpha T}]_{N_w \times N_\alpha} \\ [\mathbf{M}_{\alpha w} + \mathbf{M}_{\alpha wT}]_{N_\alpha \times N_w} & [\mathbf{M}_{\alpha\alpha} + \mathbf{M}_{\alpha\alpha T}]_{N_\alpha \times N_\alpha} \end{bmatrix}, \tag{2.16}$$

where each submatrix results from the integration of the corresponding mass contributions associated with bending and torsional degrees of freedom. The structural mass contributions from the wing are expressed as

$$\begin{aligned} [\mathbf{M}_{ww}]_{N_w \times N_w} &= \left( \int_0^s m \phi_{w,i} \phi_{w,j} \mathrm{d}y \right)_{\substack{1 \le i \le N_w \\ 1 \le j \le N_w}}, \\ [\mathbf{M}_{w\alpha}]_{N_w \times N_\alpha} = [\mathbf{M}_{\alpha w}]^T_{N_\alpha \times N_w} &= \left( \int_0^s m X_\alpha \phi_{w,i} \phi_{\alpha,j} \mathrm{d}y \right)_{\substack{1 \le i \le N_w \\ 1 \le j \le N_\alpha}}, \\ [\mathbf{M}_{\alpha\alpha}]_{N_\alpha \times N_\alpha} &= \left( \int_0^s I_\alpha \phi_{\alpha,i} \phi_{\alpha,j} \mathrm{d}y \right)_{\substack{1 \le i \le N_\alpha \\ 1 \le j \le N_\alpha}}. \end{aligned} \tag{2.17}$$

Since the elements of the mass matrix are constructed using the assumed mode shapes that discretize the wing, this same discretization can be used to include local contributions. In this context, the effect of the wing tip is accounted for by evaluating the corresponding expressions at the tip position $y = s$. It writes

$$\begin{aligned} [\mathbf{M}_{wwT}]_{N_w \times N_w} &= (M_t \phi_{w,i}(s) \phi_{w,j}(s))_{\substack{1 \le i \le N_w \\ 1 \le j \le N_w}}, \\ [\mathbf{M}_{w\alpha T}]_{N_w \times N_\alpha} = [\mathbf{M}_{\alpha wT}]^T_{N_\alpha \times N_w} &= (M_t X_t \phi_{w,i}(s) \phi_{\alpha,j}(s))_{\substack{1 \le i \le N_w \\ 1 \le j \le N_\alpha}}, \\ [\mathbf{M}_{\alpha\alpha T}]_{N_\alpha \times N_\alpha} &= (I_{ty} \phi_{\alpha,i}(s) \phi_{\alpha,j}(s))_{\substack{1 \le i \le N_\alpha \\ 1 \le j \le N_\alpha}}. \end{aligned} \tag{2.18}$$

**Stiffness matrix**

The stiffness matrix is constructed as

$$\mathbf{K}_S = \begin{bmatrix} [\mathbf{K}_{ww}]_{N_w \times N_w} & [\mathbf{0}]_{N_w \times N_\alpha} \\ [\mathbf{0}]_{N_\alpha \times N_w} & [\mathbf{K}_{\alpha\alpha}]_{N_\alpha \times N_\alpha} \end{bmatrix} \tag{2.19}$$

where each submatrix results from the integration of the corresponding stiffness contributions associated with bending and torsional degrees of freedom. It is worth noting that the material properties $EI_x$ and $GJ$ may be assumed constant along the span in the case of a uniform wing, but the formulation remains valid for spanwise-varying properties. The structural stiffness contributions from the wing are expressed as

$$\begin{aligned} [\mathbf{K}_{ww}]_{N_w \times N_w} &= \left( \int_0^s EI_x \phi_{w,i} \phi_{w,j} \mathrm{d}y \right)_{\substack{1 \le i \le N_w \\ 1 \le j \le N_w}}, \\ [\mathbf{K}_{\alpha\alpha}]_{N_\alpha \times N_\alpha} &= \left( \int_0^s GJ \phi_{\alpha,i} \phi_{\alpha,j} \mathrm{d}y \right)_{\substack{1 \le i \le N_\alpha \\ 1 \le j \le N_\alpha}}. \end{aligned} \tag{2.20}$$

### Damping matrix

The damping matrix is constructed as

$$\mathbf{C}_S = \begin{bmatrix} [\mathbf{C}_{ww}]_{N_w \times N_w} & [\mathbf{0}]_{N_w \times N_\alpha} \\ [\mathbf{0}]_{N_\alpha \times N_w} & [\mathbf{C}_{\alpha\alpha}]_{N_\alpha \times N_\alpha} \end{bmatrix} \tag{2.21}$$

where $[\mathbf{C}_{ww}]_{N_w \times N_w}$ and $[\mathbf{C}_{\alpha\alpha}]_{N_\alpha \times N_\alpha}$ are diagonal matrices whose components can be computed from the experimental identification of the structural modes damping ratios

$$\begin{aligned} \mathbf{C}_{ww}(i,i) &= 2\xi_{wi}\sqrt{K_{ww}(i,i)\left(M_{ww}(i,i) + M_{wwT}(i,i)\right)} \qquad i \in [1, N_w]\,, \\ \mathbf{C}_{\alpha\alpha}(j,j) &= 2\xi_{\alpha j}\sqrt{K_{\alpha\alpha}(j,j)\left(M_{\alpha\alpha}(j,j) + M_{\alpha\alpha T}(j,j)\right)} \qquad j \in [1, N_\alpha]\,. \end{aligned} \tag{2.22}$$

## 2.2.3 Aerodynamic matrices

This section focuses on modelling the aerodynamic contribution to the system's behaviour. In this framework, two aerodynamic models are considered: a quasi-steady model, which neglects the influence of the wake, and an unsteady model based on Theodorsen's theory, which accounts for wake effects.

### Quasi-steady model

The quasi-steady model assumes that aerodynamic forces respond instantaneously to structural motion, neglecting unsteady effects. Under this assumption, the aerodynamic load coefficients can be directly related to the wing's instantaneous deformation and motion such as

$$\begin{aligned} C_N &= \frac{\mathrm{d}C_N}{\mathrm{d}\alpha}\alpha = \frac{\mathrm{d}C_N}{\mathrm{d}\alpha}\left(\sum_{j=1}^{N_\alpha} \phi_{\alpha,j}(y) q_{\alpha,j}\right), \\ C_M &= \frac{\mathrm{d}C_M}{\mathrm{d}\alpha}\alpha = \frac{\mathrm{d}C_M}{\mathrm{d}\alpha}\left(\sum_{j=1}^{N_\alpha} \phi_{\alpha,j}(y) q_{\alpha,j}\right). \end{aligned} \tag{2.23}$$

These relations are then used to express the aerodynamic forces acting on the structure. Specifically, the aerodynamic force vector $F_A$, introduced in Equation 2.15 is written as

$$F_A = \begin{bmatrix} -\int_0^s F_N \phi_{w,1}\mathrm{d}y \\ \vdots \\ -\int_0^s F_N \phi_{w,N_w}\mathrm{d}y \\ \int_0^s M\phi_{\alpha,1}\mathrm{d}y \\ \vdots \\ \int_0^s M\phi_{\alpha,N_\alpha}\mathrm{d}y \end{bmatrix} = \frac{\rho U^2}{2} \begin{bmatrix} -\int_0^s cC_N \phi_{w,1}\mathrm{d}y \\ \vdots \\ -\int_0^s cC_N \phi_{w,N_w}\mathrm{d}y \\ \int_0^s c^2 C_M \phi_{\alpha,1}\mathrm{d}y \\ \vdots \\ \int_0^s c^2 C_M \phi_{\alpha,N_\alpha}\mathrm{d}y \end{bmatrix} = \frac{\rho U^2 c}{2} \begin{bmatrix} -\frac{\mathrm{d}C_N}{\mathrm{d}\alpha}\sum_{j=1}^{N_\alpha}\left(\int_0^s \phi_{\alpha,j}\phi_{w,1}\mathrm{d}y\right) q_{\alpha,j} \\ \vdots \\ -\frac{\mathrm{d}C_N}{\mathrm{d}\alpha}\sum_{j=1}^{N_\alpha}\left(\int_0^s \phi_{\alpha,j}\phi_{w,N_w}\mathrm{d}y\right) q_{\alpha,j} \\ c\frac{\mathrm{d}C_M}{\mathrm{d}\alpha}\sum_{j=1}^{N_\alpha}\left(\int_0^s \phi_{\alpha,j}\phi_{\alpha,1}\mathrm{d}y\right) q_{\alpha,j} \\ \vdots \\ c\frac{\mathrm{d}C_M}{\mathrm{d}\alpha}\sum_{j=1}^{N_\alpha}\left(\int_0^s \phi_{\alpha,j}\phi_{\alpha,N_\alpha}\mathrm{d}y\right) q_{\alpha,j} \end{bmatrix}. \tag{2.24}$$

This expression highlights how aerodynamic loads are projected onto the structural modal basis. The resulting formulation shows that the aerodynamic forces depend linearly on the modal amplitudes $q_{\alpha,j}$ and can therefore be interpreted as an aerodynamic stiffness contribution. This aerodynamic stiffness, denoted by $K_A$, is velocity-dependent and increases the total stiffness matrix. Introducing the shape

submatrices

$$
\begin{aligned}
[\mathbf{\Phi}_{ww}]_{N_w \times N_w} &= \left( \int_0^s \phi_{w,i} \phi_{w,j} \mathrm{d}y \right)_{\substack{1 \leq i \leq N_w \\ 1 \leq j \leq N_w}}, \quad [\mathbf{\Phi}_{w\alpha}]_{N_w \times N_\alpha} = \left( \int_0^s \phi_{w,i} \phi_{\alpha,j} \mathrm{d}y \right)_{\substack{1 \leq i \leq N_w \\ 1 \leq j \leq N_\alpha}}, \\
[\mathbf{\Phi}_{\alpha w}]_{N_\alpha \times N_w} &= \left( \int_0^s \phi_{\alpha,i} \phi_{w,j} \mathrm{d}y \right)_{\substack{1 \leq i \leq N_\alpha \\ 1 \leq j \leq N_w}}, \quad [\mathbf{\Phi}_{\alpha\alpha}]_{N_\alpha \times N_\alpha} = \left( \int_0^s \phi_{\alpha,i} \phi_{\alpha,j} \mathrm{d}y \right)_{\substack{1 \leq i \leq N_\alpha \\ 1 \leq j \leq N_\alpha}}.
\end{aligned}
\tag{2.25}
$$

These submatrices are then employed to express the aerodynamic force vector $F_A$ in a compact matrix form

$$
F_A = -\mathbf{K}_A Q = \frac{\rho U^2 c}{2} \begin{bmatrix} [\mathbf{0}]_{N_w \times N_w} & -\dfrac{\mathrm{d}C_N}{\mathrm{d}\alpha} [\mathbf{\Phi}_{w\alpha}] \\ [\mathbf{0}]_{N_\alpha \times N_w} & c \dfrac{\mathrm{d}C_M}{\mathrm{d}\alpha} [\mathbf{\Phi}_{\alpha\alpha}] \end{bmatrix} \begin{bmatrix} q_{w,1} \\ \vdots \\ q_{w,N_w} \\ q_{\alpha,1} \\ \vdots \\ q_{\alpha,N_\alpha} \end{bmatrix}. \tag{2.26}
$$

The added aerodynamic stiffness matrix can be written as

$$
\mathbf{K}_A = \frac{\rho U^2 c}{2} \begin{bmatrix} 0\,[\mathbf{\Phi}_{ww}] & \frac{\mathrm{d}C_N}{\mathrm{d}\alpha} [\mathbf{\Phi}_{w\alpha}] \\ 0\,[\mathbf{\Phi}_{\alpha w}] & -c \frac{\mathrm{d}C_M}{\mathrm{d}\alpha} [\mathbf{\Phi}_{\alpha\alpha}] \end{bmatrix}_{(N_w+N_\alpha)\times(N_w+N_\alpha)}. \tag{2.27}
$$

As previously stated, the quasi-steady model accounts only for added aerodynamic stiffness, neglecting aerodynamic damping. However, damping can be introduced in Equation 2.23 by replacing the geometric angle of attack with the effective angle of attack

$$
\alpha \to \alpha + \frac{\dot{w}}{U} + \left( \frac{1}{2} - a \right) \dot{\alpha}, \tag{2.28}
$$

which introduces time derivatives and thereby adds damping-like terms to the model. This approach has already been investigated by Wright & Cooper (2008). However, it has been shown that introducing damping in the quasi-steady model without incorporating unsteady aerodynamic effects can lead to non-physical or unreliable predictions, sometimes performing worse than the purely stiffness-based quasi-steady model. For this reason, the present study retains the quasi-steady model in its conservative form, including only the added aerodynamic stiffness as defined in Equation 2.27.

### Unsteady Theodorsen model

In unsteady aerodynamics, the reduced frequency is a key non-dimensional parameter that characterizes the relative importance of unsteady effects in oscillating flows. It is defined as

$$
k = \frac{\omega\, b}{U}, \tag{2.29}
$$

where $\omega$ is the oscillation pulsation of the structure, $b$ is the airfoil half chord length, and $U$ is the freestream velocity. Low values of $k$ correspond to slow structural motions where quasi-steady assumptions are valid, whereas higher $k$ values indicate significant unsteady aerodynamic effects.

To account for these effects in the modelling, several unsteady aerodynamic formulations have been proposed, among which the most widely used is that introduced by Theodorsen (1935). Based on the same fundamental assumptions as Glauert's theory, *i.e.* potential and incompressible flow with small perturbations in the relative wind, Theodorsen extended the analysis to unsteady motion by introducing the concept of a continuous vortex sheet shed from the trailing edge. The resulting vortex system, formed by spanwise-aligned vortices convected downstream, induces a velocity field that alters the local flow

around the airfoil. As a result, the boundary conditions and the pressure distribution are affected, leading to a modified expression for the aerodynamic loads. These loads are then corrected using the Theodorsen function $C(k)$, which is defined as

$$C(k) = \frac{K_1(ik)}{K_0(ik) + K_1(ik)} = F + iG, \tag{2.30}$$

where $K_0$ and $K_1$ are modified Bessel's function of the second kind. Approximate expression for $C(k)$ was proposed by Fung (1969) as

$$\begin{aligned} C(k) &= 1 - \frac{0.165}{1 - \frac{0.045}{k}i} - \frac{0.035}{1 - \frac{0.30}{k}i}, \quad k \leq 1/2, \\ &= 1 - \frac{0.165}{1 - \frac{0.041}{k}i} - \frac{0.035}{1 - \frac{0.32}{k}i}, \quad k > 1/2. \end{aligned} \tag{2.31}$$

The Theodorsen function is shown in Figure 2.6 as a function of the reduced frequency $k$. It highlights how unsteady aerodynamic effects are modelled, notably the phase lag at higher $k$ values. The amplitude also decreases with $k$, reaching about half its quasi-steady value at large reduced frequencies.

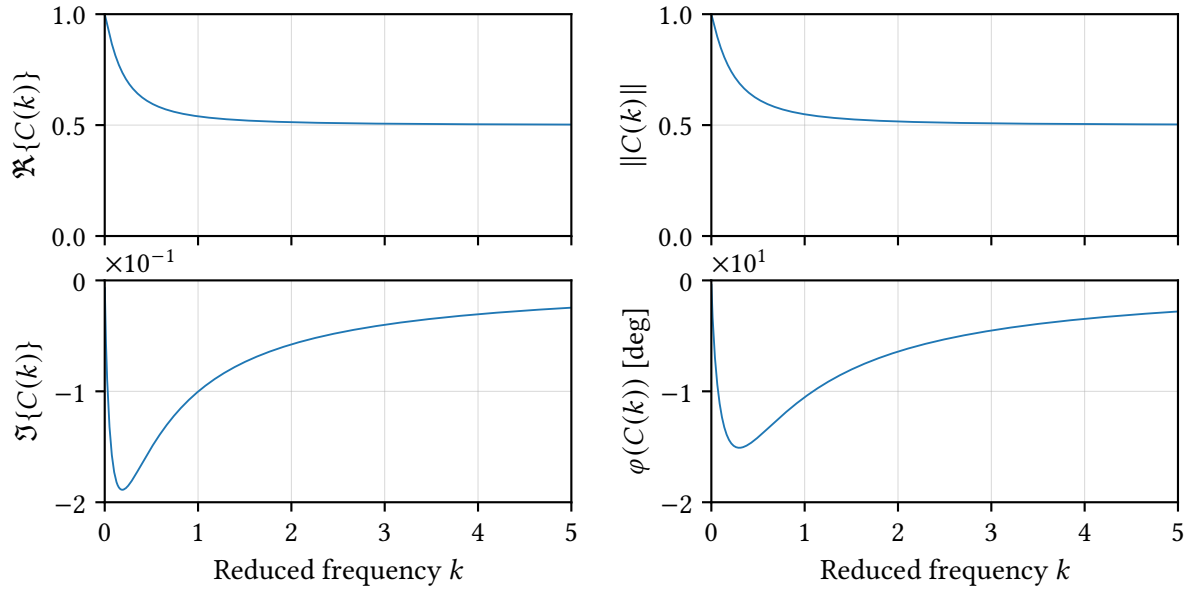


**Figure 2.6:** Real and imaginary components, amplitude, and phase of the Theodorsen function $C(k)$ as a function of the reduced frequency $k$.

The unsteady lift and moment coefficient can be expressed as

$$\begin{aligned} C_L &= \frac{\mathrm{d}C_L}{\mathrm{d}\alpha} C(k) \left[ \alpha + \frac{\dot{h}}{U} + \left( \frac{1}{2} - a \right) \frac{b}{U} \dot{\alpha} \right] + \pi \frac{b^2}{U^2} \left( \frac{\ddot{h}}{b} - a\ddot{\alpha} \right) + \pi \frac{b}{U} \dot{\alpha}, \\ C_M &= \frac{\mathrm{d}C_M}{\mathrm{d}\alpha} C(k) \left[ \alpha + \frac{\dot{h}}{U} + \left( \frac{1}{2} - a \right) \frac{b}{U} \dot{\alpha} \right] + \frac{\pi}{2} \frac{b^2}{U^2} \left[ a \frac{\ddot{h}}{b} - \left( \frac{1}{8} + a^2 \right) \ddot{\alpha} \right] - \frac{\pi}{2} \left( \frac{1}{2} - a \right) \frac{b}{U} \dot{\alpha}. \end{aligned} \tag{2.32}$$

This expression can be further developed by decomposing the Theodorsen function into its real and imag-

inary components. Using the notation proposed by Wright & Cooper (2008), one gets

$$\begin{aligned} L(t) &= \rho U^2 \left( L_w w + L_{\dot{w}} \frac{b\dot{w}}{U} + L_{\ddot{w}} \frac{b^2 \ddot{w}}{U^2} + L_\alpha b\alpha + L_{\dot{\alpha}} \frac{b^2 \dot{\alpha}}{U} + L_{\ddot{\alpha}} \frac{b^3 \ddot{\alpha}}{U^2} \right), \\ M(t) &= \rho U^2 b \left( M_w w + M_{\dot{w}} \frac{b\dot{w}}{U} + M_{\ddot{w}} \frac{b^2 \ddot{w}}{U^2} + M_\alpha b\alpha + M_{\dot{\alpha}} \frac{b^2 \dot{\alpha}}{U} + M_{\ddot{\alpha}} \frac{b^3 \ddot{\alpha}}{U^2} \right), \end{aligned} \tag{2.33}$$

where the velocity-independent notations are defined as

$$\begin{aligned} &L_{\ddot{w}} = \pi, && L_{\dot{w}} = \tfrac{\mathrm{d}C_L}{\mathrm{d}\alpha} F, && L_w = -\tfrac{\mathrm{d}C_L}{\mathrm{d}\alpha} kG, \\ &L_{\ddot{\alpha}} = -\pi a, && L_{\dot{\alpha}} = \tfrac{\mathrm{d}C_L}{\mathrm{d}\alpha} \left( F\left(\tfrac{1}{2} - a\right) + \tfrac{G}{k} \right) + \pi, && L_\alpha = \tfrac{\mathrm{d}C_L}{\mathrm{d}\alpha} \left( F - kG\left(\tfrac{1}{2} - a\right) \right), \\ &M_{\ddot{w}} = \pi a, && M_{\dot{w}} = 2\tfrac{\mathrm{d}C_M}{\mathrm{d}\alpha} F, && M_w = -2\tfrac{\mathrm{d}C_M}{\mathrm{d}\alpha} kG, \\ &M_{\ddot{\alpha}} = -\pi\left(\tfrac{1}{8} + a^2\right), && M_{\dot{\alpha}} = 2\tfrac{\mathrm{d}C_M}{\mathrm{d}\alpha} \left( F\left(\tfrac{1}{2} - a\right) + \tfrac{G}{k} \right) - \pi\left(\tfrac{1}{2} - a\right), && M_\alpha = 2\tfrac{\mathrm{d}C_M}{\mathrm{d}\alpha} \left( F - kG\left(\tfrac{1}{2} - a\right) \right). \end{aligned} \tag{2.34}$$

The aerodynamic force vector $F_A$ from Equation 2.15 can be written as

$$F_A = -\mathbf{K}_A Q - \mathbf{C}_A \dot{Q} - \mathbf{M}_A \ddot{Q}, \tag{2.35}$$

where the aerodynamic stiffness, damping, and mass matrices are formulated using the shape submatrices introduced in Equation 2.25 as follows

$$\begin{aligned} \mathbf{K}_A &= \rho U^2 \begin{bmatrix} L_w [\mathbf{\Phi}_{ww}] & L_\alpha b [\mathbf{\Phi}_{w\alpha}] \\ -M_w b [\mathbf{\Phi}_{\alpha w}] & -M_\alpha b^2 [\mathbf{\Phi}_{\alpha\alpha}] \end{bmatrix}, \\ \mathbf{C}_A &= \rho U^2 \begin{bmatrix} L_{\dot{w}} \frac{b}{U} [\mathbf{\Phi}_{ww}] & L_{\dot{\alpha}} \frac{b^2}{U} [\mathbf{\Phi}_{w\alpha}] \\ -M_{\dot{w}} \frac{b^2}{U} [\mathbf{\Phi}_{\alpha w}] & -M_{\dot{\alpha}} \frac{b^3}{U} [\mathbf{\Phi}_{\alpha\alpha}] \end{bmatrix} = \rho U b \begin{bmatrix} L_{\dot{w}} [\mathbf{\Phi}_{ww}] & L_{\dot{\alpha}} b [\mathbf{\Phi}_{w\alpha}] \\ -M_{\dot{w}} b [\mathbf{\Phi}_{\alpha w}] & -M_{\dot{\alpha}} b^2 [\mathbf{\Phi}_{\alpha\alpha}] \end{bmatrix}, \\ \mathbf{M}_A &= \rho U^2 \begin{bmatrix} L_{\ddot{w}} \frac{b^2}{U^2} [\mathbf{\Phi}_{ww}] & L_{\ddot{\alpha}} \frac{b^3}{U^2} [\mathbf{\Phi}_{w\alpha}] \\ -M_{\ddot{w}} \frac{b^3}{U^2} [\mathbf{\Phi}_{\alpha w}] & -M_{\ddot{\alpha}} \frac{b^4}{U^2} [\mathbf{\Phi}_{\alpha\alpha}] \end{bmatrix} = \rho b^2 \begin{bmatrix} L_{\ddot{w}} [\mathbf{\Phi}_{ww}] & L_{\ddot{\alpha}} b [\mathbf{\Phi}_{w\alpha}] \\ -M_{\ddot{w}} b [\mathbf{\Phi}_{\alpha w}] & -M_{\ddot{\alpha}} b^2 [\mathbf{\Phi}_{\alpha\alpha}] \end{bmatrix}. \end{aligned} \tag{2.36}$$

### 2.2.4 Aeroelastic analysis

Using the added aerodynamic matrices derived from the aerodynamic model, the equation of motion described in Equation 2.15 can be reformulated as

$$\mathbf{M}\ddot{Q} + \mathbf{C}\dot{Q} + \mathbf{K}Q = 0, \tag{2.37}$$

where $\mathbf{M} = \mathbf{M}_S + \mathbf{M}_A$, $\mathbf{C} = \mathbf{C}_S + \mathbf{C}_A$ and $\mathbf{K} = \mathbf{K}_S + \mathbf{K}_A$ represent the combined structural and aerodynamic mass, damping, and stiffness matrices, respectively. For numerical implementation and stability analysis, this second-order differential equation is commonly rewritten in state-space form. By introducing the state vector $X = \begin{bmatrix} \dot{Q} & Q \end{bmatrix}^T$, the system becomes

$$\begin{bmatrix} \ddot{Q} \\ \dot{Q} \end{bmatrix} = \begin{bmatrix} -\mathbf{M}^{-1}\mathbf{C} & -\mathbf{M}^{-1}\mathbf{K} \\ \mathbf{I} & \mathbf{0} \end{bmatrix} \begin{bmatrix} \dot{Q} \\ Q \end{bmatrix} \quad \Rightarrow \quad \dot{X} = \mathbf{A}X, \tag{2.38}$$

where $\mathbf{A}$ is the state matrix, whose eigenvalues govern the dynamic behaviour of the system. Let $\lambda = p + iq$ represent a generic eigenvalue of the system. The real and imaginary parts of $\lambda$ provide insight into the system's stability and dynamic behaviour. In particular, the imaginary part $q$ is related to the oscillation frequency, while the real part $p$ determines whether the mode grows or decays over time. The

modal frequency and damping ratio can be expressed as

$$f = \frac{|q|}{2\pi}\ [\text{Hz}] \quad , \quad \zeta = -\text{sign}\,(p)\left(1+\left(\frac{q}{p}\right)^2\right)^{-1/2} , \tag{2.39}$$

which are both velocity-dependent.

## 2.3 Model validation

As previously mentioned, this study is supported by experimental testing conducted on two wing configurations, tested respectively at the IAT and at the University of Liège. The first wing was designed and built during a previous work realised by Prieur (2023). It serves as the reference configuration for both the validation of the aeroelastic model and the parametric study presented in the following section.

The geometric and structural properties of the first wing is summarized in Table 2.1. The second wing was specifically developed to provide an additional dataset for this study. Its design and associated modelling will be presented in section 3.1.

Table 2.1: Geometric and structural properties of the first wing configuration, as defined by Prieur (2023).

| Name | Symbol | Value | Unit |
|---|---|---|---|
| Semi span | $s$ | 1.5 | m |
| Chord | $c$ | 0.2 | m |
| Distance between the leading edge and the elastic axis | $X_{ea}$ | $c/3$ | m |
| Distance between the leading edge and the inertia axis | $X_{cg}$ | $0.379\,c$ | m |
| Mass per unit length | $m$ | 2.4 | $\text{kg m}^{-1}$ |
| Moment of inertia (about the elastic axis) per unit length | $I_\alpha$ | $5.6 \times 10^{-3}$ | $\text{kg m}^2\,\text{m}^{-1}$ |
| Chordwise bending stiffness | $EI_z$ | 4189.7 | $\text{N m}^2$ |
| Flapwise bending stiffness | $EI_x$ | 366 | $\text{N m}^2$ |
| Torsional stiffness | $GJ$ | 78 | $\text{N m}^2$ |

Figure 2.7 presents the model predictions for both aerodynamic formulations, illustrating the evolution of natural frequencies and damping ratios as a function of freestream velocity. In both cases, no flutter onset is predicted within the investigated velocity range, as the damping remains positive and no transition toward instability is observed.

Experimental frequency measurements from Prieur (2023) are superimposed for comparison. The different colour intensities of the experimental markers correspond to different measurement datasets. It should be noted, however, that no identification procedure was used to extract the experimental results, which limits their precision and prevents the estimation of damping ratios. Nevertheless, the overall dynamic behaviour is expected to be reasonably represented, allowing for a meaningful comparison with the model predictions.

Overall, the unsteady Theodorsen model provides a better agreement with the experimental trends, while the quasi-steady formulation underestimates both torsional and bending frequencies at higher velocities, exhibiting a more rapid decay than observed experimentally.

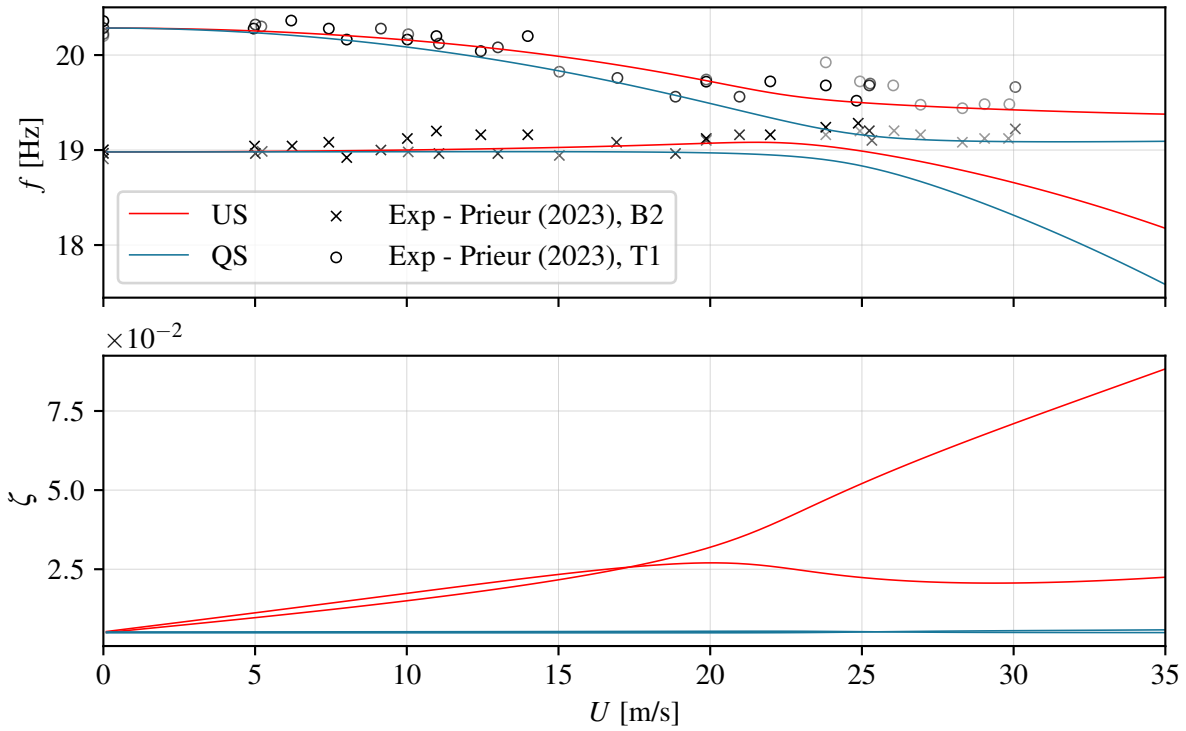


**Figure 2.7:** Evolution of the natural frequencies and aerodynamic damping ratios associated with the second bending (B2) and first torsion (T1) modes as a function of the freestream velocity $U$. Theoretical predictions are shown for both the quasi-steady (—) and unsteady Theodorsen (—) aerodynamic models. The computations are performed using the parameter set defined in Table 2.1, with structural damping ratios $\zeta_w = \zeta_\alpha = \zeta_v = 0.5\%$, lift-curve slope $\mathrm{d}C_L/\mathrm{d}\alpha = 4.9$, and pitching moment slope $\mathrm{d}C_M/\mathrm{d}\alpha = 0.5$ . Experimental data obtained from Prieur (2023) are overlaid.

### 2.3.1 Validation of orthogonality property

One can verify that the mode shapes are well defined and that they respect orthogonality properties. To this end, the Auto-MAC matrix is evaluated using the Modal Assurance Criterion computed between the theoretical mode shapes themselves. The criterion is presented in Equation 3.47. In this case, the MAC is applied to a single set of modes to assess their mutual independence. Ideally, the matrix should exhibit values of one along the diagonal and zeros elsewhere, indicating that the modes are orthogonal and linearly independent. Results are presented in Figure 2.8 where the diagonal element are close to 1, indicating reasonable mode independence.

## 2.4 Parametric study

This section presents a parametric study with the objective of identifying model configurations that promote the occurrence of flutter. The main parameter of interest is the predicted flutter speed, and the aim is to determine configurations that minimize this critical velocity.

The study is divided into two parts. The first focuses on the wing tip configuration, specifically analysing the influence of the tip mass $M_t$, the associated rotational inertia about the elastic axis $I_{ty}$, and the distance $X_t$ of the tip mass with respect to the elastic axis. This analysis seeks to better understand the underlying flutter mechanisms and how adjustments of the tip configuration can be used to influence the instability.

In the second part, a conceptual design phase is carried out to evaluate the effect of broader design parameters on the flutter speed. This investigation is intended to support future slender wing development by identifying design trends that can enhance aeroelastic performance.

It should be noted that the term ”optimal configuration” used in this section refers to the configuration

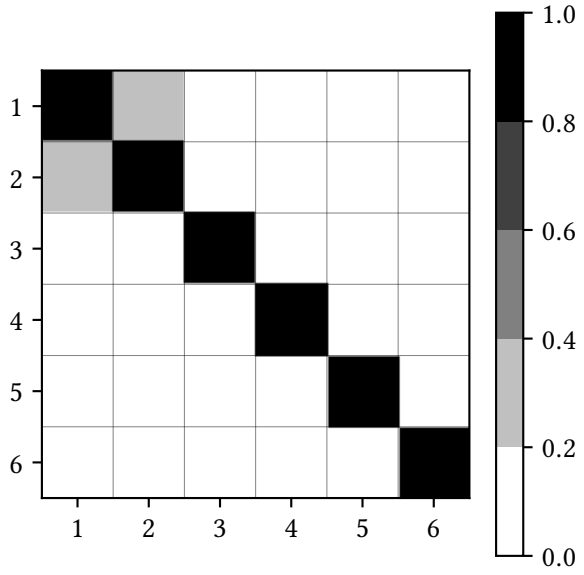


**Figure 2.8:** Auto-MAC matrix of the theoretical modes identified with the model.

that results in the minimum predicted flutter speed. While this configuration aligns with the objective of this study, it is not desirable in a practical design context. Therefore, the term ”optimal” should be interpreted strictly within the scope of this work.

### 2.4.1 Influence of wing tip configuration

This section aims to evaluate the evolution of the predicted flutter speed with respect to wing tip configuration. At this stage, only the tip mass $M_t$ and rotational inertia $I_{ty}$ are varied, with $X_t$ set to $0$. The addition of mass is expected to primarily affect the bending frequency, while the addition of inertia mainly influences the torsional frequency. Due to modal coupling, both modes are in fact affected. Furthermore, the addition of excessive rotational inertia at the wing tip can lead to a mode switching phenomenon, in which the two critical frequencies of interest invert. When such an inversion occurs, flutter between these two modes becomes impossible. As a result, an asymptotic behaviour of the flutter speed is expected as the added inertia increases.

Figure 2.9 shows the variation of the flutter speed as a function of the added torsional inertia $I_{ty}$ and the tip mass $M_t$. For clarity, three representative cuts corresponding to $M_t = 0.4$, $0.6$, and $0.8$ kg are displayed on the right. The results indicate that the flutter speed decreases approximately linearly with increasing $I_{ty}$ up to a critical point, beyond which it tends toward an asymptotic value. This trend is consistent with the expected modal decoupling associated with frequency inversion.

Moreover, it is observed that this inversion occurs at higher values of torsional inertia as the tip mass increases. This behaviour is physically consistent, as larger tip masses lower the bending-mode frequencies, thereby increasing the frequency separation between the bending and torsional modes and delaying their potential interaction.

Another observation is that, for each tip mass, the flutter speed exhibits a local minimum with respect to $I_{ty}$, suggesting the existence of an optimal configuration for which the flutter speed is minimized. This optimal condition is highlighted by the dashed red curve. From a design standpoint, this implies that reaching such a configuration experimentally requires careful tuning. A practical strategy consists in initially selecting a wing tip configuration that places the system within the linear, decreasing region of the flutter response, and then incrementally adjusting the mass and inertia toward the optimal point.

It should be note, however, that this analysis addresses only the predicted flutter speed and does not provide insight into the nature of the instability. In particular, the distinction between soft and hard flutter

is not captured within this framework.

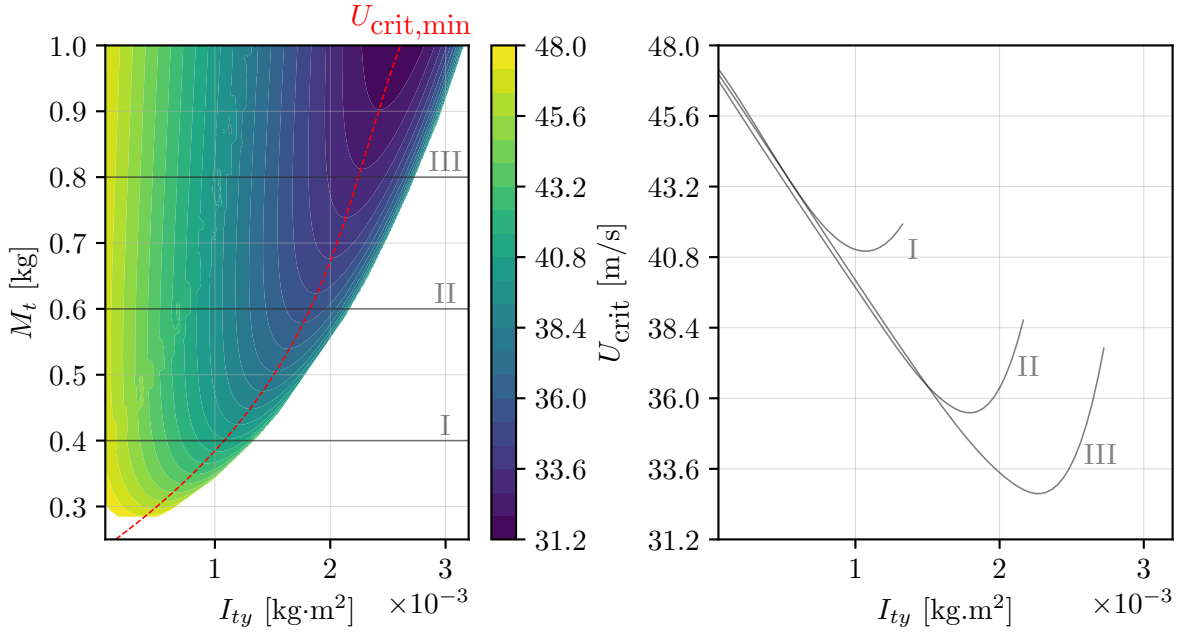


**Figure 2.9:** Contour representation of the critical flutter velocity $U_{\text{crit}}$ as a function of rotational inertia $I_{ty}$ and tip mass $M_t$ (left), where the dashed red curve denotes the evolution of the minimum critical velocity $U_{\text{crit,min}}$, and horizontal dashed lines identify three operating regions labelled I to III. The corresponding evolution of $U_{\text{crit}}$ with respect to $I_{ty}$ is shown for each selected value of $M_t$ (right). Results computed for centred configuration $X_t = 0\,\text{m}$.

### Impact of $X_t$

Additionally, the influence of the chordwise position of the wing tip mass with respect to the elastic axis was investigated. This parameter can be easily adjusted in practice through the use of wing tip configurations that incorporate movable mass compartments.

Figure 2.10 illustrates the variation of the minimum predicted flutter speed as a function of the tip mass position along the chord, measured relative to the elastic axis located at $c/3$. The mass was shifted from $-c/3$ to $2c/3$, covering positions both ahead of and behind the elastic axis. An optimal configuration for flutter onset is predicted slightly aft of the elastic axis.

The aeroelastic stability of the system is strongly influenced by the chordwise location of the tip mass. When the mass is placed ahead of the elastic axis ($X_t < 0$), the critical flutter speed increases nearly linearly. This trend is associated with a reduced coupling between bending and torsion, while the system remains potentially prone to flutter. Conversely, when the mass is positioned behind the elastic axis ($X_t > 0$), an asymptotic increase in flutter speed is observed. This stabilizing effect can be interpreted as the result of opposing contributions from the elastic restoring moment and the inertial moment induced by the mass, which increasingly counteract each other as the mass is moved further aft. Beyond a certain point, this opposition suppresses the dynamic coupling mechanism required to trigger flutter, leading to a fundamentally stable configuration.

An initial conclusion might suggest increasing the tip mass to reduce the critical flutter speed, thereby facilitating its onset during experimental testing. However, this approach is rather simplistic and may not be the most effective solution. The next section explores alternative design options that aim to reduce the minimum flutter speed in a more efficient way and improve the chances of observing the phenomenon in practice.

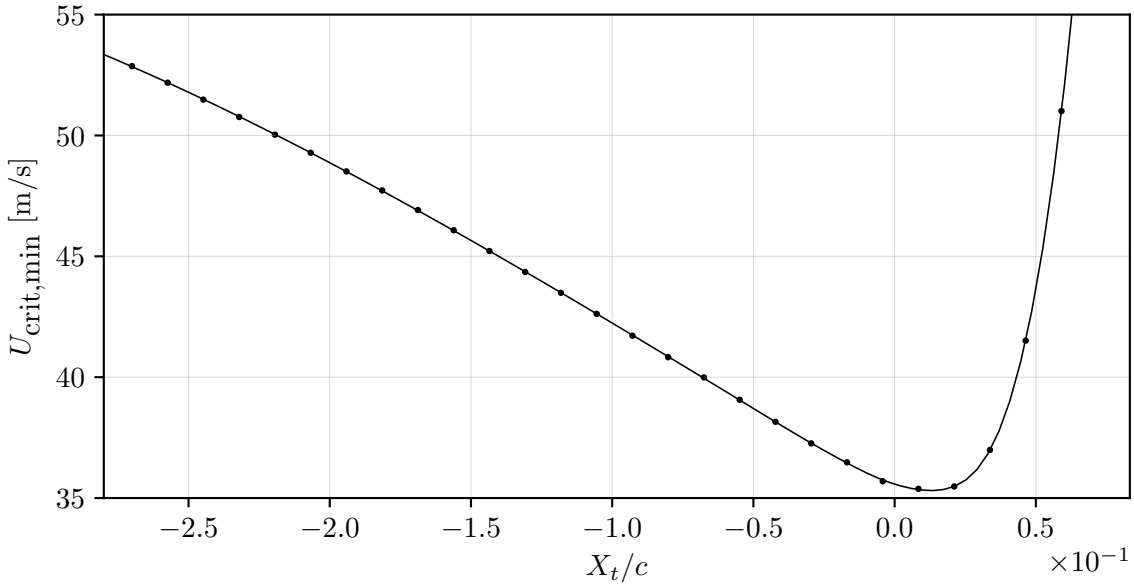


**Figure 2.10:** Evolution of the minimum flutter speed $U_{\text{crit,min}}$ as a function of the normalized wing tip mass location $X_t/c$. Results shown for $M_t = 0.6\,\text{kg}$.

### 2.4.2 Influence of design parameters

As previously introduced, this section aims to explore alternative design strategies. In this context, the analysis focuses on geometric parameters such as the aspect ratio ($AR$) and the position of the elastic axis $X_{ea}$. These parameters are selected because they can be more easily adjusted during the design and manufacturing process, unlike other parameters such as stiffness or structural inertia, which are more difficult to control directly.

#### Impact of Aspect Ratio

A first investigation focuses on the effect of the aspect ratio $AR$ on the flutter characteristics. The reference model tested at the Iat facility corresponds to a half-wing with a span of $1.5\,\text{m}$ and a chord of $0.2\,\text{m}$, yielding an aspect ratio $AR = 15$. In this parametric study, the chord length is kept constant while the span is varied to modify $AR$.

Figure 2.11 presents a contour representation of the predicted flutter speed $U_{\text{crit}}$ as a function of the added rotational inertia $I_{ty}$ and tip mass $M_t$, for two representative aspect ratios ($AR = 13$ and $AR = 20$). Each dashed horizontal line identifies a fixed mass case ($I$ to $III$), while the red dashed curve highlights the minimum flutter speed $U_{\text{crit,min}}$ for each mass value. The results reveal a strong dependence of the flutter boundary on the aspect ratio. As $AR$ increases, flutter occurs at lower tip mass values and the minimum flutter speed tends to decrease. This is consistent with the enhanced aerodynamic sensitivity of high $AR$ wings, which are more prone to aeroelastic instabilities due to their increased span and lift-curve slope. To account for this aerodynamic effect, the lift-curve slope used in the model is corrected following the formulation proposed by Glauert (1926), which adjusts the three-dimensional lift coefficient as

$$a = \frac{a_0}{1 + \frac{a_0}{\pi AR}(1+\tau)}, \tag{2.40}$$

where $a = \mathrm{d}C_L/\mathrm{d}\alpha$ is the corrected three-dimensional lift slope, $a_0$ is the two-dimensional lift curve slope, $AR$ is the wing's aspect ratio, and $\tau = 0.3$ is a correction factor accounting for the wing's geometry.

A more detailed comparison is shown in Figure 2.12, where the predicted flutter speed $U_{\text{crit}}$ (left) and the frequency ratio $f_w/f_\alpha$ (right) are plotted as functions of $I_{ty}$ for different aspect ratios, considering configuration $II$ ($M_t = 0.6\,\text{kg}, X_t = 0$). The results reveal a reduced slope in the linear region of the

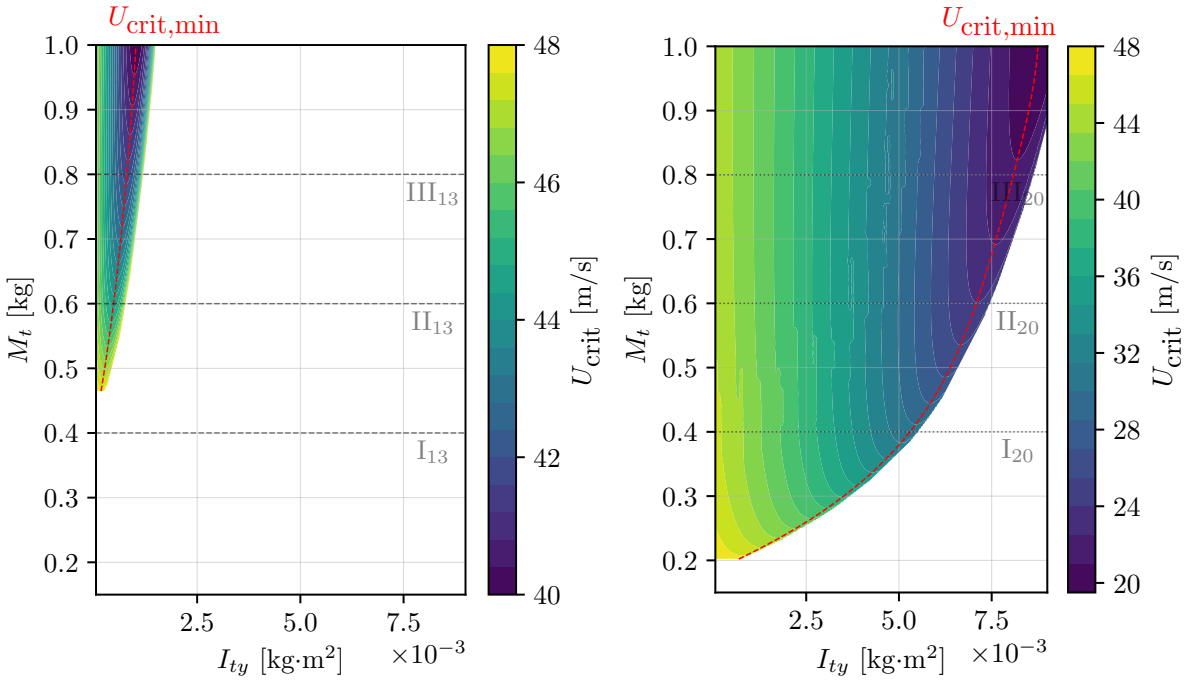


**(a)** $AR = 13$. **(b)** $AR = 20$.

**Figure 2.11:** Contour representation of the critical flutter velocity $U_{\text{crit}}$ as a function of rotational inertia $I_{ty}$ and tip mass $M_t$, where the dashed red curve denotes the evolution of the minimum critical velocity $U_{\text{crit,min}}$, and horizontal dashed lines identify three operating regions labelled I to III.

flutter speed curves as the aspect ratio increases. This reduction implies that the optimal configuration becomes easier to reach, as a broader range of $I_{ty}$ values leads to flutter speeds close to the minimum. In practice, this increases the robustness of the design with respect to tip inertia tuning, making the instability more accessible during experimental testing.

Furthermore, it can be observed that the optimal configuration shifts toward higher values of rotational inertia $I_{ty}$ as the aspect ratio increases. In this context, the increase in $AR$ not only enhances aerodynamic sensitivity but also alters the dynamic balance between bending and torsional modes. Specifically, increasing the aspect ratio tends to reduce the bending natural frequencies more significantly than the torsional ones, primarily due to the enhanced spanwise flexibility. As shown in the right subfigure of Figure 2.12, this results in an increased frequency gap between the bending and torsional modes. Consequently, a larger added rotational inertia $I_{ty}$ is required at the wing tip to bring the two modes into closer proximity, thereby enabling the modal interaction necessary for flutter to occur. This phenomenon explains the observed shift in the optimal $I_{ty}$ toward higher values as $AR$ increases.

### Impact of elastic axis location

The previous results were obtained for an elastic axis located at $X_{ea} = c/3$ and a centre of gravity at $X_{cg} = 0.379\,c$. In the current design, the position of the elastic axis was prescribed during the design process, as it is defined by the location of the internal beam within the cross section. In contrast, the inertial axis, coinciding with the centre of gravity, was determined from the CAD model based on the geometric layout and material density distribution used during 3D printing. This section aims to evaluate the influence of the elastic axis location on the minimum flutter speed. To isolate this effect, the inertial axis was kept fixed throughout the analysis. Modifying both simultaneously would introduce additional coupling effects and could lead to non-physical interpretations.

Figure 2.13 shows the evolution of minimum flutter speed as a function of the elastic axis location along the chord. As predicted by theoretical models, flutter interaction between bending and torsion modes

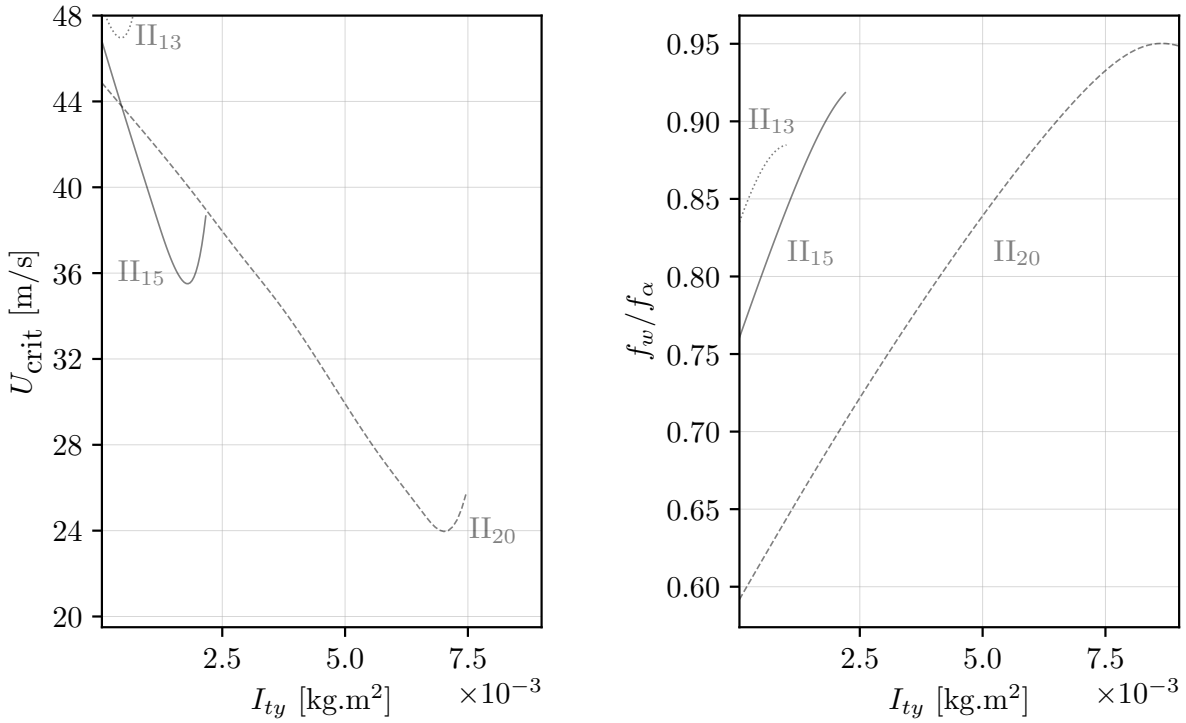


**Figure 2.12:** Evolution of the predicted flutter speed $U_{\text{crit}}$ (left) and the corresponding frequency ratio $f_w/f_\alpha$ (right) as functions of the added rotational inertia $I_{ty}$ of the wing tip about the elastic axis. Each curve corresponds to a different aspect ratio $AR$, with all cases computed for a centred tip mass ($X_t = 0$) and fixed mass $M_t = 0.6\,\text{kg}$ (configuration II).

becomes impossible when the elastic axis lies behind the inertial axis. In this configuration, an asymptotic behaviour is observed as the elastic axis approaches the inertial axis location. This stabilizing effect results from the counteracting contributions of the elastic restoring moment and the inertial moment, which tend to suppress the dynamic coupling required to trigger flutter. This principle underlies the concept of mass balancing in aircraft components that are susceptible to flutter.

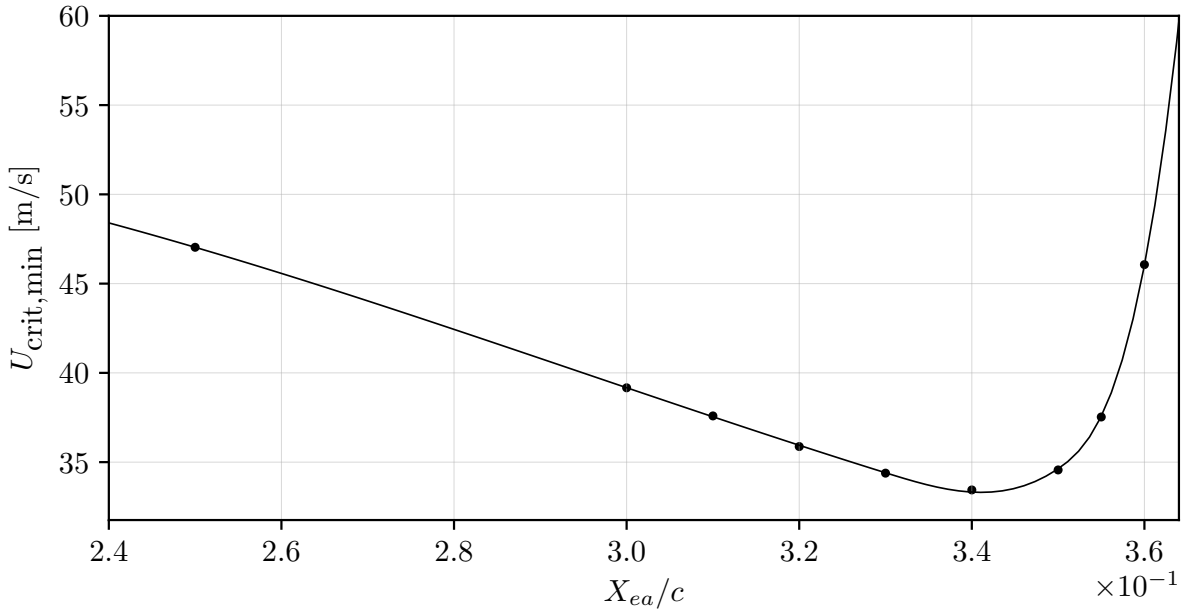


**Figure 2.13:** Evolution of the minimum flutter speed $U_{\text{crit,min}}$ as a function of the normalized location of elastic axis. Results shown for $M_t = 0.6\,\text{kg}$, $X_t = 0\,\text{m}$, $X_{cg} = 0.379\,c$, and $AR = 15$.

# Chapter 3

# Aeroelastic Testing

This chapter presents the experimental investigations conducted to characterize the aeroelastic behaviour of two wing configurations, tested respectively at IAT and the University of Liège. The main objectives of these campaigns were to observe flutter phenomena under controlled conditions and to collect data to support the calibration and validation of the numerical model developed in this work.

The chapter begins with an overview of the two wing designs and their specific features. The experimental setup is then detailed, including both excitation and measurement systems. Modal identification procedures are introduced, covering frequency-domain and time-domain techniques used to extract key dynamic parameters such as natural frequencies, damping ratios, and mode shapes. A preliminary modal analysis is conducted in wind-off conditions to evaluate the structural dynamics in the absence of aerodynamic loads. This is followed by wind tunnel tests aimed at identifying the onset of aeroelastic instabilities. Together, these investigations provide a robust experimental foundation for validating the model predictions presented in the next chapter.

## 3.1 Wing Designs

This section introduces the two wing configurations investigated during the experimental campaigns carried out at IAT and the University of Liège. These two configurations will be referred to as the IAT wing and the ULiège wing, respectively, throughout the remainder of this work.

### 3.1.1 IAT wing

As previously mentioned, the IAT wing was designed and manufactured as part of the work conducted by Prieur (2023). In the present study, the geometric and structural properties listed in Table 2.1 are retained. It should be noted that the geometric properties were measured during installation, while the structural properties are calibrated based on wind-off test results. The structure is made of 12 NACA0015 section mounted on a $H$-shaped beam. A representation of the wing section is provided in Figure 3.1.

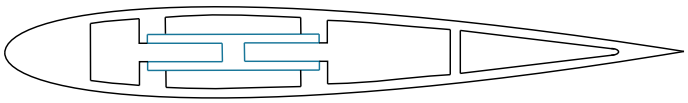

**Figure 3.1:** Schematic of the wing section assembly at IAT. The blue region highlights the internal $H$-shaped beam.

The structure is fully integrated with piezoelectric patches, which form an integral part of the wing's assembly. These patches were bonded directly onto the internal beam during manufacturing, thereby becoming embedded components of the structure. Although piezoelectric elements can operate both as

actuators and sensors, they were exclusively employed as exciters in the present work. Two types of piezoelectric patches were employed to selectively excite the bending and torsion modes of the structure.

Indeed, DuraAct piezoelectric patches and MFC patches were used. The DuraAct patches, made of isotropic piezoelectric material, were placed at mid-span, where bending-induced strains are maximum during the first bending mode. In contrast, the MFC patches, designed with an orthotropic structure, were installed near the wing root to excite torsional modes. The $45°$ fibre orientation enables effective torsional control, as it aligns with the principal strain directions induced by torsion.

This dual-patch configuration ensures optimal excitation of both bending and torsional modes. A total of $5 \times 2$ MFC patches and $8 \times 2$ DuraAct patches were used, as illustrated in Figure 3.2a. The main characteristics of both types of piezoelectric patches are summarized in Figure 3.2b.

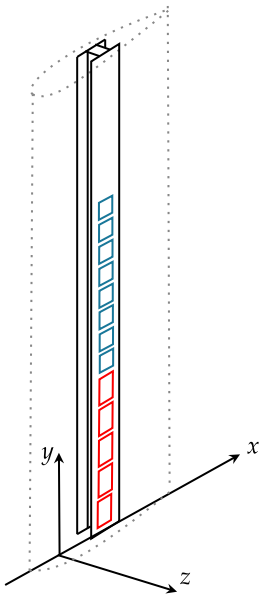


**(a)** Schematic of the piezoelectric patch layout.

| | DuraAct | MFC |
|---|---|---|
| Model | P-876.A15 | M8528-F1 |
| Capacitance ±20% [nF] | 45 | 7.4 |
| Thickness [µm] | 500 | 300 |
| Operating voltage [V] | -250 to 1000 | -500 to 1500 |

**(b)** Technical specifications of the piezoelectric patches.

**Figure 3.2:** Piezoelectric configuration. Blue patches correspond to DuraAct actuators, while red patches indicate MFC actuators.

### 3.1.2 ULiège wing

To complement the IAT configuration, a second wing was designed at the University of Liège with the objective of expanding the experimental dataset and further validating the numerical model. Its design was fully guided by the model predictions.

The wing was designed to preserve the main characteristics of the configuration tested at IAT, *i.e.*, a structure composed of 12 NACA0015 airfoil sections and an aspect ratio of $AR = 15$. Due to the smaller test section available in the wind tunnel at Liège, the half-span was reduced to $s = 1.2\,\text{m}$, which led to a chord length of $c = 0.16\,\text{m}$.

Moreover, the internal $H$-shaped structural concept used in the IAT prototype was found to be difficult to reproduce with available equipment. To address this limitation, four alternative internal beams already available in the laboratory were considered as potential internal structures. Theoretical stiffness values for each internal structure were evaluated (see section C.1), and the remaining relevant parameters were scaled relative to those of the original IAT wing. The aeroelastic model was then used to assess which internal configuration would provide the highest likelihood of exhibiting flutter, excluding any additional wingtip devices. Based on this analysis, a solid rectangular beam was selected as the most suitable internal structure for the new prototype, offering favourable dynamic characteristics for the intended flutter investigation. The beam is made of aluminium and has cross-sectional dimensions of $6 \times 15\,\text{mm}$.

A representation of the final wing section assembly is shown in Figure 3.3, and the corresponding parameters obtained from the CAD model and 3D slicer software are summarized in Table 3.1. Section height was defined to ensure a constant 3 mm gap between adjacent elements.

As previously introduced, the stiffness values were initially computed using a theoretical approach and were subsequently calibrated based on wind-off test results. All other parameters are assumed to have been measured accurately. In addition, the wing section does not include any piezoelectric patches, unlike the configuration tested at IAT. This design choice is motivated by the fact that the present campaign focuses solely on flutter observation, without any objective of implementing piezoelectric control. Moreover, the wing was not designed to incorporate any wingtip device.

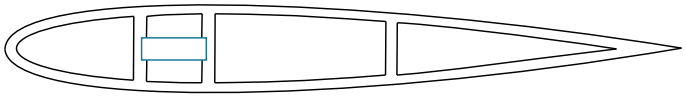

**Figure 3.3:** Schematic of the wing section assembly at ULiège. The blue region highlights the internal rectangular beam.

Table 3.1: Geometric and structural properties of the second wing configuration.

| Name | Symbol | Value | Unit |
|---|---|---|---|
| Semi span | $s$ | 1.2 | m |
| Chord | $c$ | 0.16 | m |
| Distance between the leading edge and the elastic axis | $X_{ea}$ | $c/4$ | m |
| Distance between the leading edge and the inertia axis | $X_{cg}$ | $0.41\,c$ | m |
| Mass per unit length | $m$ | 1.106 | $\mathrm{kg\,m^{-1}}$ |
| Moment of inertia (about the elastic axis) per unit length | $I_\alpha$ | $2.587 \times 10^{-3}$ | $\mathrm{kg\,m^2\,m^{-1}}$ |
| Chordwise bending stiffness | $EI_z$ | 118.12 | $\mathrm{N\,m^2}$ |
| Flapwise bending stiffness | $EI_x$ | 18.9 | $\mathrm{N\,m^2}$ |
| Torsional stiffness | $GJ$ | 21.27 | $\mathrm{N\,m^2}$ |

## 3.2 Experimental setup

This section aims to provide a detailed description of the experimental setups used for both wing configurations. The instrumentation and acquisition systems are first presented, followed by a description of the specific setups implemented for each wing. Particular attention is given to the differences in excitation methods, sensor placement, and data processing procedures.

### 3.2.1 IAT wing test setup

During this campaign, two configurations were implemented: a wind-off setup, used to characterize the structural dynamics of the wing in the IAT laboratory, and a wind tunnel setup, dedicated to the aeroelastic investigation and flutter analysis.

#### Excitation device

As previously explained in subsection 3.1.1, the wing studied in IAT was excited with piezoelectric patches. To cover the full frequency range of interest, excitation signals were generated using a NI

USB-6363 data acquisition unit system from Texas Instruments, which supplied artificial white noise to the piezoelectric actuators. This method provides broadband excitation, with energy mostly distributed across the entire spectrum, although a slight bias toward the lower frequencies is observable, as shown in Figure 3.4a.

However, it should be noted that active excitation devices are only required for wind-off testing. Once the model is installed in the wind tunnel, the ambient turbulence in the flow can act as a natural broadband excitation source, eliminating the need for dedicated actuators. In particular, the contribution of piezoelectric patches becomes increasingly negligible as the freestream velocity, and thus the level of turbulence, increases. To quantify the relative importance of the piezoelectric excitation compared to the turbulence-induced response, the signal-to-noise ratio (SNR) is introduced. It is defined as

$$\mathrm{SNR} = \frac{P_{\mathrm{signal}}}{P_{\mathrm{noise}}} = \frac{P_{\mathrm{signal}}}{P_{\mathrm{total}} - P_{\mathrm{signal}}}, \quad \text{with} \quad P = \int_{f_1}^{f_2} \mathrm{PSD}(f)\,\mathrm{d}f, \tag{3.1}$$

where $P_{\mathrm{signal}}$ is the signal power estimated from the wind-off measurement, and $f_1$ and $f_2$ denote the lower and upper bounds of the frequency band considered for the analysis. Its evolution is presented in Figure 3.4b. As expected, the ratio decreases rapidly with increasing freestream velocity, as the excitation provided by the piezoelectric patches becomes rapidly negligible.

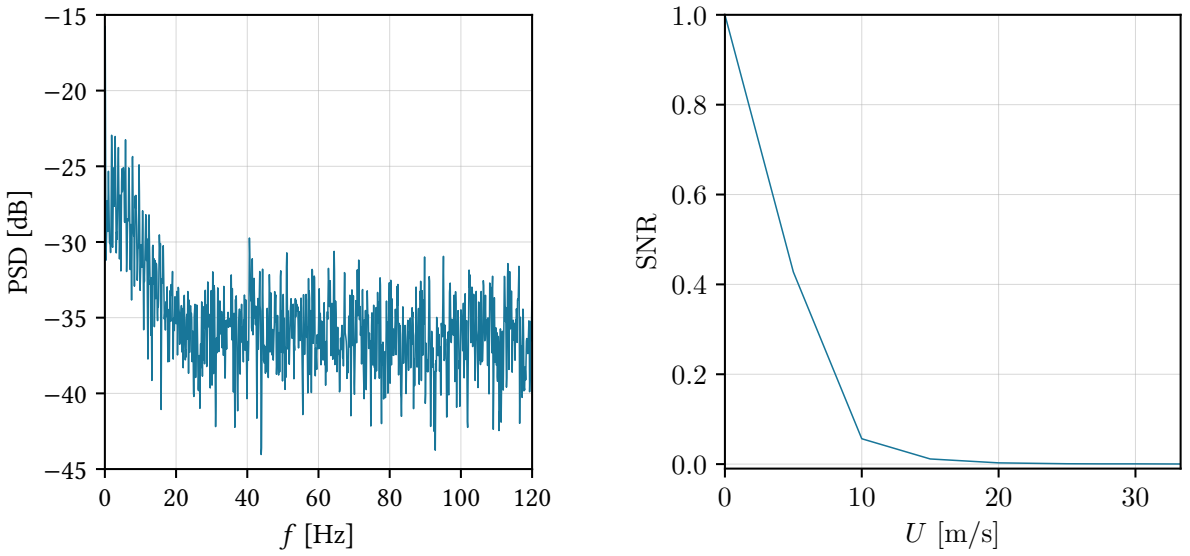


**(a)** PSD of the generated white noise excitation signal.

**(b)** SNR as a function of freestream airspeed $U$.

**Figure 3.4:** Analysis of the white noise excitation and its degradation under wind conditions.

### Sensors

During the wind-off characterisation, the structural response is measured using 6 piezoelectric accelerometers attached to the wing. These accelerometers are positioned to capture both bending and torsional deformations, ensuring they are not located at vibration nodes. Beeswax is used to fix the sensors onto the structure, allowing for easy removal after testing. In addition, an aluminium duct tape is applied over each accelerometer to prevent accidental detachment during measurements and to protect the devices from potential damage.

In the wind tunnel, the decision was made to use only 2 accelerometers, both positioned in the wing tip configuration. This adjustment was motivated by the fact that the sensors were not securely fixed enough to withstand higher airspeeds, and their wiring is embedded inside the wing.

Unlike the accelerometers, which were calibrated according to their respective data-sheets, the lasers required manual calibration. To achieve this, a dedicated setup was made, consisting of a fixed reference

structure and a movable platform to which the lasers were mounted. The distance between the two was incrementally varied and measured, while the corresponding voltage output from each laser was recorded throughout the process. A linear fit was then applied to the voltage–displacement data, and the slope of the resulting line was used as the calibration factor. The results of this procedure is presented in Figure 3.5a and the specifications of the laser displacement sensors are summarized in Figure 3.5b.

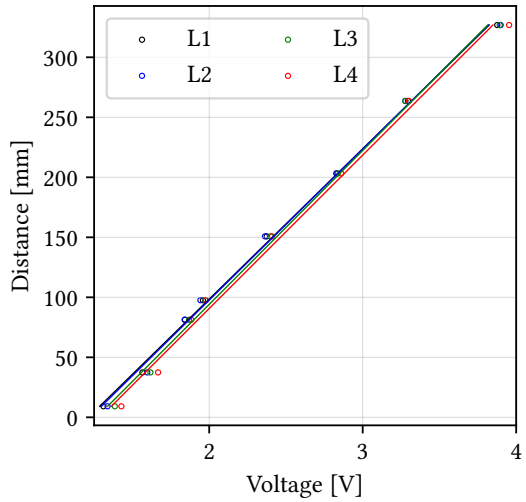


**(a)** Calibration curves for the four laser displacement sensors, illustrating the linear voltage–displacement relationship.

| | |
|---|---|
| Model | ILD 1420-500 |
| Measurement range [mm] | 500 |
| Calibration coeff. [mm/V] | 125.18 - 128.27 |
| Technology | Laser triangulation |

**(b)** Technical specifications of the optoNCDT laser displacement sensors.

**Figure 3.5:** Laser characteristics. Calibration coefficient given by curve slope.

Displacements are measured using two pairs of laser displacement sensors, with each pair composed of two sensors positioned on opposite sides of the wing section. A schematic representation of the measurement configuration is shown in Figure 3.6, for both $\alpha = 0°$ and $\alpha \neq 0°$. This sensor arrangement allows the bending and torsional components of the motion to be decoupled and evaluated independently.

The sensors are spaced by a total distance of $d_1 + d_2$ and respectively measure the vertical distances $z_1$ and $z_2$, expressed as

$$\begin{aligned} z_1 &= z_1^0 + \Delta z_1, \\ z_2 &= z_2^0 + \Delta z_2, \end{aligned} \tag{3.2}$$

where $z_1^0$ and $z_2^0$ are the initial reference positions (measured at rest), and $\Delta z_1$ and $\Delta z_2$ represent the displacements induced by the wing's motion about the elastic axis $X_{ea}$. The pure torsional rotation $\alpha$ is derived from the differential displacement between the two sensors, given as

$$\alpha = \arctan\left(\frac{\Delta z_2 - \Delta z_1}{d_1 + d_2}\right). \tag{3.3}$$

To isolate the pure bending displacement $w$, the measured displacements are corrected for torsional contributions:

$$w_1 = \Delta z_1 - d_1 \tan\alpha, \qquad w_2 = \Delta z_2 + d_2 \tan\alpha. \tag{3.4}$$

The net bending displacement is then computed as the average of the corrected values:

$$w = \frac{w_1 + w_2}{2} = \frac{1}{2}\left(\Delta z_1 + \Delta z_2 + (d_2 - d_1)\tan\alpha\right). \tag{3.5}$$

Additionally, a 6-DOFs ATI balance was used to measure the forces and moments along all translational and rotational axes. The balance, mounted at the wing root, exhibits a high stiffness that, while not infinite,

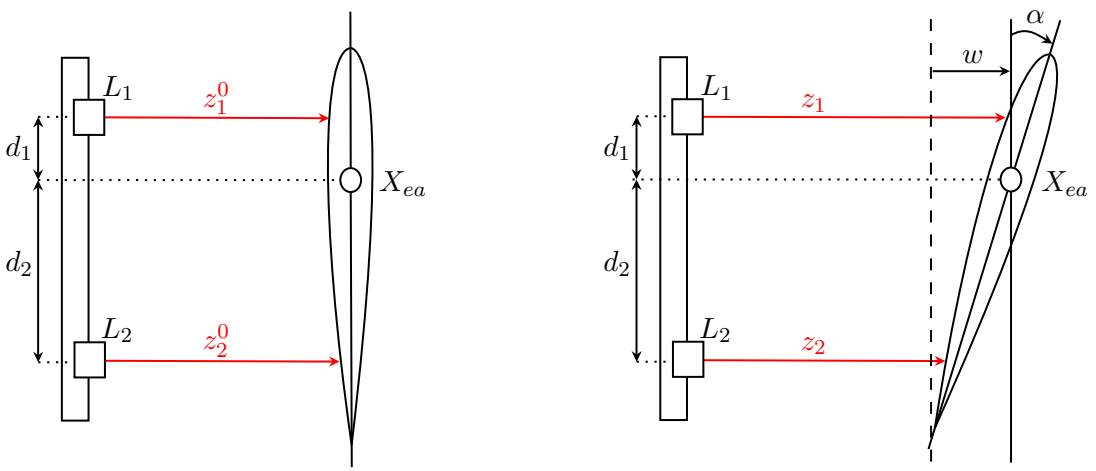


**(a)** $\alpha = 0°$. **(b)** $\alpha \neq 0°$.

**Figure 3.6:** Computation of the bending displacement $w$ and torsion angle $\alpha$ using a set of two laser sensors, denoted by $L_1$ and $L_2$.

is sufficient to approximate the boundary conditions of an ideal clamped configuration as assumed in the theoretical model. An illustration of the clamping assembly and balance integration is shown in Figure 3.7. Finally, a Pitot tube was added to the setup. The Pitot tube provides a voltage signal that is calibrated using a linear model to obtain the dynamic pressure. This value is directly used to normalize forces and moments, allowing computation of aerodynamic coefficients without requiring direct velocity measurements. The dynamic pressure is calculated as

$$p_{\text{dyn}} = V\, C_{p_{\text{dyn}}} - p_{\text{dyn},0}, \tag{3.6}$$

where $V$ is the measured voltage, $C_{p_{\text{dyn}}}$ is the calibration factor, and $p_{\text{dyn},0}$ is an offset obtained during calibration.

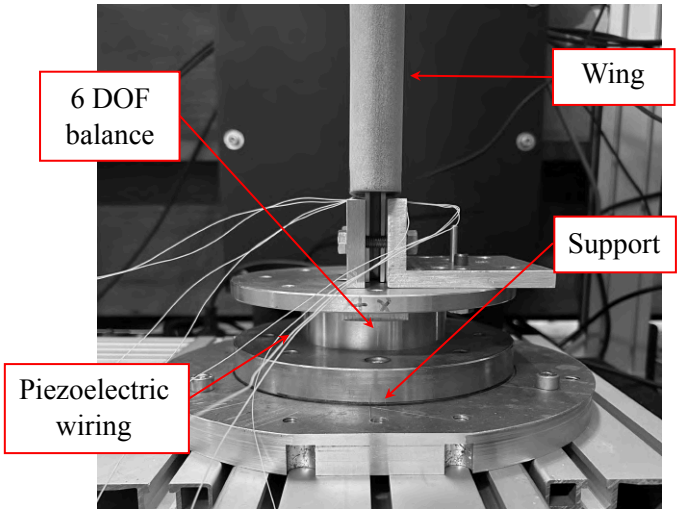


**Figure 3.7:** View of the experimental setup at the wing root.

### Data processing

Data acquisition and signal processing were performed using the DEWE-43A acquisition system in conjunction with DewesoftX software. The acquisition unit is shown in Figure 3.8. This equipment enables the synchronous measurement of up to eight channels, ensuring time-aligned data collection across all sensors. The sampling rate is a parameter that is required for discretizing the continuous signal. For this

experiment, a maximum frequency of 150 Hz is considered. However, to avoid aliasing, Shannon's sampling theorem must be satisfied, which recommends a sampling rate of 2.56 times the highest frequency in the signal. For coherence with the solver's time step, frequencies up to 195 Hz are evaluated, resulting in a total sampling rate of 500 Hz that was measured.

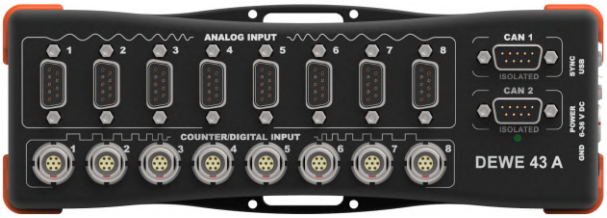


**Figure 3.8:** DEWE-43A acquisition system.

Then, the lines parameter was specified, it describes the number of frequency points in a spectrum, defining the frequency resolution for FFT computation. In this analysis, the parameter was set to 2500 to achieve a sufficiently fine discretization for post treatment. This parameter is a compromise between the frequency resolution and the total acquisition time. To improve the reliability of the measurements, an average over 10 repeated acquisitions was performed. This averaging process helps to reduce the influence of random noise and ensures more consistent results. In addition, windowing techniques were applied to both the excitation and the response signals to reduce the effect of spectral leakage. Spectral leakage occurs when signals are not perfectly periodic within the time interval over which they are measured. This is especially problematic for random signals, which contain a wide range of frequencies and naturally exhibit abrupt beginnings and endings in a finite time record. These abrupt transitions introduce artificial frequency components into the spectrum, distorting the true response of the system. To address this, a Hanning window was applied. This window gradually reduces the amplitude of the signal to zero at both ends of the time record, smoothing the transitions and thereby minimizing the unwanted spectral leakage. The Hanning window is particularly well-suited for random data, as it offers a good balance between frequency resolution and amplitude accuracy. Compared to other window types, it introduces only moderate distortion and is widely used in modal testing for this reason. Applying the window ensures that the signal decays appropriately within the selected observation period $T$ , which further improves the quality of the frequency-domain representation. Indeed, the Fourier Transform assumes periodicity over the analysis window. When this assumption is not retrieved, as it would be the case with truncated random signals, leakage becomes significant. The effect of windowing on the signal is shown in Figure 3.9.

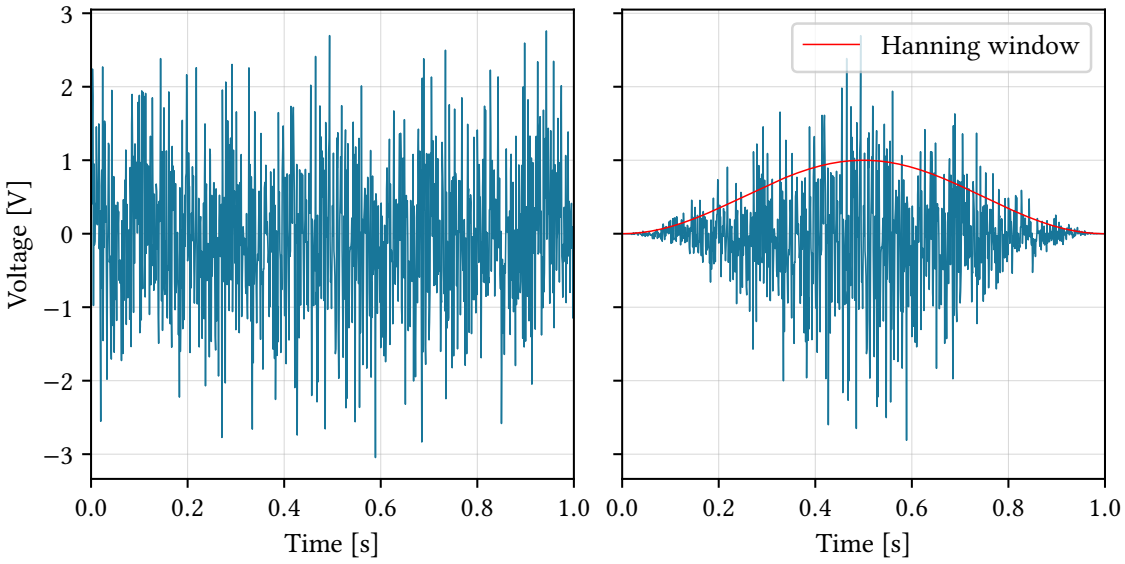


**Figure 3.9:** Representation of Hanning windows and its impact on a truncated white noise signal.

### Wind-off configuration

The locations of the accelerometers and laser displacement sensors are shown in Figure 3.10, where blue and red annotations respectively indicate their positions along the wing span. Moreover, a picture of the instrumented setup is provided for reference. The wing was mounted on the force balance during sensor installation to account for the finite stiffness of the clamping system in the measurement configuration.

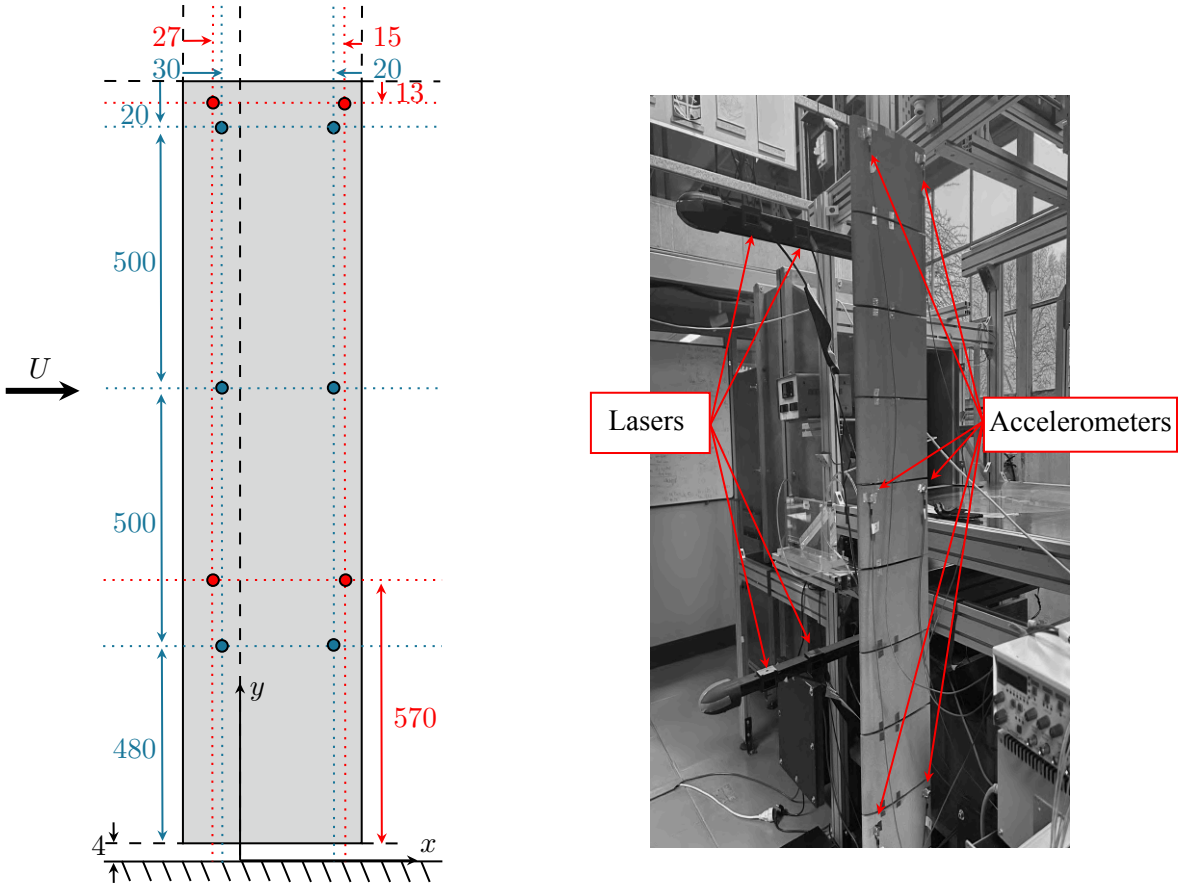


**(a)** Diagram showing sensor locations. **(b)** Picture of the experimental setup.

**Figure 3.10:** Experimental setup and sensor locations : **(a)** Schematic representation of the wing showing sensor locations. Red dots indicate the positions of laser displacement sensors, while blue dots correspond to accelerometers. Dimensions are in mm. **(b)** Picture of the experimental setup in the Iat laboratory with the sensors visibly mounted on the structure.

### Wind tunnel configuration

The IAT S4 facility in which the test was conducted is presented in Appendix A. As shown in Figure 2.7, the reference configuration is not predicted to exhibit flutter within the low-speed range. To address this, a wingtip modification was introduced to add mass and/or inertia at the tip, thereby altering the system's frequency content and influencing the evolution of its aeroelastic characteristics. Two wingtip configurations were initially tested, as illustrated in Figure 3.11. These two configurations are referred to as the *Ogive* and *Saumon* configurations throughout the remainder of this work.

In this representation, the red area indicates the allowable region for placing additional masses. A dedicated set of cylindrical weights, each with a mass of approximately 50 g, was manufactured to fit precisely within this designated volume. The same figure also shows the positions of the laser sensors, the force balance, and the accelerometers located in the different wingtip configurations.

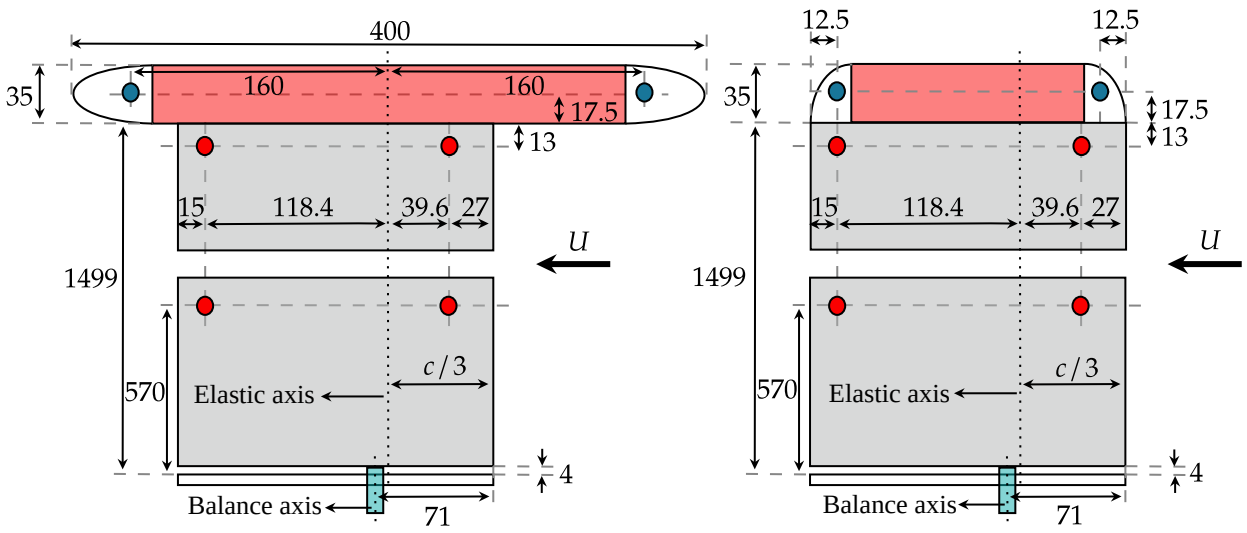


**Figure 3.11:** Comparison of two wingtip designs: *Ogive* wingtip (left) and *Saumon* wingtip (right). Both configurations are shown with reference axes for balance and elasticity. Lasers are denoted by red dots, while accelerometers are represented by blue dots. Dimensions in mm.

### 3.2.2 ULiège wing test setup

Only a single setup was implemented during this campaign. The wing was directly mounted in the wind tunnel, and wind-off measurements were performed at the beginning of each test sequence. The facility in which the test was conducted is presented in Appendix B. During this campaign, the wing was mounted on the top part of the wing section. This configuration allows gravity to act in the same direction as the first bending deformation and act as a gravity-assisted damping.

#### Excitation device

As previously explained, this setup does not include any piezoelectric actuators and is therefore primarily excited by freestream turbulence. In addition, a rope was attached to the internal beam through the gap between sections to allow manual excitation and generate free-decay responses. This configuration also makes it possible to introduce additional damping near critical conditions in order to limit the amplitude of oscillations near critical conditions.

#### Sensors

The dynamic response of the wing was directly measured using a wireless accelerometer developed by Microsys, a research laboratory at the University of Liège specializing in ultra-low-power microsystems and miniaturized electronic circuits. The accelerometer was attached with double-sided tape at the trailing edge of the wingtip during testing, and the recorded data were stored on a local network. A script was developed to automatically download the most recently recorded file from the local network and perform the modal identification procedure in real time during testing. The wireless accelerometer is characterized by a sampling frequency of 201.03 Hz.

While this wireless technology eliminates the need for cable management, it introduces potential reliability issues related to data transmission. In particular, data recording is susceptible to packet loss, which may occur due to network congestion, hardware limitations, software errors, or other environmental and systemic factors affecting the integrity of data transfer. To address these concerns, data quality is systematically evaluated during the post-processing phase.

## 3.3 Modal Identification Process

This section presents the modal identification procedures used in this study, along with the theoretical background supporting each method. Two approaches were retained: the PolyMAX and the Stochastic Subspace Identification method (SSI).

The SSI method was specifically implemented due to the limitations associated with traditional frequency-domain techniques such as PolyMAX, which require explicit knowledge of the excitation forces. In the present context, the input forces are not actively controlled but result from natural excitations and are not directly measurable. Although frequency-domain methods like PolyMAX can still yield reasonable results under high signal-to-noise ratio conditions, this criterion is not satisfied here due to the limited effectiveness of the piezoelectric actuators and the predominance of ambient disturbances, as illustrated in Figure 3.4b.

As a result, the PolyMAX technique was applied exclusively to the wind-off configuration, where controlled excitation could be ensured. In contrast, the SSI method was employed for wind tunnel measurements, where excitation forces are not controlled.

### 3.3.1 Polyreference least-squares complex frequency-domain method

In this section, the polyreference least-squares complex frequency-domain method, also known as the PolyMAX method, is implemented. This method aims to identify and evaluate the modal properties in the frequency range of interest. It was developed to address several challenges encountered in experimental modal analysis, including the identification of high-order or highly damped systems, and the need for reliable results with minimal user interaction (Peeters et al. 2004). A particular strength of this method lies in the generation of clear stabilization diagrams, which facilitate the selection between physical and spurious poles.

PolyMAX is a frequency-domain method based on a right matrix-fraction representation of the FRF, rather than the partial fraction form. It is a polyreference extension of the least-squares complex frequency-domain (LSCF) method and can handle SIMO/MIMO data. Among its main benefits is the possibility to avoid the singular value decomposition step traditionally required to reduce the rank of the residues. In addition, closely spaced modes can be separated more reliably, improving both accuracy and robustness of the estimation process (Peeters et al. 2004). The method needs FRFs as primary data such that

$$\mathbf{H}(f) = \begin{bmatrix} H_{1,1}(f) & \dots & H_{1,n_i}(f) \\ \vdots & \ddots & \vdots \\ H_{n_o,1}(f) & \dots & H_{n_o,n_i}(f) \end{bmatrix}, \tag{3.7}$$

where $\mathbf{H}(f) \in \mathbb{C}^{n_o \times n_i}$ denotes the FRF matrix, which contains all the FRFs between the $n_i$ input and $n_o$ output channels. In the context of the present measurement setup, the system consists of a single input and six output channels. The FRF matrix can be expressed in the right-fraction model as

$$\mathbf{H}(f) = \mathbf{B}(f)\, \mathbf{A}(f)^{-1}, \tag{3.8}$$

where each rows of the matrix is written as

$$H_r(f) = B_r(f)\, \mathbf{A}(f)^{-1}, \qquad \forall r \in 1, 2, \dots, n_o \tag{3.9}$$

with $B_r(f) \in \mathbb{C}^{1 \times n_i}$ and $\mathbf{A}(f) \in \mathbb{C}^{n_i \times n_i}$. Both expression can be expressed as polynomial in $f$ given by

$$\mathbf{A}(f) = \sum_{k=0}^{p} \Omega_k(f) \boldsymbol{\alpha}_r \qquad B_r(f) = \sum_{k=0}^{p} \Omega_k(f) \beta_{rk}, \tag{3.10}$$

where $\Omega_k(f) = \exp(i\, p\, f\, \Delta t)$ are the basis function, $p$ is the polynomial order of the model, $p$ is the

polynomial order of the model, and the coefficients $\boldsymbol{\alpha}_r$ and $\beta_{rk}$ are the model unknowns to be identified. The method is designed to determine the optimal coefficient that minimizes the error between the model and the measured data. These coefficients are assembled into a single parameter vector

$$\theta = \begin{pmatrix} \beta_1 \\ \vdots \\ \beta_{n_o} \\ \hline \boldsymbol{\alpha} \end{pmatrix} \in \mathbb{R}^{(n_i+n_o)(p+1)\times n_i}. \tag{3.11}$$

The objective is to find all unknown model coefficients based on measurements. To achieve this, the coefficients $\boldsymbol{\theta}$ can be identified by minimizing the non-linear least-squares error function

$$\varepsilon_{NLS}(f, \boldsymbol{\theta}) = \omega_r(f) \left( B_r(f, \beta_r)\mathbf{A}^{-1}(f, \boldsymbol{\alpha}) - \hat{H}_r(f) \right), \tag{3.12}$$

where $\omega_r(f)$ is an arbitrary weighting function, which can be set to unity, and $\hat{(.)}$ refers to measured quantity. A cost function can be evaluated and minimized based on these error functions. However, it is evident that this process results in non-linear equations. To approximate this non-linear least-squares problem, a sub-optimal linear least-squares approach can be employed by right-multiplying Equation 3.12 with the numerator matrix polynomial $\mathbf{A}$. The error function for each line can be expressed in matrix form as

$$\mathbf{E}_r^{LS}(\boldsymbol{\theta}) = \begin{pmatrix} \varepsilon_r^{LS}(f_1, \boldsymbol{\theta}) \\ \varepsilon_r^{LS}(f_2, \boldsymbol{\theta}) \\ \vdots \\ \varepsilon_r^{LS}(f_{N_f}, \boldsymbol{\theta}) \end{pmatrix} = (\mathbf{X}_r \ \mathbf{Y}_r) \begin{pmatrix} \beta_r \\ \boldsymbol{\alpha} \end{pmatrix}, \tag{3.13}$$

where $\mathbf{X}_r \in \mathbb{C}^{N_f\times(p+1)}$, $\mathbf{Y}_r \in \mathbb{C}^{N_f\times n_i(p+1)}$ and $N_f$ refers to the number of element in the frequency content of the measured signal. Matrices $\mathbf{X}_r$ and $\mathbf{Y}_r$ are respectively defined as

$$\mathbf{X}_r = \begin{pmatrix} \omega_r(f_1) \left(\Omega_0(f_1) \dots \Omega_p(f_1)\right) \\ \vdots \\ \omega_r(f_{N_f}) \left(\Omega_0(f_{N_f}) \dots \Omega_p(f_{N_f})\right) \end{pmatrix}, \quad \mathbf{Y}_r = \begin{pmatrix} -\omega_r(f_1) \left(\Omega_0(f_1) \dots \Omega_p(f_1)\right) \otimes \hat{H}_r(f_1) \\ \vdots \\ -\omega_r(f_{N_f}) \left(\Omega_0(f_{N_f}) \dots \Omega_p(f_{N_f})\right) \otimes \hat{H}_r(f_{N_f}). \end{pmatrix} \tag{3.14}$$

Based on this error matrix, one can minimize the cost function

$$l^{NS}(\boldsymbol{\theta}) = \sum_{r=1}^{n_o} \text{trace} \left( \mathbf{E}_r^{LS}(\boldsymbol{\theta})^H \mathbf{E}_r^{LS}(\boldsymbol{\theta}) \right), \tag{3.15}$$

with $(.)^H$ the hermitian operator. To minimize this expression, one can derive it with respect to each unknowns. Without delving into details, the expression $\partial\varepsilon^{LS}(\boldsymbol{\theta})/\partial\beta_r$ is equal to zero when the condition $\beta_r = -\mathbf{R}_r^{-1}\mathbf{S}_r\boldsymbol{\alpha}$ is satisfied. To extract the poles and build the stabilisation diagram, only the $\boldsymbol{\alpha}$ must be computed. One can eliminate $\beta_r$ from $\partial\varepsilon^{LS}(\boldsymbol{\theta})/\partial\boldsymbol{\alpha}$ by introducing this condition, one get

$$\left( 2\sum_{r=1}^{n_o} \left( \mathbf{T}_r - \mathbf{S}_r^T\mathbf{R}_r^{-1}\mathbf{S}_r \right) \right) \boldsymbol{\alpha} = \mathbf{M}\boldsymbol{\alpha} = 0, \tag{3.16}$$

where $\mathbf{M} \in \mathbb{C}^{n_i(p+1)\times n_i(p+1)}$. Each matrix appearing in $\mathbf{M}$ definition are respectively defined as

$$\mathbf{R}_r = \mathfrak{Re}\{\mathbf{X}_r^H\mathbf{X}_r\} \quad \mathbf{S}_r = \mathfrak{Re}\{\mathbf{X}_r^H\mathbf{Y}_r\} \quad \mathbf{T}_r = \mathfrak{Re}\{\mathbf{Y}_r^H\mathbf{Y}_r\}. \tag{3.17}$$

Further explanation of the method and development can be found in the work of Peeters et al. (2004). Expression from Equation 3.16 can be solved for the denominator polynomial $\boldsymbol{\alpha}$ using a least-squares approach. To prevent a trivial solution, a constraint is imposed on the parameters by setting $\boldsymbol{\alpha}_p = \mathbf{I}_{m\times m}$.

This constraint additionally resolves parameter redundancy within the right matrix-fraction model, as multiplying both the numerator and denominator by the same matrix alters the individual polynomials but retains the same transfer function matrix (Peeters et al. 2004). After some development, the system can be solved as

$$\begin{pmatrix} M_{1,1} & M_{1,2} & \dots & M_{1,n_i\,p} \\ M_{2,1} & M_{2,2} & \dots & M_{2,n_i\,p} \\ \vdots & \vdots & \ddots & \vdots \\ M_{n_i\,p,1} & M_{n_i\,p,2} & \dots & M_{n_i\,p,n_i\,p} \end{pmatrix} \begin{pmatrix} \boldsymbol{\alpha}_0 \\ \boldsymbol{\alpha}_1 \\ \vdots \\ \boldsymbol{\alpha}_{p-1} \end{pmatrix} = - \begin{pmatrix} M_{1,n_i\,p+1} & \dots & M_{1,n_i(p+1)} \\ M_{2,n_i\,p+1} & \dots & M_{2,n_i(p+1)} \\ \vdots & & \vdots \\ M_{n_i\,p,n_i\,p+1} & \dots & M_{n_i\,p,n_i(p+1)} \end{pmatrix}. \tag{3.18}$$

Once the $\boldsymbol{\alpha}$ value are determined, one can evaluate the companion matrix given by

$$\mathbf{C} = \begin{pmatrix} 0 & \mathbf{I} & \dots & 0 & 0 \\ 0 & 0 & \ddots & \vdots & \vdots \\ \vdots & \vdots & & \mathbf{I} & 0 \\ 0 & 0 & \dots & 0 & \mathbf{I} \\ -\boldsymbol{\alpha}_0^T & -\boldsymbol{\alpha}_1^T & \dots & -\boldsymbol{\alpha}_{p-2}^T & -\boldsymbol{\alpha}_{p-1}^T \end{pmatrix}. \tag{3.19}$$

Based on this matrix, the eigenvectors of $\mathbf{C}$ give the complex mode shapes of the aircraft structure and the corresponding eigenvalue $a_i$ are computed and related to the system poles $\lambda_i$ by

$$a_i = e^{\lambda_i \Delta t}. \tag{3.20}$$

Finally, one can determine the natural frequencies and the corresponding damping ratio as

$$f_i = \frac{|\lambda_i|}{2\pi}\ [\text{Hz}] \qquad \zeta_i = -\frac{\mathfrak{Re}\{\lambda_i\}}{f_i}\ [\text{-}]. \tag{3.21}$$

### 3.3.2 Stochastic subspace identification method

The SSI method presents a key advantage in that it operates directly on time-domain output signals and does not require prior knowledge of the system input, provided the excitation can be modelled as a stochastic process, typically white noise. In addition, the method is well suited for free-response conditions, making it particularly relevant for the present experimental context. Among the various SSI formulations available in the literature, this study employs the covariance-driven stochastic subspace identification approach, which is widely recognized for its simplicity of implementation and relatively low computational cost. The method is based on the following continuous-time state-space model

$$\begin{cases} \dot{r} &= \mathbf{A}_c r + \mathbf{B}_c f, \\ y &= \mathbf{C} r, \end{cases} \tag{3.22}$$

where $\mathbf{A}_c$ is the continuous-time state matrix, $\mathbf{B}_c$ is the input matrix, $\mathbf{C}$ is the output matrix, $r(t)$ is the state vector, $f(t)$ is the excitation (assumed stochastic), and $y(t)$ is the measured output vector. The solution to the state equation is expressed as

$$r(t) = e^{\mathbf{A}_c(t-t_0)}\, r(t_0) + \int_{t_0}^{t} e^{\mathbf{A}_c(t-\tau)}\, \mathbf{B}_c\, f(\tau)\, \mathrm{d}\tau, \tag{3.23}$$

where the first term represents the free response and the second term corresponds to the particular solution due to external excitation. Assuming measurements are sampled at discrete time intervals $\Delta t$, the system

can be discretized as follows

$$\begin{aligned} r\left((k+1)\Delta t\right) &= e^{\mathbf{A}_c \Delta t} r\left(k\Delta t\right) + \int_{k\Delta t}^{(k+1)\Delta t} e^{\mathbf{A}_c((k+1)\Delta t - \tau)}\, \mathbf{B}_c\, f(\tau)\, \mathrm{d}\tau, \\ \Rightarrow \quad r\left[k+1\right] &= e^{\mathbf{A}_c \Delta t} r\left[k\right] + w\left[k\right] = \mathbf{A} r\left[k\right] + w\left[k\right]. \end{aligned} \tag{3.24}$$

where $\mathbf{A} = \exp\left(\mathbf{A}_c \Delta t\right)$ is the discrete-time state matrix and $w[k]$ is the discrete process noise introduced by the stochastic excitation. The corresponding discrete-time output equation is

$$y[k] = \mathbf{C} r[k] + v[k], \tag{3.25}$$

where $v[k]$ is the measurement noise. Both the process and measurement noises are assumed to be zero-mean white Gaussian noise with covariance matrices

$$E[w[k]] = E[v[k]] = 0 \quad \text{and} \quad E\left[\begin{pmatrix} w[k] \\ v[k] \end{pmatrix} \begin{pmatrix} w[l]^T & v[l]^T \end{pmatrix}\right] = \begin{pmatrix} \mathbf{Q} & \mathbf{S} \\ \mathbf{S} & \mathbf{R} \end{pmatrix} \delta_{kl}, \tag{3.26}$$

where $E[.]$ denotes the expectation operator and $\delta_{kl}$ is the Kronecker delta. Additionally, the stochastic process is assumed to be stationary with zero mean, which implies that the state covariance matrix is time-invariant

$$E[r[k] r[k]^T] = \Sigma, \tag{3.27}$$

where $\Sigma$ is independent of the time $k$. Moreover, the process and measurement noises are considered to be uncorrelated with the system state, meaning

$$E[r[k] w[k]^T] = 0 \quad \text{and} \quad E[r[k] v[k]^T] = 0. \tag{3.28}$$

The SSI method relies on evaluating the output covariance matrices, which characterize the correlations between output signals at different time lags. These are defined as

$$\Lambda_i \triangleq E\left[y(k+1)\, y(k)^T\right], \tag{3.29}$$

where $\Lambda_i \in \mathbb{R}^{n_o \times n_o}$. These matrices capture the temporal correlations in the output signal and serve as the core input to the subspace identification algorithm. Moreover, the next state-output covariance matrix $G$ are defined as

$$G \triangleq E[r[k+1]\, y[k]^T], \tag{3.30}$$

where $\Lambda_i \in \mathbb{R}^{2n_o \times n_o}$. From these definitions, the following properties can be established

$$\begin{aligned} \Sigma &= \mathbf{A}\Sigma\mathbf{A}^T + \mathbf{Q}, \\ \Lambda_0 &= \mathbf{C}\Sigma\mathbf{C}^T + \mathbf{R}, \\ \mathbf{G} &= \mathbf{A}\Sigma\mathbf{C}^T + \mathbf{S}, \\ \Lambda_i &= \mathbf{C}\mathbf{A}^{i-1}\mathbf{G}. \end{aligned} \tag{3.31}$$

This last result, demonstrated by Golinval (n.d.), represents one of the most important properties used to address the identification problem. It implies that the output covariance matrices can be interpreted as the impulse responses of an equivalent deterministic linear time-invariant system (Peeters & Roeck 1999). Based on this interpretation, one can successively write

$$\begin{cases} \Lambda_1 &= \mathbf{C}\,\mathbf{G}, \\ \Lambda_2 &= \mathbf{C}\,\mathbf{A}^1\,\mathbf{G}, \\ & \vdots \\ \Lambda_p &= \mathbf{C}\,\mathbf{A}^{p-1}\,\mathbf{G}, \end{cases} \quad \Rightarrow \quad \begin{bmatrix} \Lambda_1 \\ \Lambda_2 \\ \vdots \\ \Lambda_p \end{bmatrix} = \mathcal{O}_p \mathbf{G}, \tag{3.32}$$

where $\mathcal{O}_p = \left[\mathbf{C}\ \mathbf{CA} \dots \mathbf{CA}^{p-1}\right]^T$ is the $p^{\text{th}}$ order observability matrix. Similarly, one can write

$$\begin{bmatrix}\Lambda_1 & \Lambda_2 & \dots & \Lambda_q\end{bmatrix} = \mathbf{C}\,\mathcal{C}_q, \tag{3.33}$$

where $\mathcal{C}_q = \left[\mathbf{G}\ \mathbf{AG} \dots \mathbf{A}^{q-1}\mathbf{G}\right]$ is the $q^{\text{th}}$ order controllability matrix. By combining both matrices, the block-Hankel matrix $\mathcal{H}_{p,q}$ can be expressed as the product

$$\mathcal{H}_{p,q} = \mathcal{O}_p\mathcal{C}_q = \begin{bmatrix} \mathbf{CG} & \mathbf{CAG} & \dots & \mathbf{CA}^{q-1}\mathbf{G} \\ \mathbf{CAG} & \mathbf{CA}^2\mathbf{G} & \dots & \mathbf{CA}^{q}\mathbf{G} \\ \vdots & \vdots & \ddots & \vdots \\ \mathbf{CA}^{p-1}\mathbf{G} & \mathbf{CA}^{p}\mathbf{G} & \dots & \mathbf{CA}^{p+q-2}\mathbf{G} \end{bmatrix} = \begin{bmatrix} \Lambda_1 & \Lambda_2 & \dots & \Lambda_q \\ \Lambda_2 & \Lambda_3 & \dots & \Lambda_{q+1} \\ \vdots & \vdots & \ddots & \vdots \\ \Lambda_p & \Lambda_{p+1} & \dots & \Lambda_{p+q-1} \end{bmatrix}, \tag{3.34}$$

where the last equality was derived using the last properties presented in Equation 3.31. Since the true system order is theoretically infinite, the exact output covariance matrices are not known. Instead, they are approximated from the available time-series data using

$$\hat{\Lambda}_i = \frac{1}{N-i}\sum_{k=0}^{N-i-1}\left(y\left[k+i\right]\ y\left[k\right]^T\right) \quad \forall i \in [1, p+q-1], \tag{3.35}$$

where $N$ is the number of samples. From the estimated block-Hankel matrix, the observability and controllability matrices can be recovered via singular value decomposition :

$$\begin{aligned} \mathcal{O}_p &= U_1\, S_1^{1/2}, \\ \mathcal{C}_q &= S_1^{1/2}\, V_1^T, \end{aligned} \tag{3.36}$$

with $\mathcal{H}_{p,q} = U_1 S_1 V_1^T$. The output matrix $\mathbf{C}$ is directly extracted from the first $n_o$ rows of $\mathcal{O}_p$. The state matrix $\mathbf{A}$ is then computed using the shift-invariance property of the observability matrix. By introducing the upper-shifted matrix $\mathcal{O}_p^{\uparrow}$, defined as

$$\mathcal{O}_p^{\uparrow} = \begin{bmatrix} \mathbf{C\,A} \\ \mathbf{C\,A}^2 \\ \vdots \\ \mathbf{C\,A}^{p-1} \end{bmatrix} = \mathcal{O}_{p-1}\,\mathbf{A}. \tag{3.37}$$

Both matrices $\mathcal{O}_p^{\uparrow}$ and $\mathcal{O}_{p-1}$ being determined by making use of the $\mathcal{O}_p$ matrix, the state matrix can be identified by solving a least-squares problem. Finally, the eigenvectors of matrix $\mathbf{A}$ corresponds to the complex mode shapes of the structure and the eigenvalues $a_i$ are related to the system poles $\lambda_i$ by

$$a_i = e^{\lambda_i \Delta t}. \tag{3.38}$$

The frequencies and damping ratios are extracted using the same procedure described in Equation 3.21.

### 3.3.3 Stabilization diagram

In modal analysis applications, it is generally recommended to over-specify the model order, *i.e.* to fit high-order models that include significantly more modes than present in the data, to estimate the modal parameters from real measurements. This approach requires post-processing of the data to distinguish true physical modes from spurious ones. This distinction is achieved by analysing the stabilization diagram. The poles associated with a given model order are compared to those of a model with one order lower complexity. To identify stabilized modes corresponding to physical modes, tolerance criteria for the relative error must be defined.

## 3.4 IAT wing

### 3.4.1 Wind-off identification

During this campaign, a complete wind-off identification procedure was conducted to determine all the modal properties of the structure, *i.e.* natural frequencies, damping ratios, and mode shapes. While comparing natural frequencies provides a first validation step, the accurate prediction of mode shapes is of greater importance. To this end, the Modal Assurance Criterion is used to quantitatively assess the agreement between the experimental and numerical mode shapes.

Figure 3.12 shows a typical system response measured using one accelerometer. Both the Frequency response function (FRF) and the coherence function are presented. Drops in the coherence function can be observed, corresponding to anti-resonances where the amplitude becomes minimal and noise dominates the measurement. Additionally, the signal is affected by low-frequency disturbances, which can be attributed to the amplification of noise by the excitation signal, as illustrated in Figure 3.4a. Four distinct peaks can be observed below 60 Hz, along with a potential additional peak at low frequency. However, this latter peak lies in a particularly noisy region of the spectrum, making its identification less reliable.

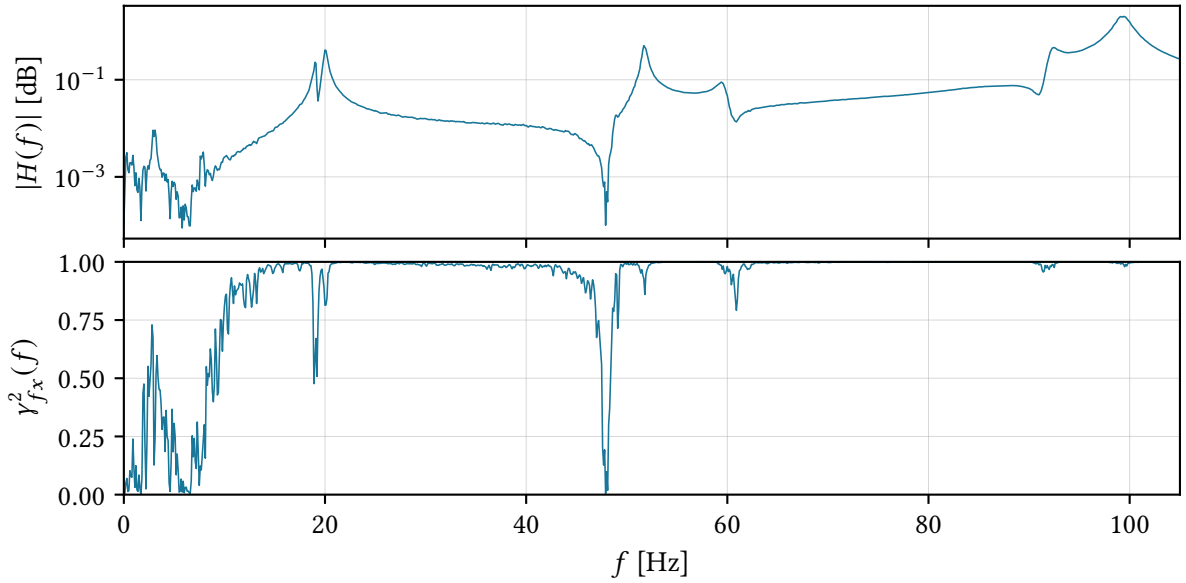


**Figure 3.12:** Frequency response function and coherence function recorded with one accelerometer.

To obtain a broader view of the system's dynamic behaviour, the Complex Mode Indicator Function (CMIF) can be used. This tool analyses the response from each accelerometer independently and provides a quick estimate of the number of modes. It also serves as a solid foundation for more advanced identification techniques. This method consist in evaluating the singular value decomposition of the FRF matrix $[H(\omega)]_{N_o \times N_i}$ at each spectral line, it writes

$$[\mathbf{H}(\omega)]_{N_o \times N_i} = [\mathbf{U}(\omega)]_{N_o \times N_o} \; [\mathbf{S}(\omega)]_{N_o \times N_i} \; [\mathbf{V}(\omega)]^T_{N_i \times N_i} \,, \tag{3.39}$$

where $\mathbf{U}(\omega_k)$ is a left singular vector that gives an approximation of the mode shapes $k$, $\mathbf{V}(\omega_k)$ is a right singular vector and represent the approximate force pattern necessary to generate a response on mode $k$, and $\mathbf{S}(\omega_k)$ is a diagonal matrix of singularities. Based on this decomposition, one can evaluate the CMIF defined as

$$[\mathbf{CMIF}(\omega_k)]_{N_i \times N_i} = [\mathbf{S}(\omega_k)]^T_{N_i \times N_o} \; [\mathbf{S}(\omega_k)]_{N_o \times N_i} \,. \tag{3.40}$$

Figure 3.13 presents the CMIF obtained from different experimental configurations. Peaks corresponding to all modes, including the first, are clearly identifiable. Two main effects were investigated: excitation type and clamping configuration.

First, Figure 3.13a compares the CMIF obtained using two piezoelectric actuators: DuraAct and MFC patches. As expected, MFC patches, better suited for torsional excitation, enhance the response of torsional modes, while DuraAct patches more effectively excite bending modes. Nonetheless, both actuators successfully excite all relevant modes. DuraAct patches were selected for the remainder of the study due to their higher response amplitudes, leading to better signal quality and improved identification.

Second, the influence of the clamping configuration was assessed by comparing results with and without the root-mounted balance, as shown in Figure 3.13b. While the balance is not expected to play a dominant role in the response, it does introduce a finite stiffness at the interface, in contrast to the ideal clamped boundary condition assumed in the theoretical model. A slight discrepancy appears near 50 Hz, where the configuration without the balance shows a double peak, possibly due to local flexibility or an unintended degree of freedom. In contrast, the configuration with the balance exhibits a cleaner single peak, suggesting a stiffer and more stable boundary closer to the ideal assumption.

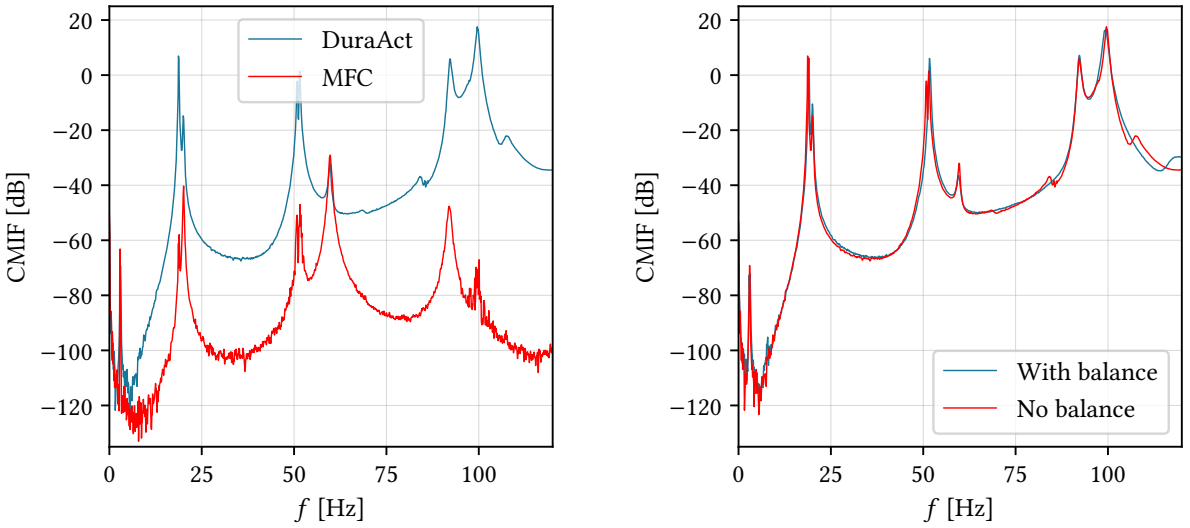


**(a)** Excitation effect.

**(b)** Clamping effect.

**Figure 3.13:** Comparison of the CMIF obtained experimentally to evaluate the effect of **(a)** the type of piezoelectric actuator, and **(b)** the clamping configuration.

To extract the damping ratios, the PolyMAX method was applied. Figure 3.14 presents the resulting stabilization diagram, where physical poles are highlighted with blue triangles. It can be seen that the first bending mode does not stabilize, likely due to poor measurement quality at low frequencies, as previously shown in Figure 3.12. Additionally, the second bending mode exhibits inconsistent damping stabilization, making its extraction more challenging. Despite these issues, six distinct lines can be clearly identified within the frequency range of interest. The identified poles align closely with the peaks observed in the CMIF obtained from the accelerometers, confirming the consistency of the modal extraction. The corresponding natural frequencies and damping ratios are summarized in Table 3.2.

Since the first mode could not be extracted using the identification method due to significant noise contamination in the low-frequency range. To overcome this limitation, a simple release test was performed to characterize the first mode, which is expected to be predominantly governed by the first bending deformation. The damping ratio was estimated using the logarithmic decrement method, which involves analysing the decay of successive peaks in the time-domain response. The method is based on

$$\ln\left(\frac{z_N}{z_{N+1}}\right) = 2\pi\zeta_S, \tag{3.41}$$

where $z_N$ denotes the amplitude of the $N^{\text{th}}$ peak in the displacement signal along the $z$-axis, and $\zeta_S$ is the structural damping ratio. By evaluating multiple successive peaks in the signal and plotting the

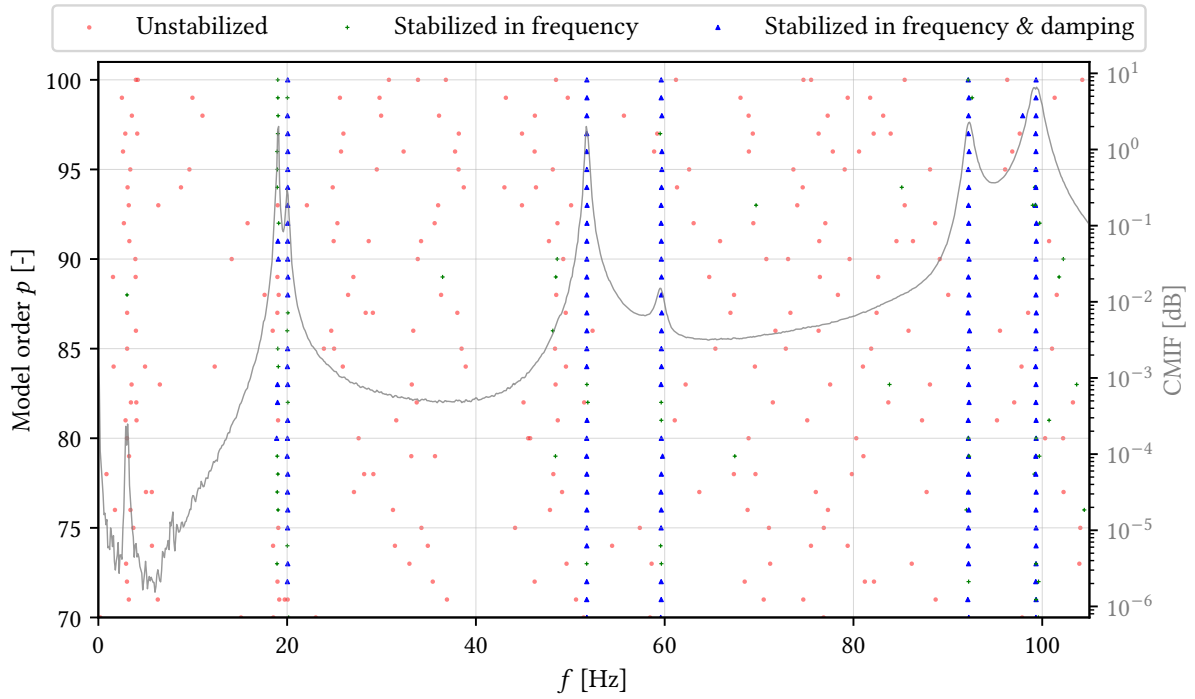


**Figure 3.14:** Stabilization diagram generated using the PolyMAX method, with stabilization thresholds set to $\varepsilon_f = 1\%$ for eigenfrequencies and $\varepsilon_\zeta = 20\%$ for damping ratios. The overlaid gray curve represents the CMIF.

logarithmic decrement, a linear fit can be applied to estimate the slope, from which the damping ratio is obtained. A summary of the results derived from the release test and the modal identification procedure is presented in Table 3.2.

Moreover, the relative error between the model predictions and experimental identification is presented in Table 3.2. It can be observed that the error remains below 3% for modes 1 to 5, indicating a good representation by the model. However, the sixth mode shows a larger discrepancy, suggesting that the predicted mode differs from the experimentally observed one. This discrepancy is attributed to the inherent limitations of the Rayleigh-Ritz method. The quality of the approximation improves with the number of degrees of freedom included in the formulation (Géradin & Rixen 2015, Wright & Cooper 2008). In the present study, three modes were retained for both bending and torsional deformations. When the number of basis functions is increased to four in each direction, the predicted frequency of the sixth mode shifts to 97.85 Hz, reducing the relative error to 6.12%. Nevertheless, as the objective of this study is to investigate the potential interaction between modes 2 and 3, the discrepancy observed in the sixth mode was considered acceptable.

Table 3.2: Comparison of experimental and model-predicted natural frequencies and damping ratios using the PolyMAX method in the reference configuration for the IAT wing.

| Number | 1 | 2 | 3 | 4 | 5 | 6 |
|---|---|---|---|---|---|---|
| $f_{\text{exp}}$ [Hz] | 3.039 | 19.02 | 20.05 | 51.75 | 59.64 | 92.21 |
| $f_{\text{model}}$ [Hz] | 3.069 | 18.98 | 20.28 | 53.09 | 60.79 | 100.26 |
| Rel. error [%] | +0.99 | -0.21 | +1.15 | +2.59 | +1.93 | +8.73 |
| $\zeta_{\text{exp}}$ [%] | 1.969 | 0.474 | 0.663 | 0.355 | 0.774 | 0.555 |

### Mode shapes identification

In order to reconstruct the mode shapes from the experimental measurements, the Least-Squares Frequency Domain (LSFD) method was implemented. The PolyMAX algorithm was first applied to provide a global estimation of the system's natural frequencies and damping ratios. Subsequently, the LSFD method was used to obtain local estimates, such as the residues, which are essential for accurate mode shape reconstruction. The implementation is conducted in the frequency domain, as it allows the specification of $\omega_{\text{min}}$ and $\omega_{\text{max}}$, enabling the evaluation of a frequency range where the coherence function approaches 1. Additionally, residual effects outside the frequency band can be explicitly considered. The FRF is expressed as

$$H_{rs}(\omega) = -\frac{1}{\omega^2 M_{rs}^R} + \sum_{k=m_1}^{m_2} \left( \frac{A_{rs(k)}}{i\omega - \lambda_k} + \frac{A_{rs(k)}^*}{i\omega - \lambda_k^*} \right) + \frac{1}{K_{rs}^R}, \tag{3.42}$$

where $m = m_2 - m_1$ corresponds to the number of modes in the frequency range $[\omega_{\text{min}}, \omega_{\text{max}}]$, and the residual terms $M_{rs}^R$ and $K_{rs}^R$ which are respectively describing the mass/stiffness behaviours. The expression $A_{rs(k)}$, $A_{rs(k)}^*$, $M_{rs}^R$ and $K_{rs}^R$ are unknowns of the system and represents local quantities. Expanding the residues into real and imaginary parts yields

$$H_{rs}(\omega) = -\frac{1}{\omega^2 M_{rs}^R} + \sum_{k=m_1}^{m_2} \left( U_{rs(k)} P_k(\omega) + i V_{rs(k)} Q_k(\omega) \right) + \frac{1}{K_{rs}^R}, \tag{3.43}$$

where $P_k(\omega)$ and $Q_k(\omega)$ are respectively given by

$$P_k(\omega) = \frac{1}{i\omega - \lambda_k} + \frac{1}{i\omega - \lambda_k^*} \qquad Q_k(\omega) = \frac{1}{i\omega - \lambda_k} - \frac{1}{i\omega - \lambda_k^*}. \tag{3.44}$$

This method takes advantage of the previous knowledge of the natural frequencies and damping ratios identified with the PolyMAX method, and the measured FRF obtained experimentally. In this context, Equation 3.43 leads to an over-determined system of equations which can be solved to obtain the $2m + 2$ unknowns provided that

$$\frac{\omega_{\text{max}} - \omega_{\text{min}}}{\Delta\omega} + 1 > 2m + 2, \tag{3.45}$$

where $\Delta\omega$ is the frequency resolution. The modes extracted with this method are complex. Therefore, it's required to extract real eigenmodes from the complex ones in order to allows the comparison between the model and experimental mode shapes. This extraction can be achieved using the method

$$z_{r(i)}^{\text{real}} = |z_{r(i)}| \, \text{sign} \left( \cos \phi_i \right), \tag{3.46}$$

where $\phi_i$ represents the phase angle associated with the $i^{\text{th}}$ element. This approach is efficient for lightly damped structures, where the phase angle $\phi_i$ remains close to $0°$ or $180°$. The validity of this assumption can be visually confirmed through the Argand diagram, which provides an evaluation of the complexity of the mode shapes. Figure 3.15 present the Argand diagrams corresponding to the complex modes 2 to 6 of the structure. It can be observed that the elements of these modes are nearly aligned in the same direction within the complex plane, indicating that the modes are almost real and the vibrations are in-phase.

Finally, the mode shapes within the frequency range of interest are shown in Figure 3.16. These figures were constructed using the 6 measurement points corresponding to the accelerometer locations which serve as reference points in the visualization. The experimental mode shapes are derived from the eigenvectors obtained using the LSFD method. Each mode shape is normalized with respect to its maximum amplitude and scaled for optimal visual clarity. Additionally, the theoretical mode shapes predicted by the model are superimposed for comparison. It can be observed that all modes exhibit a strong coupling between bending and torsion. Overall, the model captures the dynamic behaviour of the structure well, accurately representing the coupling between bending and torsion observed in the experimental results.

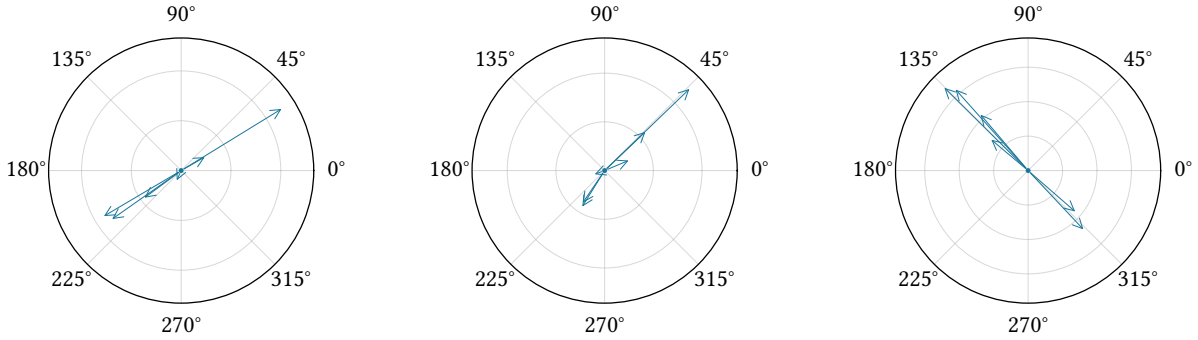


**(a)** Mode 2. **(b)** Mode 3. **(c)** Mode 4.

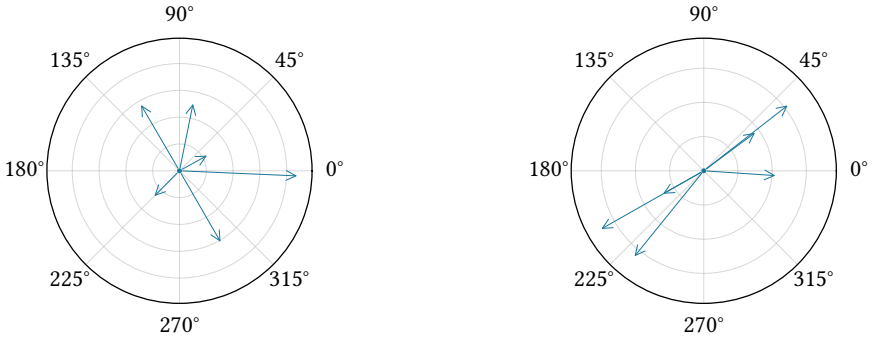


**(d)** Mode 5. **(e)** Mode 6.

**Figure 3.15:** Argand diagrams of the identified complex eigenmodes of the structure.

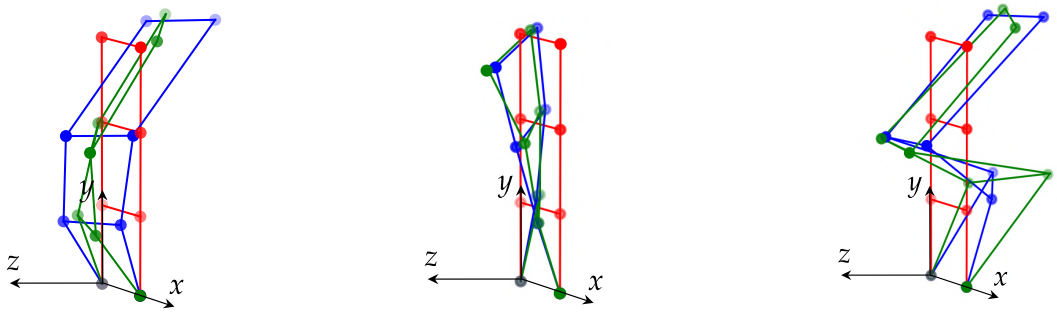


**(a)** Mode 2. **(b)** Mode 3. **(c)** Mode 4.


**(d)** Mode 5. **(e)** Mode 6.

**Figure 3.16:** Mode shapes 2 to 6 of the wing extracted from experimental measurement using LSFD (●) compared to mode shapes from the mathematical model (●) and initial configuration (●).

**Model validation**

The dynamic properties of the wing can be compared with the mathematical model and through the Modal Assurance Criterion which is mathematically defined as

$$\mathrm{MAC}\left(\boldsymbol{\psi}_x, \boldsymbol{\psi}_a\right) = \frac{|\boldsymbol{\psi}_x^T \boldsymbol{\psi}_a|^2}{\left(\boldsymbol{\psi}_x^T \boldsymbol{\psi}_x\right)\left(\boldsymbol{\psi}_a^T \boldsymbol{\psi}_a\right)}, \tag{3.47}$$

where $\boldsymbol{\psi}_x$ denotes an experimental mode shape obtained using the LSFD method and $\boldsymbol{\psi}_a$ corresponds to the analytical eigenvector from the model. The MAC value ranges between $0$ and $1$, providing a quantitative measure to evaluate similarities and differences between the modes. Figure 3.17 shows the MAC matrix between the analytical and experimental mode shapes. It can be observed that the MAC matrix exhibit a diagonal trend, indicating a good agreement between corresponding modes. However, some biasing is evident. As expected from mode shapes, some difference are noticeable for mode $2$ and $4$ which is quantified with a lower associated value on the MAC matrix diagonal. Especially, it can be observe that the diagonal value associated to mode $2$ is very low which can be associated to the quality of the measurement at low frequency, as further evidenced by the low coherence in Figure 3.12.

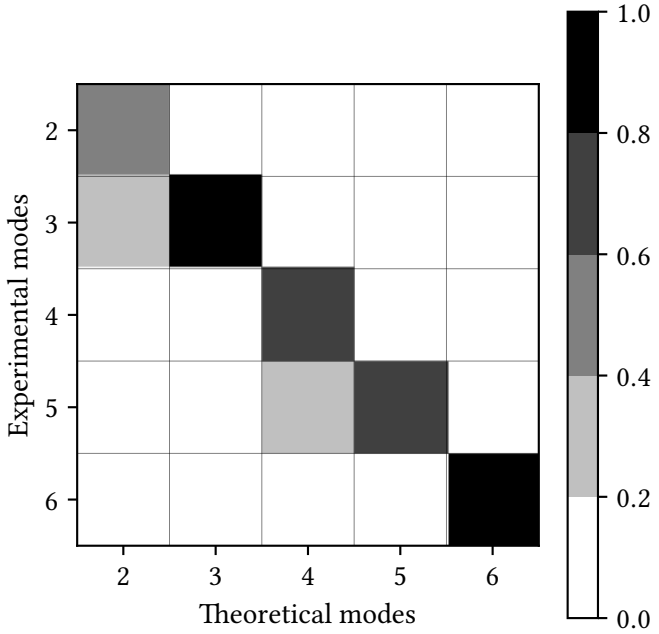


**Figure 3.17:** MAC matrix of the experimental modes identified with LSFD method and correlated with the analytical modes obtained using the mathematical model.

### 3.4.2 Aerodynamic coefficient measurement

In order to properly calibrate the aerodynamic model, it is essential to characterize the wing's aerodynamic behaviour. This was achieved through the evaluation of polar curves, which describe how aerodynamic coefficients vary with the angle of attack. The measurements were carried out using the turntable integrated into the wind tunnel setup. The balance was employed to capture the aerodynamic loads acting on the wing at a fixed freestream velocity, for various root angles of attack.

Figure 3.18 presents the measured polar curves for two freestream velocities. The evolution of the lift coefficient indicates that stall occurs at approximately $16°$. Additionally, the curves obtained at both velocities are nearly identical, demonstrating good repeatability of the measurements. From these results, the slopes of the lift and moment curves were extracted from their respective linear regions and used to

calibrate the aerodynamic model. The recorded values yield

$$\frac{\mathrm{d}C_L}{\mathrm{d}\alpha} \simeq 3.9 \quad , \quad \frac{\mathrm{d}C_M}{\mathrm{d}\alpha} \simeq 0.47. \tag{3.48}$$

It is observed that the lift curve slope is significantly lower than the theoretical value. This discrepancy can be attributed to two main effects. First, the influence of the 3D effect must be considered. The lift curve slope for a finite wing can be estimated using the corrected expression:

$$a = \frac{a_0}{1 + \frac{a_0}{\pi AR}(1+\tau)} \simeq 4.9, \tag{3.49}$$

where $a = \mathrm{d}C_L/\mathrm{d}\alpha$ is the corrected three-dimensional lift slope, $a_0 \simeq 0.9\ (2\pi)$ is the two-dimensional lift curve slope, $AR = 15$ is the wing's aspect ratio, and $\tau = 0.3$ is a correction factor accounting for the wing's geometry. Second, the effect of gaps between wing sections was investigated. To assess their influence, the gaps were sealed with tape during testing. The resulting measurements showed an increase in the lift curve slope to approximately $a \simeq 4.6$, which is in better agreement with the theoretical estimate.

In conclusion, the reduced lift slope observed in the initial measurements is primarily due to wing tip effects and the presence of inter-section gaps. Both sources of deviation are consistent with the corrected theoretical model.

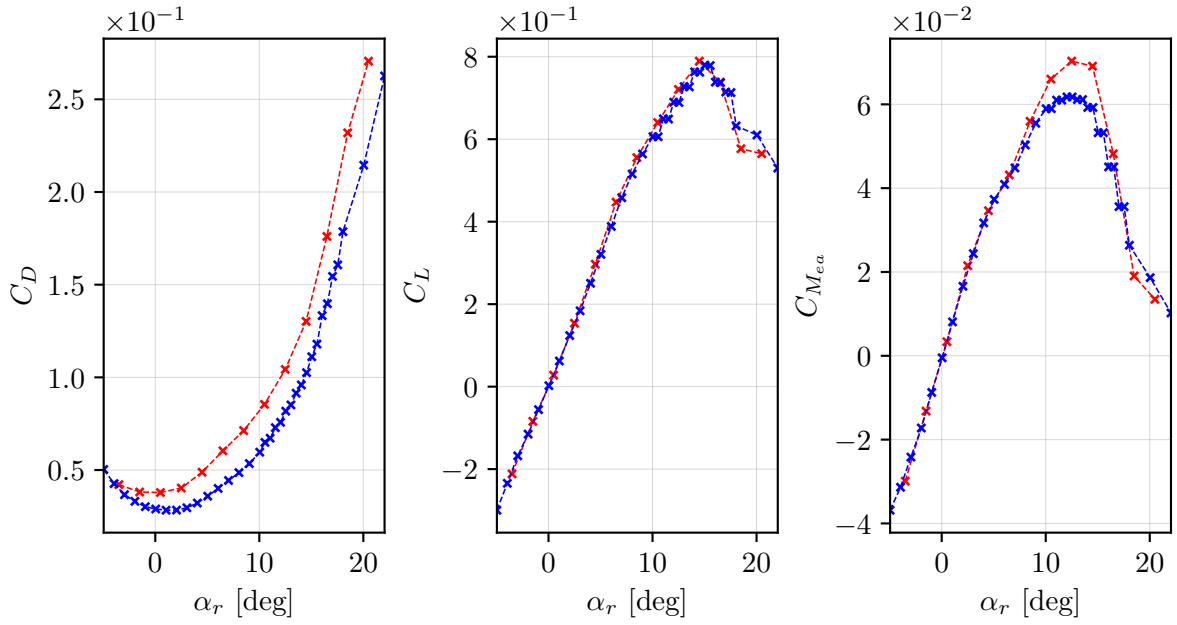


**Figure 3.18:** Polar curves of the wing for two freestream velocities: 15 m/s (-×-) and 20 m/s (-×-).

### Wingtip effect

Figure 3.19 presents the resulting polar curves for three wing tip configurations: without wing tip, with the *Ogive* tip, and with the *Saumon* tip. It can be observed that the wing tip configuration has only a small impact on the aerodynamic characteristics of the wing. The stall behaviour remains unchanged, and the slopes of the lift and moment curves, used for aerodynamic model calibration, are effectively identical across all configurations. Therefore, results presented in Equation 3.48 are used for all tested configuration.

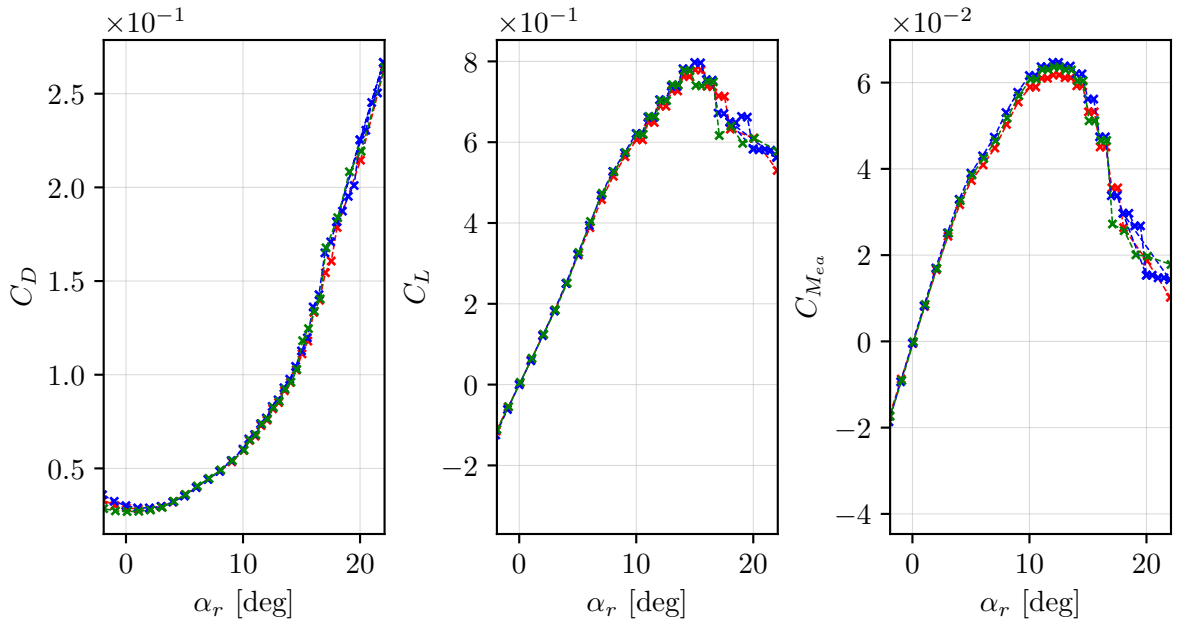


**Figure 3.19:** Polar curves of the wing for three configurations at $U = 20\,\mathrm{m/s}$: without wingtip (-×-), with *Ogive* wingtip (-×-), and with *Saumon* wingtip (-×-).

### Gap effect

Figure 3.20 presents the polar curves obtained during pitch-up and pitch-down motions for the wing with open gaps between the segmented sections. A clear aerodynamic hysteresis loop is observed in the stall region. Such hysteresis is often associated with the existence of bi-stable separated flow structures that can arise over the wing surface within a specific range of angles of attack. Although the flow remains separated during both the increasing and decreasing pitch phases, the topology of the separated region may differ, potentially leading to different aerodynamic responses.

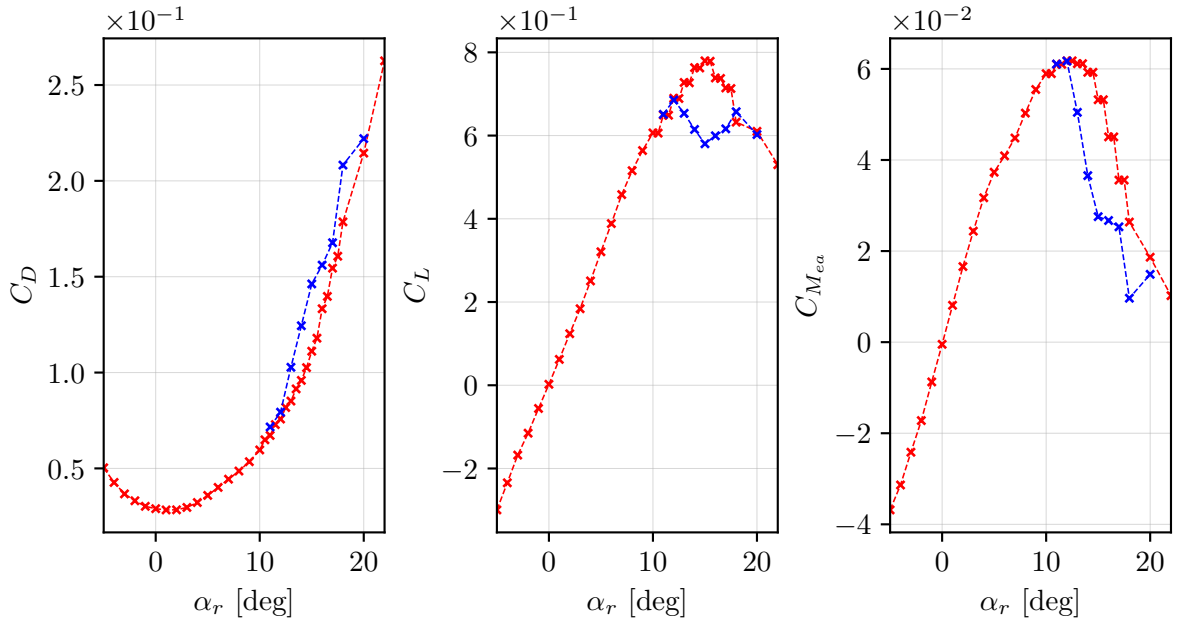


**Figure 3.20:** Polar curves of the wing for pitch-up (-×-) and pitch-down (-×-) phases.

In particular, the flow during the pitch-down phase appears to separate closer to the leading edge, which could explain the more significant loss in lift due to a diminished suction peak. This kind of behaviour

has been described by Sereez et al. (2024), though it is worth noting that their work was conducted on continuous wings without segmented gaps.

In the present case, the presence of open gaps might amplify such effects by promoting unsteady vortex interactions between sections. While the exact mechanisms remain to be confirmed, the diminution of the hysteresis loop when the gaps are sealed suggests a strong influence of inter-section flow dynamics. Furthermore, sealing the gaps leads to a noticeable increase in the lift-curve slope, possibly due to the suppression of three-dimensional disturbances and a more coherent flow over the wing surface. These observations suggest that the gaps play a non-negligible role in modifying the stall behaviour of the wing, although further investigation would be needed to isolate and confirm the underlying mechanisms.

### 3.4.3 Aeroelastic response

This section presents the dynamic response measurements obtained during the wind tunnel tests at IAT. Two wingtip configurations were investigated, as described in subsection 3.2.1.

#### *Ogive* wingtip

The *Ogive* wingtip was initially designed assuming a limited inertia. However, in practice, the wingtip exhibits greater inertia than expected which altered the dynamic behaviour of the structure. In particular, the bending and torsion frequencies were observed to be inverted, resulting in a modal divergence that prevented the onset of flutter within the tested velocity range. This divergence phenomena can be clearly observe in Figure 3.21.

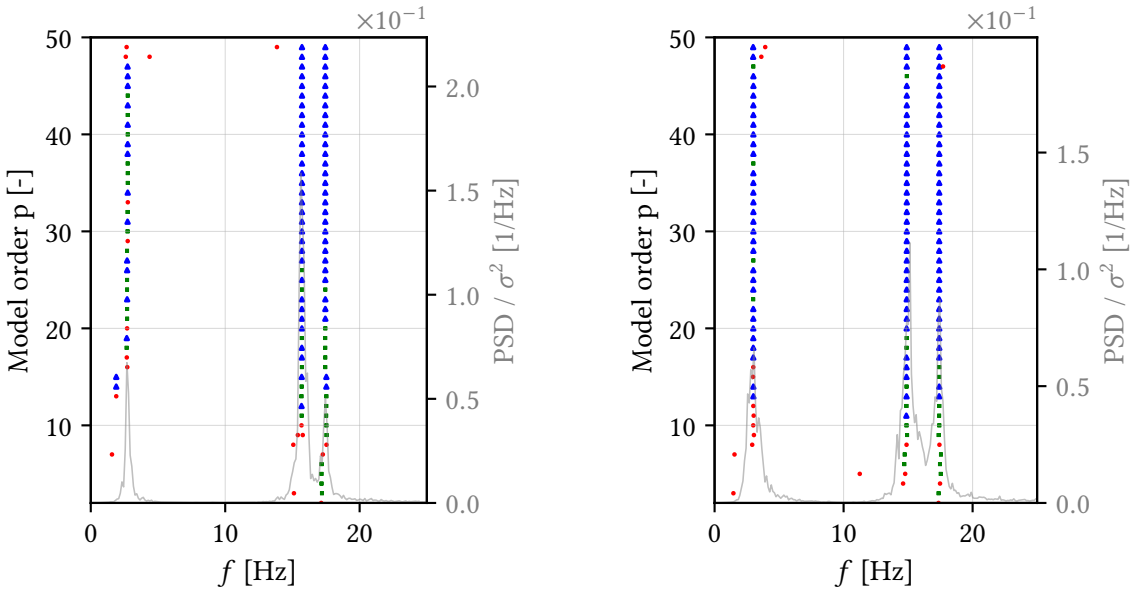


**(a)** $U = 10\,\mathrm{m/s}$. **(b)** $U = 27.5\,\mathrm{m/s}$.

**Figure 3.21:** Stabilization diagram obtained from time response signals at two different airspeeds for configuration 1 (see Table 3.3). The overlaid gray curve represents the normalized power spectral density of the corresponding signal captured by accelerometers.

This representation shows the stabilization diagrams obtained from time response measurements at two different freestream velocities. These diagrams were generated using the covariance-driven SSI method, with stabilization tolerances set to $\varepsilon_f = 0.5\%$ for the eigenfrequencies and $\varepsilon_\zeta = 1\%$ for the damping ratios. In the diagrams, blue markers indicate poles that are stable in both frequency and damping, green markers denote stability in frequency only, while red markers correspond to unstable poles. Additionally, a normalized PSD curve, shown in gray, is superimposed to aid interpretation. The PSD is scaled by the variance of the signal to ensure consistent comparison between test conditions. From the diagrams, one

can observe that the SSI method successfully captures the evolution of modal frequencies with increasing airspeed.

As expected, modal divergence occurs due to the added rotational inertia $I_{ty}$ of the wingtip, resulting in an inversion of the natural frequencies. Figure 3.22 presents the evolution of the identified frequencies and damping ratios as a function of freestream velocity, obtained using the SSI method. The configuration remains stable throughout the tested velocity range, as indicated by the diverging frequency trends and the generally increasing damping ratios. No flutter onset was observed.

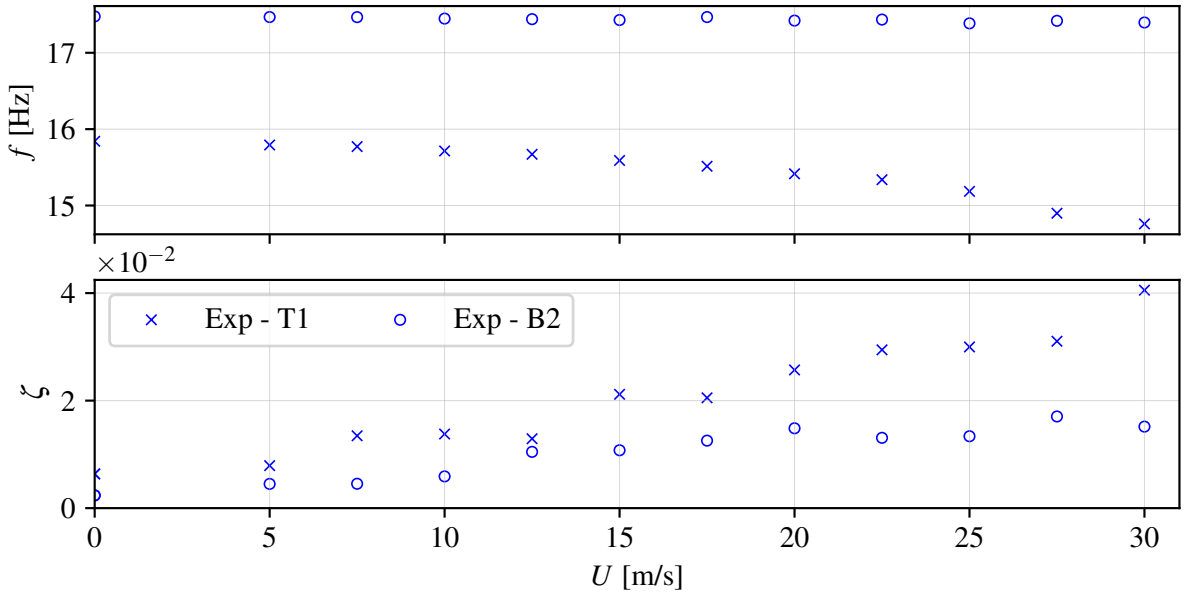


**Figure 3.22:** Evolution of natural frequencies and damping ratios as a function of freestream velocity for configuration number 1 (see Table 3.3).

To investigate conditions more favourable to flutter, several alternative configurations with varying tip mass and inertia were tested. These modifications aimed to alter the frequency content and promote mode coupling. A selection of these configurations is listed in Table 3.3.

Table 3.3: Configuration tested in the wind tunnel facility with *Ogive* wing tip.

| Number | Description | $M_t$ [kg] | $I_{ty}$ [kg m$^2$] | $X_t$ [m] |
|---|---|---|---|---|
| 1 | *Ogive* only | 0.170 | $2.36 \times 10^{-3}$ | 0 |
| 2 | *Ogive* with one mass of 218 g centered | 0.388 | $2.38 \times 10^{-3}$ | 0 |
| 3 | *Ogive* with one mass of 436 g centered | 0.605 | $2.53 \times 10^{-3}$ | 0 |
| 4 | *Ogive* with two masses of 109 g at 0.1 m from elastic axis | 0.388 | $4.54 \times 10^{-3}$ | 0 |
| 5 | *Ogive* with two masses of 109 g at 0.145 m from elastic axis | 0.388 | $6.94 \times 10^{-3}$ | 0 |

As the *Ogive* wingtip introduces significant rotational inertia, the torsional frequency is reduced below that of the second bending mode, inhibiting the onset of flutter. A potential solution is to increase the tip mass while keeping the added inertia relatively low, in order to promote coupling between the torsional and second bending modes. Among the tested cases, configuration 3 with $M_t \simeq 0.6$ kg, best meets this condition. The corresponding results are presented in Figure 3.23. It can be observed that the modal frequencies converges slightly, indicating that torsion frequency increases beyond the second bending frequency as a result of the added tip mass. However, this apparent frequency proximity does not necessarily imply that flutter will occur at higher velocities, as confirmed experimentally. No flutter onset was observed for this configuration, even at the highest tested speeds.

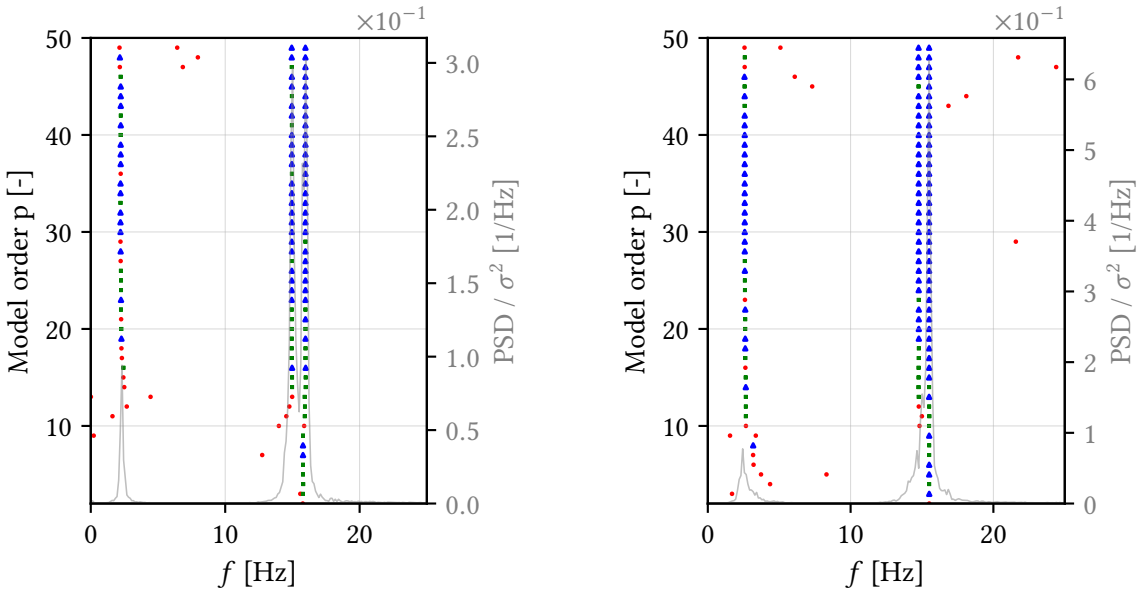


**(a)** $U = 10\,\mathrm{m/s}$. **(b)** $U = 27.5\,\mathrm{m/s}$.

**Figure 3.23:** Stabilization diagram obtained from time response signals at two different airspeeds for configuration 3 (see Table 3.3). The overlaid gray curve represents the normalized power spectral density of the corresponding signal captured by accelerometers.

To further investigate the dynamics of this configuration, Figure 3.24 presents the evolution of natural frequencies and damping ratios as a function of freestream velocity. While the frequencies tend to approach one another slightly, they do not appear to converge or interact significantly. Although flutter is often associated with frequency coalescence, this condition is not strictly necessary in general aeroelastic systems when aerodynamic damping is accounted for (Wright & Cooper 2008). For this reason, the evolution of damping ratios is commonly analysed.

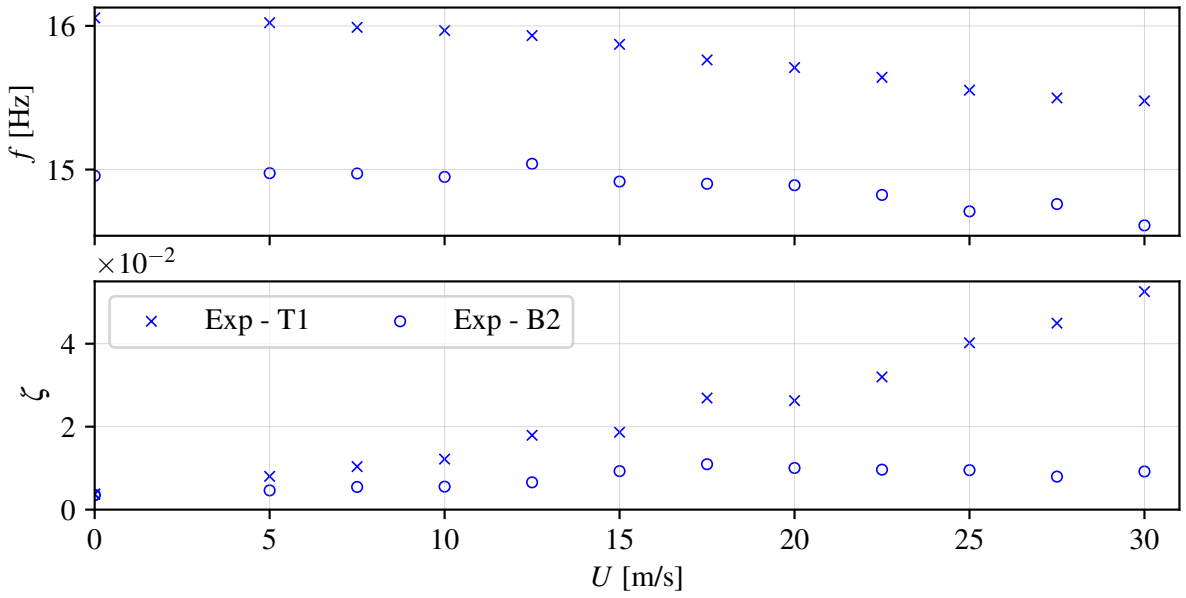


**Figure 3.24:** Evolution of natural frequencies and damping ratios as a function of freestream velocity for configuration number 3 (see Table 3.3).

In this configuration, the damping ratio associated with the second bending mode remains below that of the first torsional mode. Moreover, it exhibits a slight decrease before rising again around $U = 30\,\mathrm{m/s}$.

While this behaviour is not strongly marked, it may indicate the presence of a hump mode, as illustrated in Figure 2.3. In this context, comparison with the model prediction will help clarify the expected damping behaviour and support interpretation of the observed trends.

Given that the high rotational inertia introduced by the *Ogive* wingtip made flutter onset difficult to trigger within the tested range, further investigations were carried out using the *Saumon* wingtip, which is characterized by a significantly lower torsional inertia.

### *Saumon* wingtip

As explained , the *Saumon* configuration was designed in response to the excessive inertia introduced by the *Ogive* wingtip. Two variants were tested, and their properties are listed in Table 3.4.

Table 3.4: Configuration tested in the wind tunnel facility with *Saumon* wing tip.

| Number | Description | $M_t$ [kg] | $I_{ty}$ [kg m$^2$] | $X_t$ [m] |
|---|---|---|---|---|
| 1 | *Saumon* only | 0.0915 | $1.78 \times 10^{-4}$ | 0.033 |
| 2 | *Saumon* with two masses of 54 g and 218 g respectively at 0.055 m from TE and 0.045 m from LE | 0.362 | $6.11 \times 10^{-4}$ | 0.007 |

Figure 3.25 presents the stabilization diagrams obtained from time response measurements at two different freestream velocities for *Saumon* wingtip. From the diagrams, one can observe that the SSI method successfully captures the evolution of modal frequencies with increasing airspeed.

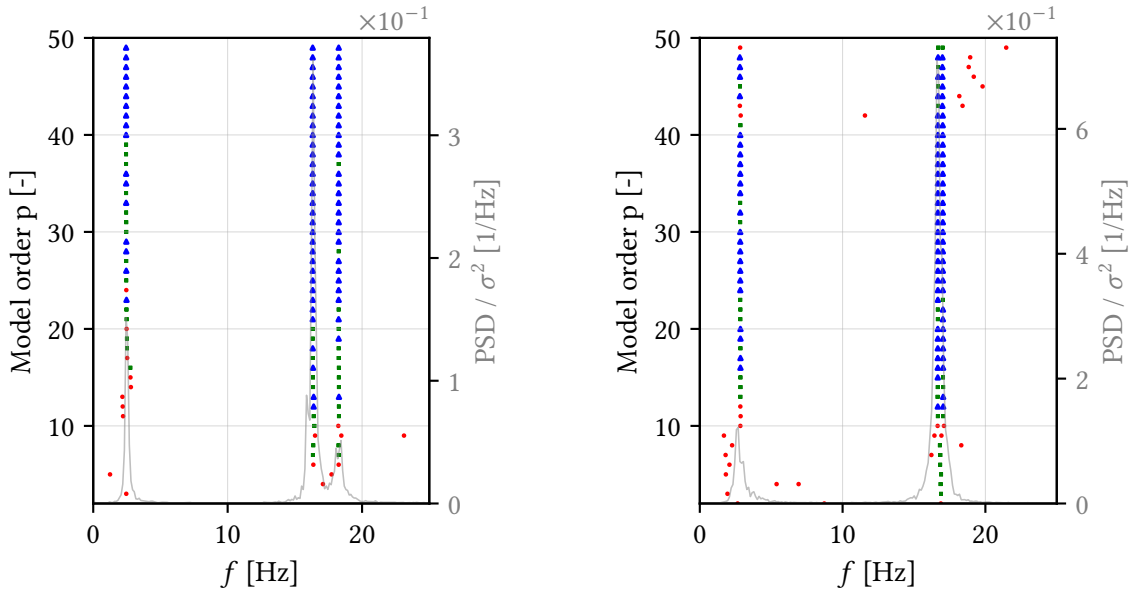


**(a)** $U = 10\,\mathrm{m/s}$. **(b)** $U = 27.5\,\mathrm{m/s}$.

**Figure 3.25:** Stabilization diagram obtained from time response signals at two different airspeeds for configuration 2 (see Table 3.4). The overlaid gray curve represents the normalized power spectral density of the corresponding signal captured by accelerometers.

The stabilization process in SSI method relies on the convergence of modal parameters such as natural frequencies and damping ratios across increasing model orders. However, near critical conditions, such as flutter onset, the damping ratio of the unstable mode approaches zero and may even become negative, making convergence more challenging. This behaviour is illustrated in Figure 3.26, where two modes are located in close proximity in the stabilization diagram. One of them (*e.g.* the blue marker) corresponds to a mode with relatively high damping and stabilizes clearly. The other (*e.g.* the green marker) is associated

with an unstable or nearly unstable mode and fails to stabilize. This can be interpreted as an energy exchange process between the two modes. As the aerodynamic coupling increases near the flutter speed, the stable and unstable modes interact through unsteady aerodynamic forces. Energy is progressively transferred from the unstable mode to the stable one, causing the damping of one to increase while the other decrease.

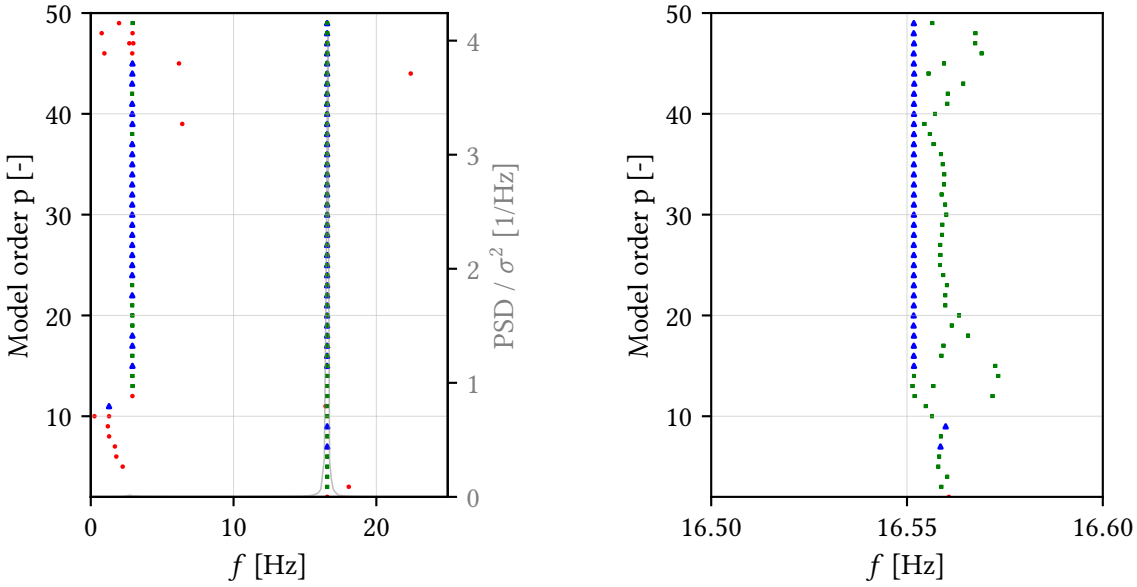


**Figure 3.26:** Stabilization diagram obtained from time response signals for configuration 2 (see Table 3.4) at $U = 33.3\,\mathrm{m/s}$ (left) and a zoom on the two closed frequencies (right). The overlaid gray curve represents the normalized power spectral density of the corresponding signal captured by accelerometers.

The results shown in Figure 3.27 indicate that, unlike the previous *Ogive* configuration, the two modes in the *Saumon* setup tend to converge as the freestream velocity increases. This trend suggests that the system becomes more prone to instability, with a potential modal interaction emerging at higher speeds. The torsional frequency decreases due to aerodynamic softening, while the bending frequency increases slightly under aerodynamic loading. According to the experimental data, the system appears to approach a potential instability near the highest tested velocity. However, it should be noted that these results were obtained using the SSI method, and the identification of low-damping modes in near-critical conditions must be interpreted with caution. No additional points were recorded beyond this velocity, as the wind tunnel was operating at its maximum capacity, preventing further testing that might have revealed the onset of flutter.

To further assess whether the system approaches flutter onset, time response signals for configuration 2 are presented in Figure 3.28. These signals, recorded at $U = 25, 30$ and $33.3\,\mathrm{m/s}$, are superimposed to highlight the evolution of the wing's dynamic response near critical conditions. As the velocity increases from 25 to 30 $\mathrm{m/s}$, a slight increase in vibration amplitude is observed, which can reasonably be attributed to the increase in turbulent excitation with airspeed. However, this variation remains moderate, indicating that turbulence alone has a limited impact on the amplitude growth in this range. In contrast, a further increase to $U = 33.3\,\mathrm{m/s}$ leads to a significantly larger response amplitude. This sharp rise cannot be explained by turbulence alone, as the previous trend showed only mild sensitivity. It instead indicates a reduction in system damping as the system approaches the flutter boundary. Despite this increase, no exponential divergence is observed. The response remains bounded within an amplitude envelope, exhibiting non-stationary oscillations that are characteristic of a system nearing, but not yet undergoing, a flutter instability. This phenomenon, known as the beating phenomenon, corresponds to an interference pattern resulting from the superposition of two signals with slightly different frequencies (Théodore 2020).

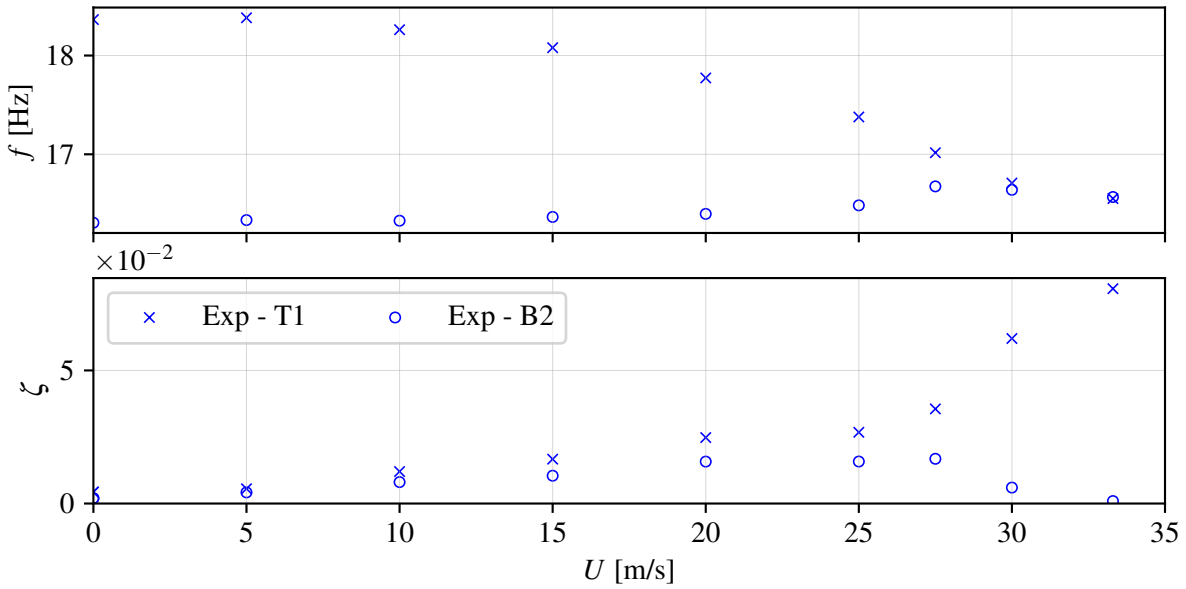


**Figure 3.27:** Evolution of natural frequencies and damping ratios as a function of freestream velocity for configuration number 2 (see Table 3.4).

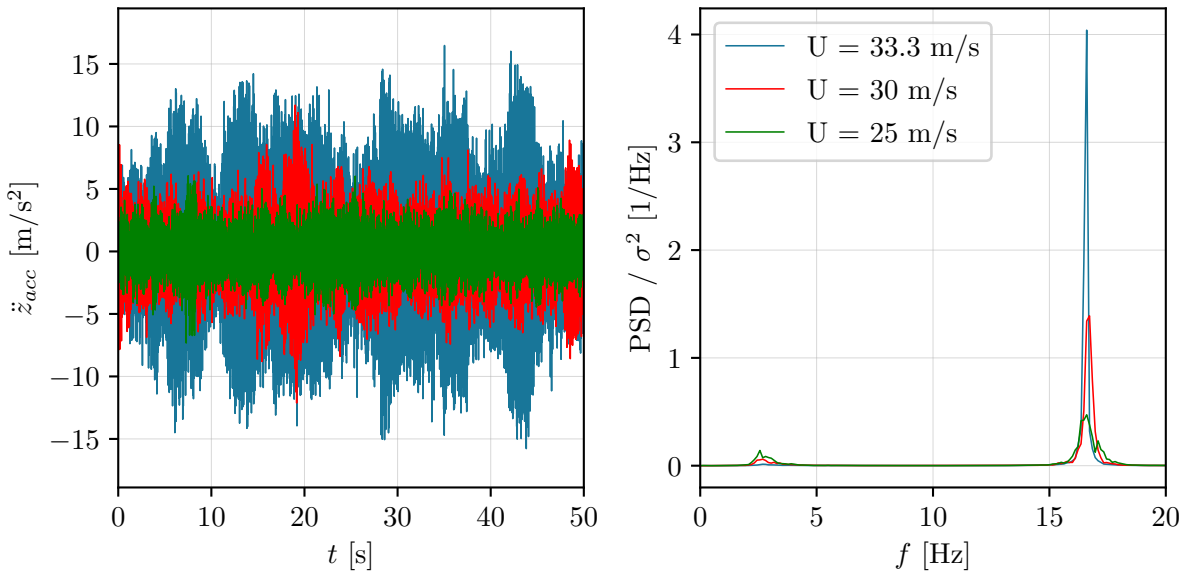


**Figure 3.28:** Time response of the wingtip acceleration measured by accelerometers (left), and the corresponding normalized power spectral density (right) for multiple freestream velocity.

Additionally, the normalized power spectral density of each signal is shown to illustrate the evolution of the frequency content with increasing freestream velocity. At $U = 25\,\mathrm{m/s}$, the spectrum exhibits two moderate peaks near 16 Hz, corresponding to lightly damped but stable structural modes, along with a lower-frequency peak associated with the first bending mode. As the velocity increases, the response becomes dominated by a single peak near 16.5 Hz, indicating a concentration of vibrational energy within a narrow frequency band. This shift suggests a transition from a multi-modal structural response to a predominantly aeroelastic response, characterized by the emergence of a mode near the critical flutter condition. This trend is further confirmed by the decreasing contribution of the first bending mode in the overall response. As the velocity increases, the amplitude of its associated spectral peak decreases,indicating that the structural modes are gradually dominated by the emerging aeroelastic mode. The clear evolution in frequency content, from the presence of multiple structural modes at low speed to the dominance of a

single mode at higher speed, supports the interpretation that the system is approaching a flutter instability.

Finally, as shown in Figure 3.29, the standard deviation of the wingtip acceleration increases gradually up to approximately $U = 20\,\mathrm{m/s}$, beyond which the slope becomes steeper, with a pronounced rise near $30\,\mathrm{m/s}$. This trend indicates a growing dynamic response amplitude, consistent with reduced damping and a system nearing aeroelastic instability. It is worth noting that the standard deviation at $U = 0\,\mathrm{m/s}$ is not zero, as the measurements were taken with the piezoelectric excitation system active, resulting in a non-zero baseline response.

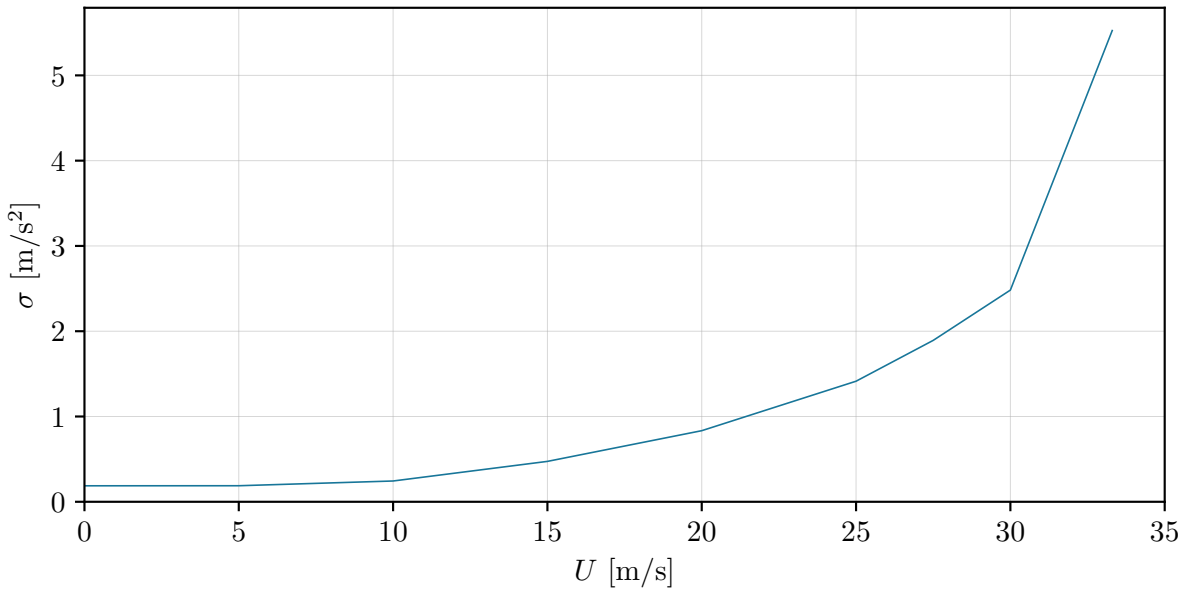


**Figure 3.29:** Evolution of the the standard deviation of the wingtip acceleration as a function of freestream velocity for configuration 2 (see Table 3.4).

#### Discussion and perspective

This test campaign ended with the failure of the wing in the S4 wind tunnel facility, caused by an aeroelastic instability. The failure occurred during incidence tests near stall condition ($\alpha_r = 16°$) at flow velocities above $25\,\mathrm{m/s}$. Although a classical galloping flutter dominated by the first bending mode was initially expected, the observed motion looked similar to a torsional stall flutter. The torsional mode was not pure and included bending components, but the instability was most likely triggered by a dynamic stall loop in torsion. This type of flutter was not observed when the gaps were sealed, suggesting that the dynamic stall behaviour and the hysteresis seen in static tests was significantly influenced by the open-gaps configuration. Predicting this kind of instability would require a dynamic stall model validated over a range of reduced velocities that includes the hysteresis effect and the gap effect.

## 3.5 ULiège wing

During this second test campaign, only a basic wind-off identification procedure was conducted. Since the wing shares the same airfoil profile as the one studied at IAT, no aerodynamic characterization was performed. Consequently, the model predictions presented in chapter 4 are based on identical aerodynamic coefficients for both wings.

### 3.5.1 Wind-off identification

As previously introduced, the wind-off characterization was carried out to calibrate the numerical model. In this context, only the natural frequencies and damping ratios were evaluated while the mode shapes

were neither extracted nor measured. The identification was performed using the SSI method, and the resulting stabilization diagram is presented in Figure 3.30.

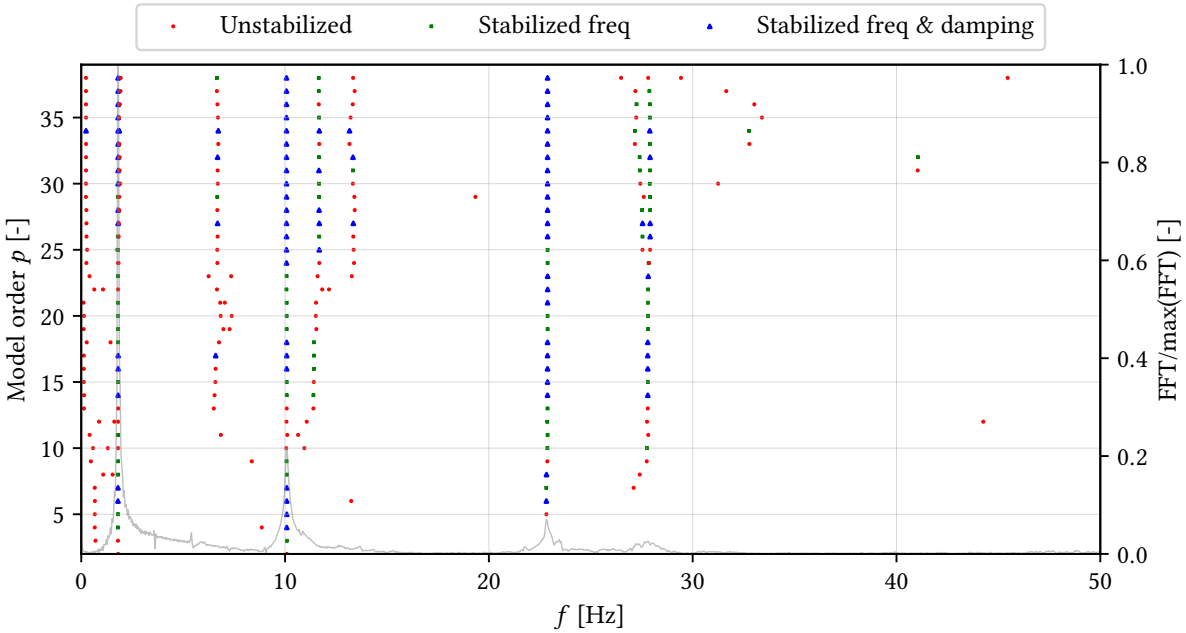


**Figure 3.30:** Stabilization diagram generated using the SSI method, with stabilization thresholds set to $\varepsilon_f = 1\%$ for eigenfrequencies and $\varepsilon_\zeta = 0.5\%$ for damping ratios. The overlaid gray curve represents the maximum-amplitude normalized FFT of the measured response.

It can be observed that the first four vibration modes are clearly stabilized. The identified values of frequency and damping for each mode are summarized in Table 3.5. Notably, the two modes of interest are separated by more than 10 Hz, suggesting that mode coupling, and thus flutter, can only occur at higher flow velocities. This separation is due to the underestimation of the torsional inertia during design process. Once the frequency were identified, the model was updated and frequency predicted are summarized in Table 3.5. Moreover, the relative error between the model predictions and experimental identification is also presented. It can be observed that the error remains below 10% for all modes, indicating a good representation by the model. The calibration was realised based on the frequency of interest which explained the good accuracy for second bending and first torsion mode.

Table 3.5: Comparison of experimental and model-predicted natural frequencies and damping ratios using the SSI method for the ULiège wing.

| Mode Number | 1 | 2 | 3 | 4 |
|---|---|---|---|---|
| $f_{\text{exp}}$ [Hz] | 1.803 | 10.069 | 22.879 | 27.895 |
| $f_{\text{model}}$ [Hz] | 1.626 | 10.147 | 22.922 | 28.260 |
| Rel. error [%] | $-9.575$ | $+0.803$ | $+0.179$ | $+1.307$ |
| $\zeta_{\text{exp}}$ [%] | 1.022 | 0.967 | 0.708 | 1.075 |

During the wind-off identification, the effect of gap closure on the dynamic characteristics was also investigated. To this end, the gaps between sections were sealed using a thin adhesive tape, and the identification procedure was repeated under identical conditions. The results, presented in Table 3.6, demonstrate that sealing the gaps significantly affects both the natural frequencies and the damping ratios of the structure.

From a frequency perspective, all four modes exhibit an increase when the gaps are sealed, with the third mode showing the most pronounced shift, increasing by approximately 17.6%. This can be attributed to

an increase in torsional stiffness, as the tape restricts relative motion between segments and effectively stiffens the system. As a result, the separation between modes of interest becomes larger reducing the likelihood of mode coupling and delaying potential flutter onset. In addition to the frequency shifts, a notable increase in damping ratios is observed across all modes. For instance, the damping of the third mode increases by nearly 392%, likely due to the constrained motion from the sealed gaps. While this may enhance stability, it significantly alters the system's dynamic behaviour. Given the modifications in both frequency and damping characteristics, the sealed configuration was not retained for the wind tunnel tests in order to preserve the possibility of capturing flutter-related phenomena

Table 3.6: Effect of gap sealing on natural frequencies and damping ratios identified using the SSI method for the ULiège wing.

| Mode Number | 1 | 2 | 3 | 4 |
|---|---|---|---|---|
| $f_{\text{ref}}$ [Hz] | 1.803 | 10.069 | 22.879 | 27.895 |
| $f_{\text{tape}}$ [Hz] | 1.843 | 10.479 | 26.914 | 30.189 |
| Rel. shift [%] | +2.22 | +4.07 | +17.64 | +8.22 |
| $\zeta_{\text{ref}}$ [%] | 1.022 | 0.967 | 0.708 | 1.075 |
| $\zeta_{\text{tape}}$ [%] | 1.814 | 1.906 | 3.486 | 2.452 |
| Rel. shift [%] | +77.50 | +97.10 | +392.37 | +128.09 |

### 3.5.2 Aeroelastic response

During this wind tunnel test, an additional identification procedure was used, exploiting the fact that the modes of interest are well separated. A single-mode nonlinear curve-fitting approach was applied to the amplitude spectrum derived from the FFT of the response signal. The method consists in fitting a theoretical second-order system model to the measured magnitude data by minimizing, in a least-squares sense, the error between the experimental and modelled frequency response. The fitted expression is given by

$$|H(\omega)| = \left| \frac{\phi}{\omega_r^2 - \omega^2 + 2i\,\zeta\,\omega_r\,\omega} \right|$$

where $\omega = 2\pi f$ is the pulsation, $\omega_r$ the natural pulsation, $\zeta$ the damping ratio, and $\phi$ a complex amplitude scaling coefficient. This formulation assumes a single-degree-of-freedom model in the frequency region around each mode. This approach is conceptually similar to Rational Fraction Polynomial (RFP) methods in that it fits a theoretical model to frequency-domain data, but it differs in key aspects. In particular, it relies solely on the magnitude of the response and employs a nonlinear optimization routine, whereas RFP methods typically operate on the full complex-valued FRF using linear regression. Although the RFP method is traditionally applied to transfer functions obtained from measured input-output pairs, this was not possible in the present case due to the absence of direct excitation measurements. Consequently, identification was carried out directly on the response spectrum. While this does not constitute a true RFP method, it remains a viable alternative for estimating modal parameters when modes are well separated. An illustration of the curve fitting results for the two dominant modes is provided in Figure 3.31. However, the method will be referred to as RFP for simplicity throughout the remainder of this work.

The extracted natural frequencies and damping ratios are presented in Figure 3.32, where results obtained using the modified RFP and SSI methods are compared. A gradual convergence of the two dominant frequencies is observed, although no frequency coalescence occurs during the test. Regarding the damping ratios, an initial increase is observed with airspeed, as expected, followed by a sudden drop around $U = 40$ to $45$ m/s which suggests the onset of flutter instability.

However, the measurement at $U = 40$ m/s was excluded from the analysis due to significant packet loss.

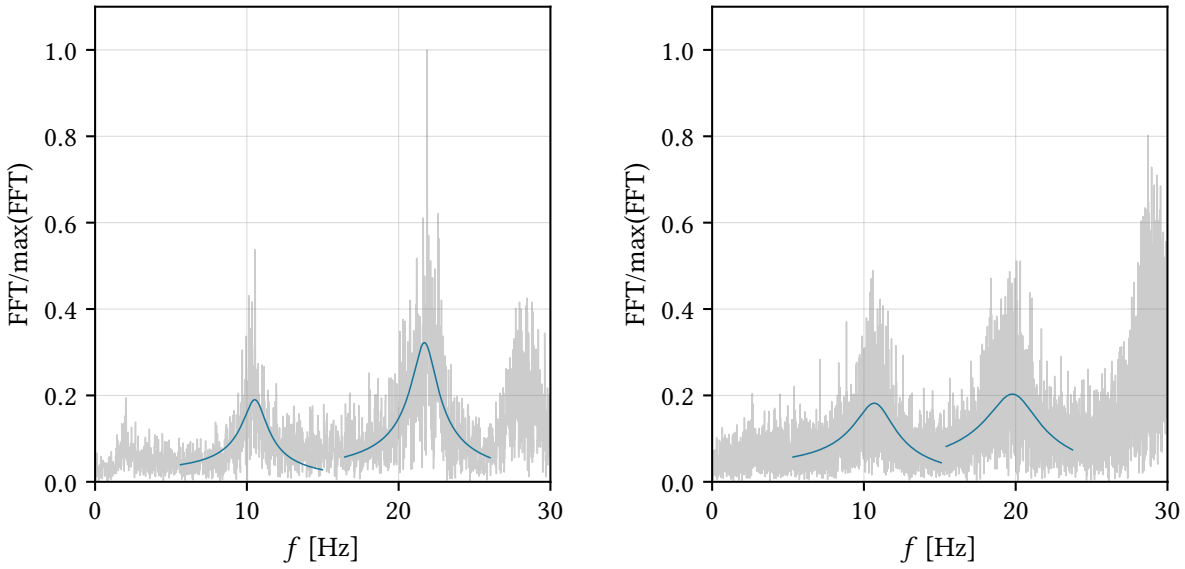


**(a)** $U = 20\,\mathrm{m/s}$. **(b)** $U = 35\,\mathrm{m/s}$.

**Figure 3.31:** Curve fitting of the two dominant modes on the normalized FFT amplitude spectrum for two flow velocities. The raw acceleration spectra (—) are plotted alongside the fitted second-order single-mode responses (—).

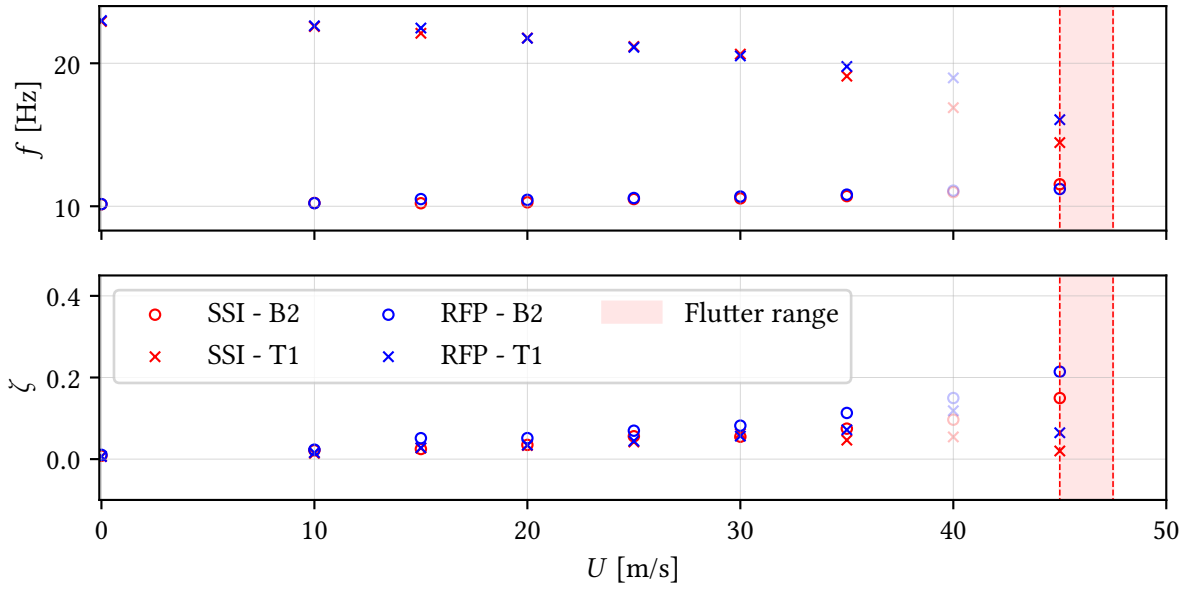


**Figure 3.32:** Evolution of natural frequencies and damping ratios as a function of freestream velocity for ULiège configuration. Results extracted using SSI and RFP method. Red regions illustrate the range of velocity in which flutter occured.

This issue is clearly visible in Figure 3.33a, which presents the time step between successive recorded samples. It can be seen that many steps are missing, such that the effective time step deviates from the expected $\Delta t = 1/f_{\text{samp}} \simeq 5 \times 10^{-3}\,\text{s}$. This has a direct impact on the frequency-domain representation shown in Figure 3.33b, where the FFT exhibits a double peak near 20 Hz which was not present in earlier measurements. The packet loss introduces irregular time steps and effectively alters the sampling rate locally, violating the assumption of uniform sampling required by the FFT. As a result, the signal is no longer accurately projected onto the frequency basis, leading to spectral leakage and the appearance of spurious frequency components.

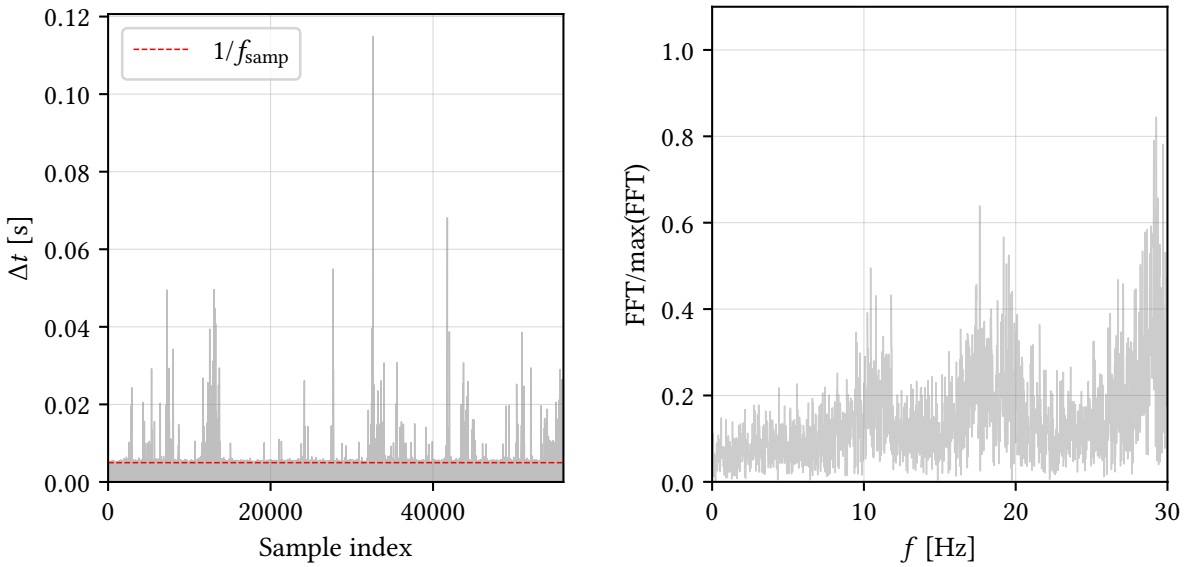


**(a)** Time step irregularities caused by packet loss. **(b)** Distortion of the frequency content for $U = 40\,\mathrm{m/s}$.

**Figure 3.33:** Effect of packet loss on time-domain sampling and its consequence on frequency-domain identification.

The comparison between SSI and RFP shows similar results up to $U = 30\,\mathrm{m/s}$, beyond which discrepancies begin to appear. Notably, the SSI method predicts a faster convergence of modal frequencies than RFP. However, the evolution of the second bending frequency remains consistently captured by both methods. In terms of damping, both methods indicate a clear reduction in torsional damping near critical conditions. Still, due to the degraded data quality at $40\,\mathrm{m/s}$, no definitive conclusions can be drawn about the behaviour close to flutter onset. Nonetheless, both identification methods provide consistent results and align with the experimental observation of flutter onset at higher airspeeds. As shown in Figure 3.32, the flutter speed is represented as a range rather than a single value. This is because the wing entered flutter during a continuous wind speed ramp, preventing precise identification of the critical speed. Consequently, an interval between $45$ and $47.5\,\mathrm{m/s}$ was chosen to reflect the experimental speed increment.

The onset of flutter is illustrated in Figure 3.34a, which displays a superposition of two successive frames capturing the early stage of the instability. A clear torsional motion about the elastic axis is visible, particularly at the wingtip. This sequence was recorded just before the oscillation amplitude grew exponentially, ultimately leading to structural failure, as seen in Figure 3.34b. The failure occurred at the wing clamping interface. Additionally, the wing exhibits significant deformation in the streamwise direction, mainly attributed to large drag forces acting under high effective angle of attack conditions.

However, it should be noted that it remains uncertain whether the flutter occurred naturally or was triggered by a fracture at the clamping. Since the tests were conducted over a $5$ minute duration to enable accurate SSI identification, it is possible that micro-cracks developed at the clamping interface during this period. Such damage could reduce the local stiffness and, in turn, lower the actual flutter speed compared to an ideal clamping condition (Riazat & Kheiri n.d.).

**(a)** Flutter onset. **(b)** Wing failure.

**Figure 3.34:** Visual illustration of the flutter phenomenon captured during the experimental campaign at ULiège. The left image shows the onset of instability, while the right image corresponds to the structural failure occurring shortly after flutter.

# Chapter 4

# Experimental and numerical comparison

This final chapter aims to compare the experimental results with the model predictions. In particular, the results presented in subsection 3.4.3 and subsection 3.5.2 are confronted with the outcomes of the model introduced in chapter 2. Furthermore, this chapter investigates the influence of uncertainties associated with specific model inputs that are difficult to measure accurately. Finally, the similitude and differences between the two tested wings are presented and discussed.

## 4.1 IAT wing

Firstly, it was already shown that the model provides results in good agreement with the wind-off configuration. Indeed, the results presented in Table 3.2 closely match the experimentally measured natural frequencies. Additionally, the model's accuracy was confirmed by the good agreement in mode shapes, assessed using the Modal Assurance Criterion, as shown in Figure 3.17. These results indicate that the model performs reliably in wind-off conditions, provided that accurate input parameters are used. In this context, the following comparison will primarily focus on aeroelastic responses.

First of all, no configuration with the *Ogive* wingtip exhibited dynamic instabilities. This observation is consistent with the model predictions. Indeed, all tested configurations correspond to regions where no flutter was predicted, as illustrated in Figure 2.9. Nevertheless, analysing the evolution of natural frequencies and damping ratios remains essential to further assess the model's accuracy. Figure 4.1 presents a comparison between predicted and measured frequencies and damping ratios as functions of the freestream velocity. Overall, the dynamic behaviour is well captured by the model, although some discrepancies are noticeable, particularly in the damping trends.

As previously mentioned, configuration 1 is identified as stable, as evidenced by the diverging frequency trends and the generally increasing damping ratios, both of which are well reproduced by the model. Moreover, the bending mode (B2) is accurately captured, with model predictions closely matching the experimental observations. In contrast, the torsional mode (T1) appears more difficult to model, especially at higher velocities, where experimental results increasingly deviate from the predictions. Additionally, discrepancies are also observed under wind-off conditions for configuration 3, which may be attributed to inaccuracies in the model's input parameters and may partly explain the observed deviations. Despite these deviations, it can be concluded that the model effectively captures the overall dynamics of the system, with the experimental data showing good agreement with the predicted results.

Concerning the *Saumon* configuration, the results are presented in Figure 4.2. It can be observed that the model accurately captures the overall dynamic behaviour of both modes. Furthermore, regarding the damping ratio trends, the model successfully predicts the point at which the damping ratio decreases for the second bending mode and increases for the first torsional mode. However, the following trend is not perfectly reproduced. Indeed, while the model does not predict flutter, the experimental results suggest the onset of a potential instability near the highest recorded velocity. If flutter were to occur, it

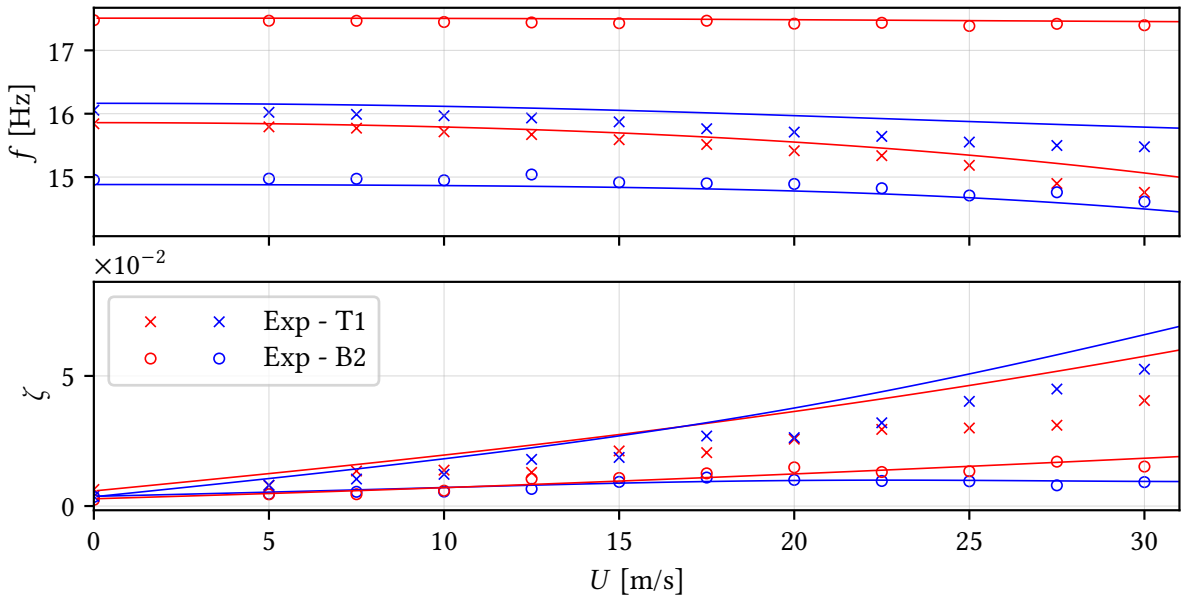


**Figure 4.1:** Evolution of natural frequencies and damping ratios as a function of freestream velocity for configuration 1 (—) and configuration 3 (—) with *Ogive* wingtip (see Table 3.3). Results obtained numerically with unsteady Theodorsen model (US) are superimposed to experimental results.

would likely do so at a slightly higher velocity, within a close velocity range, as the observed evolution is characteristic of a hump mode behaviour, marked by a slight decrease which can be followed by an increase in damping.

The damping evolution of the second bending mode is well predicted up to 27.5 m/s, whereas the increasing damping of the first torsional mode is consistently overestimated across all tested configurations. The frequency evolution is also well captured, although the coalescence of both modes is predicted at a lower velocity than observed experimentally.

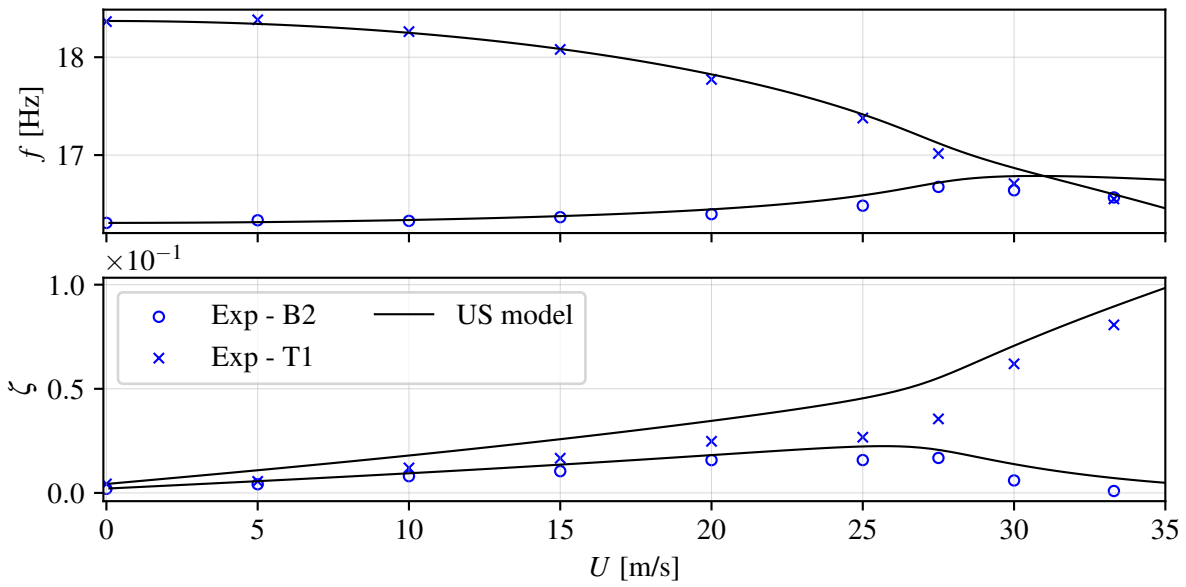


**Figure 4.2:** Evolution of natural frequencies and damping ratios as a function of freestream velocity for configuration number 2 with *Saumon* wingtip (see Table 3.4). Results obtained numerically with unsteady Theodorsen model (US) are superimposed to experimental results.

### 4.1.1 Impact of structural uncertainties

The structural parameters used in the present model were initially defined and calibrated in the work of Prieur (2023) to reproduce experimental results, in the absence of a dedicated structural characterization procedure (see section C.2). Ideally, however, these parameters should have been experimentally identified during the wind tunnel campaign to reduce model uncertainty.

In this context, the current section aims to assess the impact of uncertainties in structural and inertial properties on the accuracy of the model predictions. The parameters considered include the mass per unit length $m$, the torsional moment of inertia per unit length $I_\alpha$, the flapwise bending stiffness $EI_x$, and the torsional stiffness $GJ$. It should be noted that, due to the assumption of a 2-DOF model , the chordwise bending stiffness $EI_z$ does not influence the aeroelastic response and is therefore excluded from the analysis. The sensitivity study is performed by independently varying the inertial quantities $m$ and $I_\alpha$, while recalibrating the corresponding stiffnesses to preserve the wind-off natural frequencies. This approach allows the effect of each uncertainty to be isolated while maintaining consistency with static test conditions.

As an initial investigation, the mass per unit length $m$ was varied within a range of $\pm 20\%$. The resulting model predictions are presented in Figure 4.3a. It can be observed that the influence of $m$ remains relatively limited and only becomes noticeable for velocities above approximately $20\,\mathrm{m/s}$. The primary effect lies in the evolution of the damping ratio prior to flutter onset, where changes in $m$ affect the amplitude and shape of the damping peak that occurs before the drop associated with flutter onset.

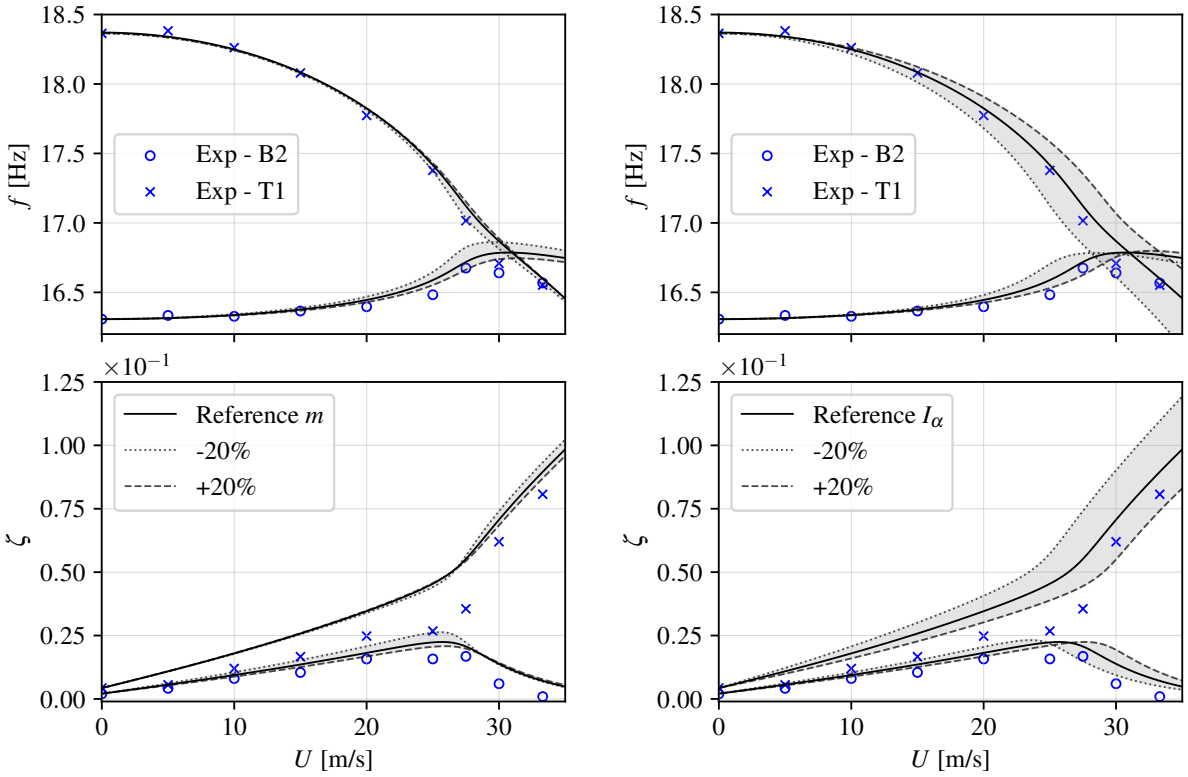


**(a)** Effect of mass per unit length $m$.

**(b)** Effect of moment of inertia per unit length $I_\alpha$.

**Figure 4.3:** Effect of uncertainties in structural parameters on the evolution of natural frequencies and damping ratios as a function of freestream velocity for the *Saumon* configuration at IAT. Experimental results extracted using the SSI method are compared with numerical predictions from the unsteady Theodorsen model (US). The shaded regions represent the envelope of predictions obtained by varying structural parameters within $\pm 20\%$ of their reference values.

In contrast, variations in the torsional moment of inertia $I_\alpha$ have a much more pronounced impact on the aeroelastic behaviour, as shown in Figure 4.3b. As observed, a reduction in $I_\alpha$ accelerates the con-

vergence between the two modes, leading to an earlier and more severe damping drop. Conversely, increasing $I_\alpha$ stiffens the torsional response, resulting in a delayed interaction and the damping drop occurs at higher velocity. Moreover, the variation of $I_\alpha$ has a significant impact on both the frequency and damping evolution of the torsional mode, an effect that is considerably stronger than that observed for the bending mode when modifying $m$.

## 4.2 ULiège Wing

In this section, the model predictions obtained using the parameters listed in Table 3.1 are compared to the experimental results. As previously mentioned, no aerodynamic characterization was performed during this campaign. Consequently, the aerodynamic coefficients used in the model were those identified during the IAT campaign. The influence of the uncertainties on aerodynamic coefficient is discussed in subsection 4.2.1.

The comparison is presented in Figure 4.4. It can be observed that the overall dynamic behaviour is well captured by the model, both in terms of frequency evolution and damping trends. The predicted frequency content shows better agreement with the experimental results obtained using the SSI method, while the damping ratios appear to align more closely with the values extracted via the RFP method.

The model predicts a flutter speed of $U_{\text{crit}} = 47.8\,\text{m/s}$, which is slightly higher than the experimental observation. Flutter was experimentally identified to occur between $U = 45\,\text{m/s}$ and $47.5\,\text{m/s}$. In this context, the model overpredicts the flutter speed by a maximum relative error of $\varepsilon_{\text{rel}} = 6.22\,\%$ when compared to the lower bound of the observed flutter interval. For comparison, the flutter prediction technique proposed by Zimmerman & Weissenburger (1964) was applied to the same dataset and yielded a predicted flutter speed of $46.71\,\text{m/s}$. This result falls within the experimentally observed interval and reduces the relative error to $\varepsilon_{\text{rel}} = 3.8\,\%$.

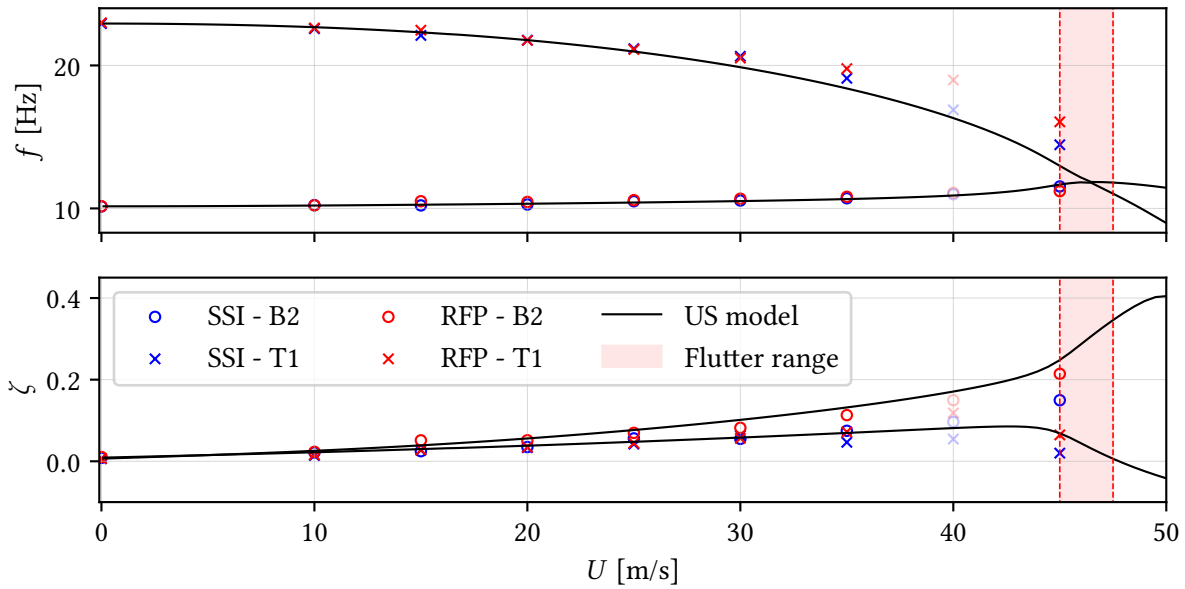


**Figure 4.4:** Evolution of natural frequencies and damping ratios as a function of freestream velocity for ULiège configuration. Results extracted using SSI and RFP method. Red regions illustrate the range of velocity in which flutter occured. Results obtained numerically with unsteady Theodorsen model (US) are superimposed to experimental results.

### 4.2.1 Influence of aerodynamic uncertainties

The parameters used in the model were determined during the design phase and the wind-off characterization of this campaign. The only remaining unknown is the aerodynamic coefficient defining the wing's

behaviour. Since the wing retains the same airfoil section as the IAT wing, it was assumed that the aerodynamic coefficient could be directly reused. However, the validity of this assumption must be verified. To this end, the model was tested by varying the aerodynamic coefficient within a range of -20% to +20%. The corresponding results are presented in Figure 4.5.

It can be observed that variations in the aerodynamic coefficient have limited impact on the model predictions up to approximately 30 m/s. Within this range, only the torsional branch exhibits slight changes. Specifically, an increase in the aerodynamic slope causes the torsional frequency to decrease more rapidly with velocity. This trend leads to an earlier mode interaction, which results in a lower predicted flutter speed, as reflected in the evolution of the damping curves.

Experimentally, flutter was observed at a lower velocity than predicted by the nominal model. This discrepancy suggests that the actual aerodynamic coefficient may be higher than initially assumed. However, while increasing this coefficient improves the accuracy of flutter speed prediction, it leads to poorer agreement with the frequency evolution, especially at higher velocities, where the measured frequencies exceed those predicted by the model.

In this context, the nominal aerodynamic coefficient appears to offer a reasonable compromise, providing a satisfactory match with both the frequency and damping trends observed experimentally.

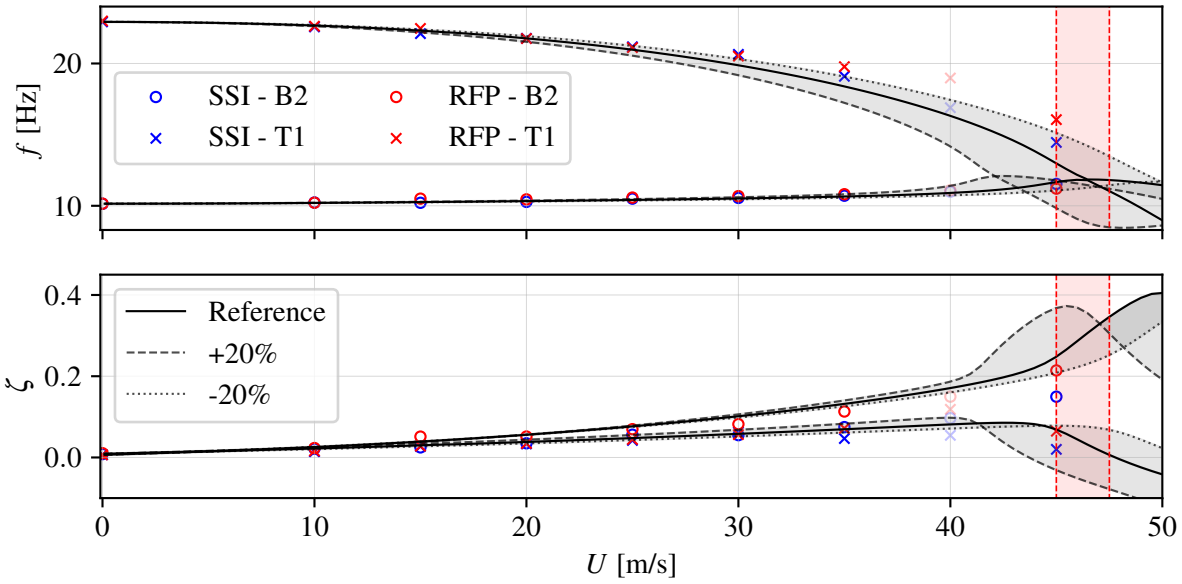


**Figure 4.5:** Evolution of natural frequencies and damping ratios as a function of freestream velocity for ULiège configuration. Results extracted using SSI and RFP method are shown alongside numerical predictions from the unsteady Theodorsen model (US). The numerical curves correspond to variations of the aerodynamic coefficient within ±20% of the reference value. Red regions illustrate the range of velocity in which flutter occurred.

## 4.3 Cross-configuration comparison

This final section aims to evaluate the similarities and differences between the two tested wing configurations. Since the geometries are not identical, the comparison is based on non-dimensional parameters. First, it is observed that both configurations were tested within a similar Reynolds number range

$$Re^{\text{IAT}} = \frac{U_{\max}\, c}{\nu} \simeq 4.5 \times 10^5 \quad , \quad Re^{\text{ULiège}} \simeq 4.9 \times 10^5 \tag{4.1}$$

where $\nu = 1.48 \times 10^{-5}\,\text{m}^2\,\text{s}^{-1}$ is the kinematic viscosity of air at ambient temperature. Despite the geometric differences between the IAT and ULiège wings, the aerodynamic conditions during testing

were comparable, as evidenced by their similar Reynolds numbers.

Additionally, the Scruton number was evaluated. This dimensionless parameter provides insight into the relative importance of structural damping compared to inertial effects, which can significantly influence the onset of vortex-induced vibrations and flutter. It writes

$$Sc = 4\pi\zeta_s m_r \quad \text{with} \quad m_r = \frac{m}{\rho\pi(c/2)^2}, \tag{4.2}$$

where $\zeta_s$ is the structural damping ratio, and $m_r$ describes the mass ratio between the structure and the volume of fluid displaced. The Scruton number was found to be similar between the two tested configurations. This is explained by the fact that the damping ratio identified during the ULiège campaign was approximately twice that of the IAT campaign, while the mass per unit length $m$ of the ULiège wing was approximately half that of the IAT wing.

Moreover, it was observed that the ratio of the measured inertial quantities appears to be similar between the two configurations. Specifically, the ratios of mass and torsional moment of inertia between the IAT and ULiège wings are given by

$$\lambda_m = \frac{m^{\text{IAT}}}{m^{\text{ULiège}}} = 2.169 \quad , \quad \lambda_{I_\alpha} = \frac{I_\alpha^{\text{IAT}}}{I_\alpha^{\text{ULiège}}} = 2.164. \tag{4.3}$$

Although this proportionality between inertial properties is preserved, it was observed that the same does not hold for the wind-off natural frequencies. This discrepancy is attributed to the significant difference in stiffness between the $H$-shaped beam used in the IAT configuration and the simpler rectangular beam employed at ULiège. This structural difference results in a different frequency ratio, which is expressed as

$$\gamma^{\text{IAT}} = \left(\frac{f_\alpha}{f_h}\right)^{\text{IAT}} = 1.05 \quad , \quad \gamma^{\text{ULiège}} = \left(\frac{f_\alpha}{f_h}\right)^{\text{ULiège}} = 2.27. \tag{4.4}$$

However, it was observed that the IAT configuration does not exhibit any sign of dynamic instability or flutter onset. To further investigate this, a comparison is drawn with the *Saumon* configuration, which approaches the instability boundary and is characterized by a slightly higher frequency ratio of $\gamma^{\text{IAT}} = 1.12$. At first glance, this observation may appear counter-intuitive, as one might expect flutter to occur when the bending and torsional modes are closer in frequency, *i.e.* when $\gamma \simeq 1$. However, as demonstrated in the work conducted by Wen et al. (2025), the relationship between the flutter onset and the frequency ratio is not monotonic. Indeed, flutter onset is governed not only by frequency proximity, but also by damping level, inertia ratios, and aerodynamic coupling strength. A qualitative representation of structural damping impact on flutter dynamic is presented in Figure 4.6.

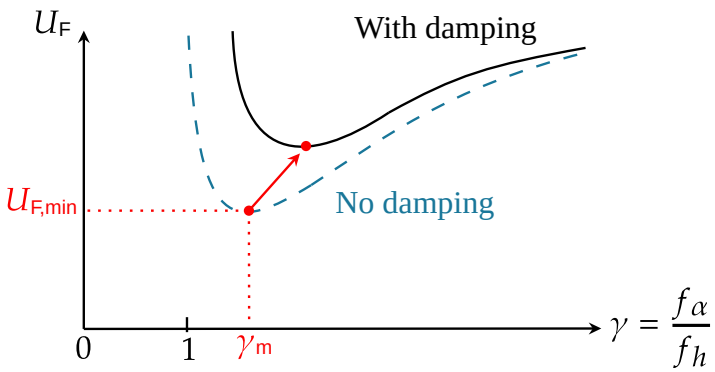


**Figure 4.6:** Flutter speed diagram as a function of the frequency ratio. The effect of structural damping is illustrated. Figure reproduced from Wen et al. (2025).

Then, the evolution of frequency ratio as a function of reduced velocity $U/(f_\alpha b)$ was evaluated for both

ULiège and IAT (*Saumon*) configurations. The results, including experimental measurements and theoretical predictions, are presented in Figure 4.7.

It can be observed that both configurations tend to converge towards $\gamma = 1$, indicating that the bending and torsional frequencies approach each other. For the IAT configuration, both experimental and theoretical results show a nearly constant frequency ratio of approximately $\gamma \simeq 1.1$ over the entire velocity range, suggesting limited aeroelastic interaction and stable modal separation. In contrast, the ULiège configuration shows a pronounced decrease in the frequency ratio with increasing velocity, dropping from values above 2.2 to approximately 1.3. This evolution, accurately captured by the numerical model, confirms a progressive coupling between the two modes as the flow speed increases. Such a trend is a good indication of instability.

The difference observed between the two configurations likely arises from differences in structural properties, including mass and stiffness distributions, as well as the relative positioning of the inertial and elastic axes. These factors strongly influence the velocity-dependent modal dynamics and explain the contrasting aeroelastic responses observed in both configurations.

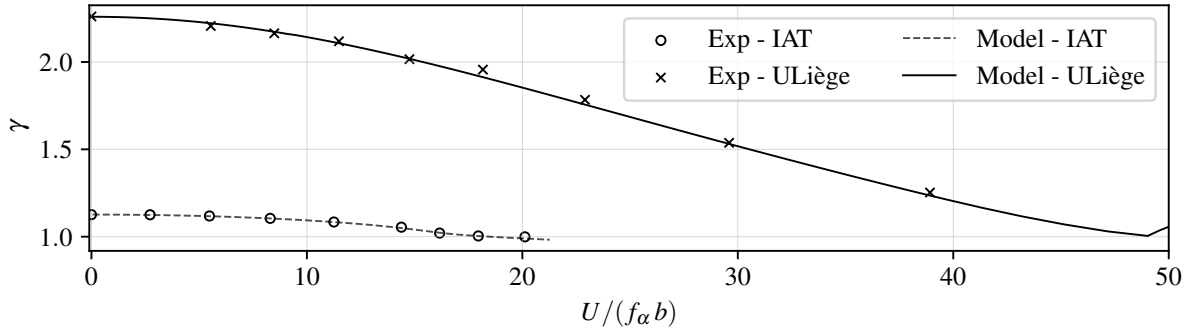


**Figure 4.7:** Evolution of frequency ratio $\gamma$ as a function of reduced velocity $U/(f_\alpha\, b)$ for both wing tested. Experimental results are superimposed to numerical prediction.

Finally, the instability mechanism differs between the two configurations. Indeed, the wing tested at IAT exhibited a dynamic instability driven by the second bending mode, as evidenced by a progressive reduction in its associated damping ratio with increasing velocity. In contrast, the wing studied at ULiège experienced a torsional instability, with a noticeable decrease in the damping ratio of the first mode, primarily associated with torsional deformation, as the flow speed increased.

# Chapter 5

# Conclusion and Perspectives

## 5.1 Conclusion

This study investigated flutter phenomena relevant to slender structures using both analytical and experimental approaches. The main objectives were to validate the developed aeroelastic model and to gain deeper insight into flutter behaviour.

The work began with chapter 2, which first provided a presentation of the theoretical foundations necessary to support the modelling and subsequent discussions. Then, the numerical development of the aeroelastic model was introduced. This included the structural considerations and the application of the Rayleigh–Ritz method to construct the structural response in both bending and torsion. To account for aerodynamic effects, two models were implemented: a quasi-steady formulation and an unsteady formulation based on Theodorsen's theory. These models captured the contributions of added mass, stiffness, and aerodynamic damping. The resulting model was then used to conduct a parametric study, with particular focus on the influence of the wingtip configuration and specific design choices on the aeroelastic response. It was observed that the wingtip configuration has a significant impact on the flutter onset. Increasing the tip mass was found to reduce the flutter speed, but if too much inertia is added, a frequency inversion occurs between the structural modes, making flutter onset no longer possible. While added mass generally lowers the flutter speed, this effect is limited by structural constraints.

Subsequently, chapter 3 presented the experimental campaigns carried out at IAT and ULiège. The chapter first provides a description of the tested wings and the associated design choices, followed by a detailed presentation of the instrumentation and excitation systems. The experimental setups are described separately for each configuration, covering wind-off characterisation, wind tunnel testing, and related procedures. Modal identification procedures were then introduced, along with the specific contexts in which each was applied. In particular, the PolyMAX method was employed during the wind-off characterisation phase, where the signal-to-noise ratio is sufficiently high to allow accurate identification. In contrast, during wind tunnel testing, where the excitation is induced by ambient turbulence and cannot be directly measured, an operational modal analysis technique was implemented, namely the covariance-driven Stochastic Subspace Identification method. The final part of this chapter was dedicated to presenting the measured results. The first section focused on wind-off characterisation, which enabled the evaluation of natural frequencies, damping ratios, and mode shapes under controlled excitation. These results served as a reference for both model calibration and experimental validation. The validation was performed by comparing the experimentally identified modal parameters with the numerical predictions, and further supported through the use of the modal assurance criterion. The second section presented the outcomes of the aerodynamic characterisation. This included the analysis of the wing's response under constant airflow, highlighting the influence of phenomena such as three-dimensional effects, gap sealing, and wingtip geometry on the aerodynamic forces. Finally, the aeroelastic responses were assessed. It was observed that both the *Saumon* configuration tested at IAT and the configuration tested at ULiège had the potential to exhibit flutter onset. However, only the ULiège wing reached an actual flutter condition. In

this context, the IAT results demonstrated that the wing was operating close to flutter onset, even if the instability did not fully manifest. This section also aimed to evaluate and discuss the accuracy of the identification procedures. The RFP method was also selected for the ULiège configuration, as it enabled a comparison between different identification techniques.

Finally, chapter 4 focused on comparing the experimental results from both campaigns with the predictions of the numerical model. It was shown that the frequency evolution is well captured by the model. However, the damping ratios proved more challenging to predict accurately, particularly for the stable mode, which was consistently overestimated by the model. The impact of modelling uncertainties was then discussed, and it was observed that certain parameters had a significant influence on the evolution of modal properties, potentially explaining some of the discrepancies between the model and experimental data. The chapter concluded with a comparison between the two wings, highlighting their respective aeroelastic behaviours and underlying structural differences.

## 5.2 Perspectives

Throughout this study, the aeroelastic behaviour of slender wings was investigated through a combination of experimental testing and numerical modelling. However, the results obtained also raise several additional questions and highlight several promising directions for future research :

- Firstly, as discussed in section 3.4.3, the wing initially tested at IAT suffered structural failure during the incidence tests. Consequently, a new prototype is expected to be built. In this context, the parametric study presented in section 2.4 provides valuable insight into potential design modifications that could help trigger flutter onset within a more accessible velocity range. For example, it was observed that increasing the aspect ratio promotes the likelihood of flutter occurring at moderate freestream velocities. Since the S4 wind tunnel at IAT offers a test section height of 3 meters, it would be worth considering increasing the half-span $s$ up to 2 m ($AR = 20$).
- Secondly, the experimental campaign conducted at ULiège should be repeated. In the initial test series, flutter onset occurred at high velocity during one of the earliest runs, which prevented the acquisition of sufficient data for a complete aeroelastic analysis. Therefore, rebuilding the wing and conducting more controlled and comprehensive testing would be highly beneficial.

  As briefly discussed in subsection 3.5.2, it is suspected that the flutter event may have been triggered or influenced by micro-cracks in the clamping area. As shown in Figure 5.1, damage was observed at the wing clamping interface following the flutter event. However, it remains unclear whether this damage was a consequence of flutter or its underlying cause. In this context, improving the attachment system, such as reducing the size of the fixation holes or adopting a more robust mounting approach, would be a valuable step toward ensuring repeatability and structural integrity during testing.

  Moreover, it would be beneficial to improve the sensor system. During the ULiège campaign, only a single wireless accelerometer was used, which limited the ability to fully characterize the structural response. It would be advantageous to use a set of two accelerometers, positioned near the wingtip and symmetrically placed with respect to the elastic axis. This configuration would enable the decomposition of the measured response into bending and torsional components, thereby enhancing the quality of the aeroelastic analysis. Additionally, packet loss was observed in the wireless system, which may introduce bias or uncertainty in the recorded data. To overcome this limitation, the use of cabled accelerometers is recommended. The sensor cables can be routed through the grooved structural profile, which serves as the primary support. Since the wing is hollow, this internal space can accommodate the accelerometer and wiring without degrading the wing aerodynamic. Furthermore, it would be useful to employ additional accelerometers or apply a roving hammer technique to enhance the quality of the wind-off characterisation.

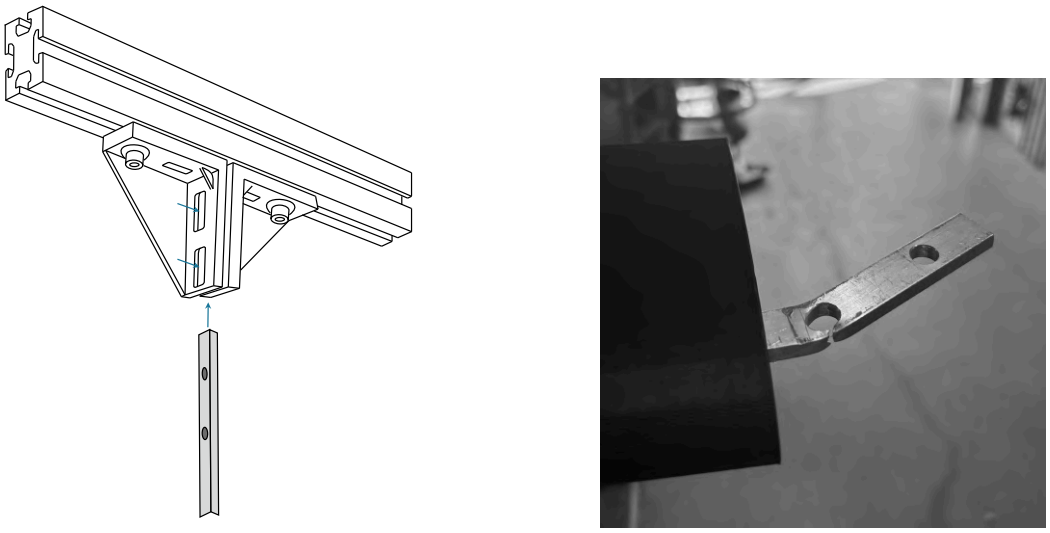

**(a)** Schematic of the clamping assembly.

**(b)** Picture of the wing clamping after flutter onset was observed in ULiège experimental campaign.

**Figure 5.1:** Clamping during ULiège campaign.

- Concerning the current aeroelastic model, several improvements could be considered. Firstly, it would be valuable to incorporate a dynamic stall model, such as the Leishman–Beddoes model or the ONERA model. This enhancement would provide a better understanding of the unsteady aerodynamic phenomena observed during the incidence tests, particularly in post-stall conditions. However, implementing a dynamic stall model alone is not sufficient. The effect of the structural gap should also be investigated, as it was observed to influences both the aerodynamic response and stall behaviour. Addressing this requires a more advanced aerodynamic characterisation, combining high-fidelity numerical simulations with targeted experimental validation.
- Finally, a promising direction for future research would be the study of flutter suppression through aeroelastic control. Over the years, developments in smart structures offered new alternatives for flutter suppression systems (Loewy 1997). Among the various functional materials, piezoelectric materials have attracted significant attention as potential actuators for such systems, due to their simple structure and rapid response time (Crawley & de Luis 1987).

  As mentioned in subsection 3.1.1, the wing studied at IAT was initially equipped with piezoelectric patches. In the present work, these patches were used exclusively as excitation sources. However, piezoelectric materials can also be employed as active/passive control actuators. In passive configurations, piezoelectric elements dissipate vibrational energy through resistive circuits without external input, whereas in active systems, they are integrated with sensors and controllers to generate real-time corrective forces based on structural feedback.

  For instance, both methods can be used simultaneously. Indeed, paper addressing this combined approach was presented by Tsushima & Su (2016). In this configuration, active piezoelectric actuation is employed as the primary mechanism for flutter suppression, while energy harvesting acts as a secondary passive approach, providing additional damping to mitigate wing vibrations.

# Bibliography


*AeroVironment Helios Prototype* (n.d.). https://en.wikipedia.org/wiki/AeroVironment_Helios_Prototype.

Bairstow, L. & Fage, A. (1916), Oscillations of the tailplane and body of an aeroplane in flight, Technical report, R&M 276, Part 2.

Colaone, M. (2010), 'De la nécessité de fabriquer des drones hale en europe'. https://www.aeroplans.fr/drones/necessite-fabriquer-drone-hale-europe.html.

Collar, A. R. (1946), 'The expanding domain of aeroelasticity'.

Crawley, E. F. & de Luis, J. (1987), 'Use of piezoelectric actuators as elements of intelligent structures', *AIAA Journal* **25**(10), 1373–1385.

Fung, Y. C. (1969), *An Introduction to the Theory of Aeroelasticity*, Dover.

Glauert, H. (1926), *The Elements of Aerofoil and Airscrew Theory*, Cambridge University Press.

Golinval, J.-P. (n.d.), 'Vibration testing and experimental modal analysis', University of Liège, Lecture Notes.

Géradin, M. & Rixen, D. J. (2015), *Mechanical Vibrations: Theory and Application to Structural Dynamics*, third edn, John Wiley & Sons, Chichester, United Kingdom.

*IAI Heron* (n.d.). https://fr.wikipedia.org/wiki/IAI_Heron.

Kunertova, D. (2019), 'Military drones in europe: The european defense market and the spread of military uav technology', Center for War Studies, University of Southern Denmark.

Lanchester, F. W. (1916), Torsional vibrations of the tail of an aeroplane, Technical report, R&M 276, Part 1.

Loewy, R. G. (1997), 'Recent developments in smart structures with aeronautical applications', *Smart Materials and Structures* **6**, R11–R42.

Meirovitch, L. (2010), *Fundamentals of Vibrations*, Waveland Press.

Noger, C. & Gilliéron, P. (2003), 'Banc expérimental d'analyse des phénomènes aérodynamiques générés par le dépassement de deux véhicules automobiles', Conference presentation, Nice, France.

*Northrop Grumman RQ-4 Global Hawk* (n.d.). https://fr.wikipedia.org/wiki/Northrop_Grumman_RQ-4_Global_Hawk.

Peeters, B., Auweraer, H. V. D., Guillaume, P. & Leuridan, J. (2004), 'The polymax frequency-domain method: a new standard for modal parameter estimation?', *Shock and Vibration* **11**(3-4), 395–409.

Peeters, B. & Roeck, G. D. (1999), 'Reference-based stochastic subspace identification for output-only modal analysis', *Mechanical Systems and Signal Processing* pp. 855–878.

Prieur, B. (2023), Contrôle piézoélectrique des charges et instabilités aéroélastiques sur aile flexible. Rapport de stage de recherche, École polytechnique, encadré au CNAM (LMSSC) par Xavier Amandolese et Boris Lossouarn.

Raghavan, B. & Patil, M. (2006), 'Flight dynamics of high aspect-ratio flying wings'.

Riazat, M. & Kheiri, M. (n.d.), 'Aeroelastic stability of a flexible high aspect-ratio wing with an imperfect end-support'. Fluid-Structure Interactions & Aeroelasticity Laboratory, Concordia University, Montréal, Canada.

Sereez, M., Abramov, N. & Goman, M. (2024), 'Cfd simulations and phenomenological modelling of aerodynamic stall hysteresis of naca 0018 wing', *Aerospace* **11**, 354.

Theodorsen, T. (1935), General theory of aerodynamic instability and the mechanism of flutter, Technical Report Report No. 496, National Advisory Committee for Aeronautics (NACA).

Théodore, A. (2020), Actions du vent sur les ouvrages souples dans le domaine temporel, Thèse de doctorat, Institut Polytechnique de Paris, École Polytechnique, Palaiseau, France. Spécialité : Mécanique des fluides et des solides, acoustique.

Tsushima, N. & Su, W. (2016), Passive and active piezoelectric effects on flutter suppression of highly flexible wings, *in* 'Proceedings of the First International Symposium on Flutter and its Application', University of Alabama, Tuscaloosa, AL, USA, pp. 67–.

Verstraelen, E. (2018), Aeroelastic Limit Cycle Oscillations Mitigation Using Linear and Nonlinear Tuned Mass Dampers, PhD thesis, University of Liège.

Wen, Z., Fang, G., Wang, J., Ge, Y. & Li, S. (2025), 'Practical flutter speed formulas for flexible structures considering all torsional-to-vertical frequency ratios', *Journal of Wind Engineering and Industrial Aerodynamics* **261**, 106085.

Wright, J. R. & Cooper, J. E. (2008), *Introduction to Aircraft Aeroelasticity and Loads*, Vol. 18, John Wiley & Sons.

Zimmerman, N. H. & Weissenburger, J. T. (1964), 'Prediction of flutter onset speed based on flight testing at subcritical speeds', *Journal of Aircraft* **1**(4), 252–256.

# Appendix A

# Wind tunnel of the Institut Aérotechnique in Paris

The Institut Aérotechnique is a public research and testing facility affiliated with the Conservatoire National des Arts et Métiers (CNAM) in Paris. Specialized in experimental aerodynamics, it provides advanced testing capabilities for both academic and industrial applications. IAT hosts several wind tunnels tailored to different aerodynamic investigations, including the S4, S6, and S10 tunnels, as well as the SVL (long-vein tunnel) and the Flûte de Pan (FdP) tunnel.

This study was conducted exclusively in the S4 wind tunnel, which offers suitable conditions for aeroelastic testing, particularly in terms of flow quality, test section size, and instrumentation access. The S4 is a low-speed facility featuring a $5\,\mathrm{m} \times 3\,\mathrm{m}$ test section within a total tunnel length of $10\,\mathrm{m}$. A contraction ratio of $4$ ensures flow uniformity, with wind speeds adjustable from $0$ to $40\,\mathrm{m/s}$ and a maintained turbulence intensity of approximately $1\%$. Airflow is generated by two four-blade fans, each $4.6\,\mathrm{m}$ in diameter and driven by $260\,\mathrm{kW}$ motors. The facility also includes a $360°$ rotating platform with a $4\,\mathrm{m}$ diameter, allowing full angular positioning of test models. The IAT S4 facility is shown in Figure A.1.

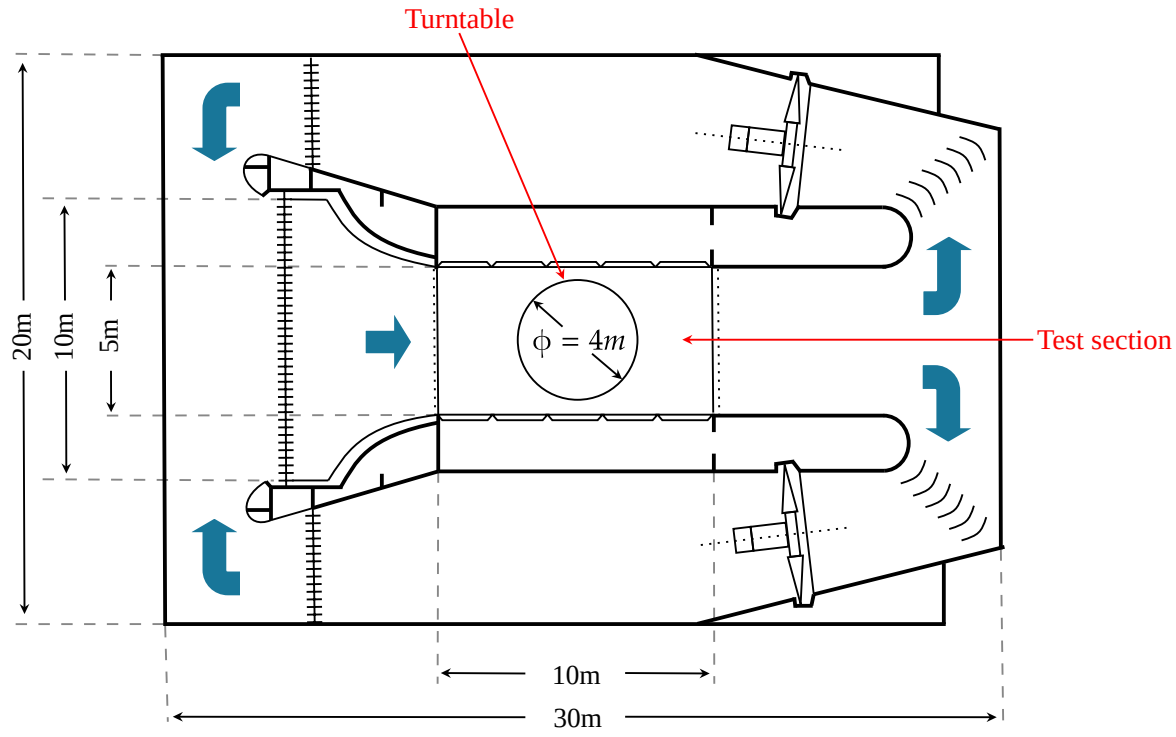


**Figure A.1:** Iat S4 wind tunnel, reproduced from Noger & Gilliéron (2003).

# Appendix B

# Wind tunnel at the University of Liège

The wind tunnel of the University of Liège was constructed in 1999 on the Sart-Tilman campus, with funding support from the Walloon Region and the European Commission. It is a low-speed, multidisciplinary facility that can operate in either closed-loop or open-loop configuration under atmospheric pressure.

Experimental campaigns can be conducted in one of two interchangeable test sections depending on the size and configuration of the model under investigation. These tests sections are respectively referred as the Aeronautical test section (TS1), and the Wind engineering test section (TS2).

The main characteristics of the two test sections are summarized in Table B.1, while the specifications of the wind tunnel fan are detailed in Table B.2. A schematic view of the facility is provided in Figure B.1.

Table B.1: Characteristics of the wind tunnel of ULiège.

| Characteristics | TS1 | TS2 |
|---|---|---|
| Dimension (Width × Height × Length) | $2\,\mathrm{m} \times 1.5\,\mathrm{m} \times 5\,\mathrm{m}$ | $2.5\,\mathrm{m} \times 1.8\,\mathrm{m} \times 5\,\mathrm{m}$ |
| Airspeed range (Open/Closed loop) | [2 - 40] / [2 - 65] m/s | [2 - 30] / [2 - 40] m/s |
| Turntable diameter | $1.5\,\mathrm{m}$ | $2\,\mathrm{m}$ |
| Thermal stability | $1\,^{\circ}\mathrm{C}$ | $1\,^{\circ}\mathrm{C}$ |
| Turbulence level | $0.15\%$ | $< 0.23\%$ |
| Streamwise static pressure gradient | $0.3\%/\mathrm{m}$ | $0.5\%/\mathrm{m}$ |
| Mean angle divergence | $< 0.2\%$ | $< 0.2\%$ |
| Speed non-uniformity | $< 0.5\%$ | $< 0.8\%$ |

Table B.2: Characteristics of the axial fan used in the wind tunnel.

| Characteristics | Specification |
|---|---|
| Temperature range | $[15 - 50]\,^{\circ}\mathrm{C}$ |
| Fan diameter | $2.8\,\mathrm{m}$ |
| Maximum volumetric flow rate | $186\,\mathrm{m}^3/\mathrm{s}$ |
| Maximum total pressure rise | $1953\,\mathrm{N}/\mathrm{m}^2$ |
| Rotation speed range | $[25 - 820]\,\mathrm{rad}/\mathrm{min}$ |
| Maximum rotation speed | $880\,\mathrm{rad}/\mathrm{min}$ |
| DC motor power | $440\,\mathrm{kW}$ |

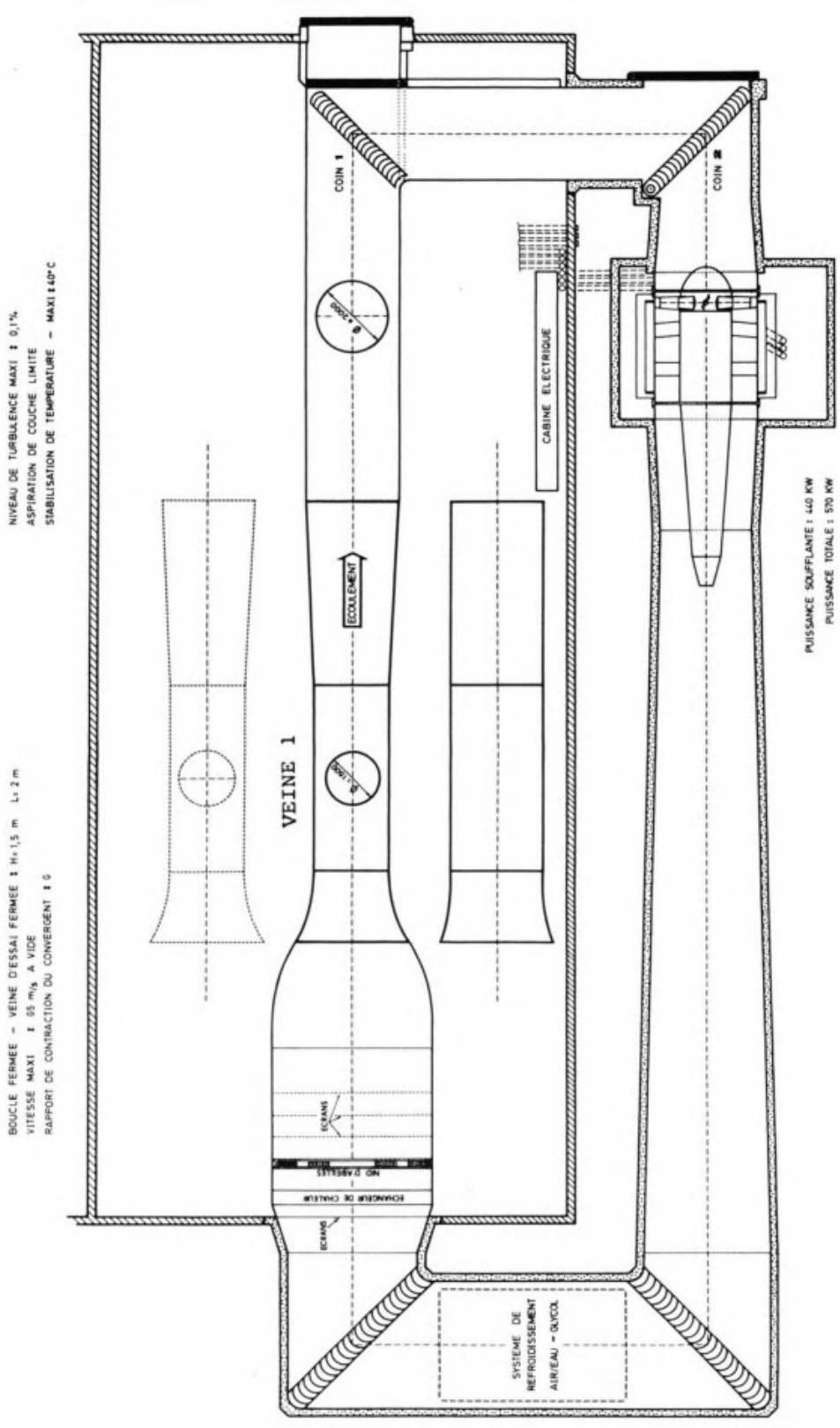


**Figure B.1:** Schematic view of the wind tunnel of ULiège.

# Appendix C

# Theoretical and experimental stiffness assessment

## C.1 Theoretical stiffness estimation

The theoretical determination of the structural stiffness, *i.e.* the chordwise bending stiffness $EI_z$, the flapwise bending stiffness $EI_x$, and the torsional stiffness $GJ$, is based on the geometry of the cross section. In this context, the following expressions apply to rectangular cross-sections, either full or hollow, as defined in Figure C.1.

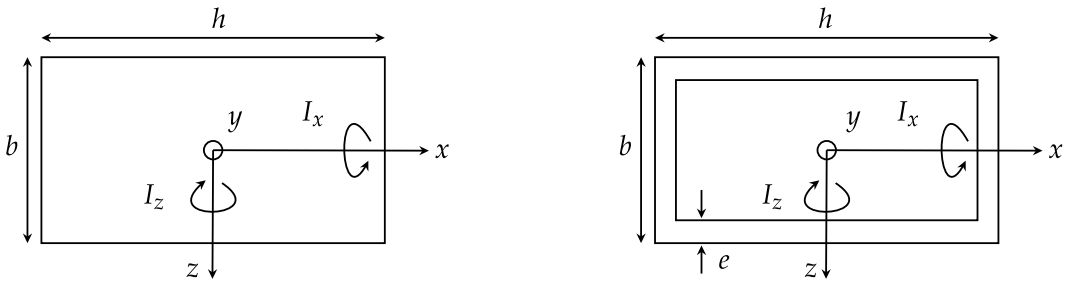


**(a)** Full section. **(b)** Hollow section.

**Figure C.1:** Geometric definitions for the full (left) and hollow (right) rectangular cross-sections used in the stiffness evaluation.

### C.1.1 Full section

For a full cross-section, the second moments of area with respect to the $x$ and $z$ axes, denoted $I_x$ and $I_z$ respectively, are given by the expressions

$$I_x = \frac{hb^3}{12}, \qquad I_z = \frac{bh^3}{12}, \tag{C.1}$$

where $b$ and $h$ represent the width and height of the cross-section, respectively. The torsional constant $J$ can be estimated using an empirical approximation suitable for rectangular sections

$$J = b^3 h \left( \frac{1}{3} - \frac{0.21\, b}{h} \left( 1 - \frac{b^4}{12h^4} \right) \right). \tag{C.2}$$

The shear modulus $G$ is related to the Young's modulus $E$ and Poisson's ratio $\nu$ by

$$G = \frac{E}{2(1+\nu)}. \tag{C.3}$$

### C.1.2 Hollow section

For hollow cross-section, thee second moments of area with respect to the $x$ and $z$ axes, denoted $I_x$ and $I_z$ respectively, are given by the expressions

$$I_x = \frac{hb^3}{12} - \frac{(h-2e)(b-2e)^3}{12} \quad , \quad I_z = \frac{bh^3}{12} - \frac{(b-2e)(h-2e)^3}{12}. \tag{C.4}$$

The torsional constant $J$ for a thin-walled rectangular hollow section can be approximated using the following expression

$$J = \frac{4A_m^2}{\sum_{i=1}^{4}\left(\frac{l_i}{e_i}\right)} = \frac{2e\,A_m^2}{h+b-2e} \quad \text{with} \quad A_m = (b-e)(h-e), \tag{C.5}$$

where $A_m$ is the area enclosed by the median of the wall thickness, $l_i$ denotes the length of the $i^{\text{th}}$ segment of the median line, and $e_i$ is the corresponding wall thickness of that segment.

## C.2 Experimental stiffness measurement procedure

The structural stiffnesses of the beam can be experimentally determined through static loading tests. This method consists of applying a known static force at the free end of the cantilevered structure and measuring the resulting deformation. Assuming linear elasticity and small deformations, the associated stiffness values can be inferred directly from the measured displacements. It is important to ensure that pure flapwise bending, chordwise bending, or torsional loading is applied in order to isolate the corresponding stiffness component. The following relationships can be used to retrieve the structural stiffnesses from the experimental data

$$z(s) = \frac{Fs^3}{3EI_x} \quad , \quad x(s) = \frac{Fs^3}{3EI_z} \quad , \quad \alpha(s) = \frac{2\,F\,(b/2)\,s}{GJ} = \frac{Fbs}{GJ}, \tag{C.6}$$

where $z(s)$ and $x(s)$ are the measured displacements under vertical and horizontal loading, respectively, $\alpha(s)$ is the twist angle at the tip, $b$ is the moment arm for torsional loading, and $s$ is the beam length. A schematic of the experimental procedure is shown in Figure C.2.

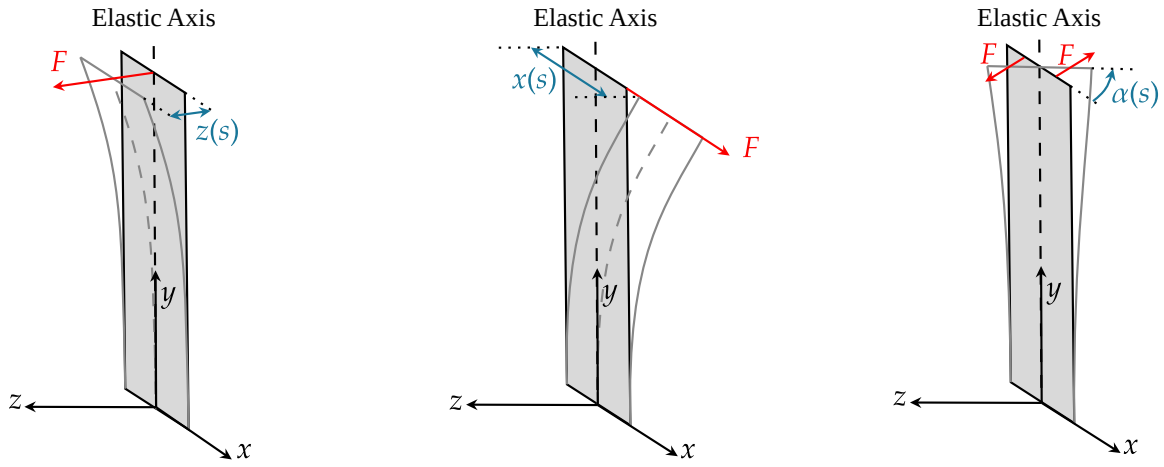


**Figure C.2:** Qualitative representation of the experimental stiffness measurement procedure.